The influence of minor stenoses on carotid artery flow

The influence of minor stenoses

on carotid artery flow

Daniëlle Palmen

The influence of minor stenoses on carotid artery flow

The influence of minor stenoses on carotid artery flow

PROEFSCHRIFT

ter verkrijging van de graad van doctor
aan de Technische Universiteit Eindhoven
op gezag van de Rector Magnificus, prof.dr. J.H. van Lint,
voor een commissie aangewezen door het College van Dekanen
in het openbaar te verdedigen
op dinsdag 24 mei 1994 om 14.00 uur

door

DANIËLLE ELISABETH MARIA PALMEN

geboren te Susteren

Dit proefschrift is goedgekeurd door de promotoren:

prof.dr.ir. J.D. Janssen
prof.dr.ir. A.A. van Steenhoven

en de copromotor:

dr.ir. F.N. van de Vosse

Vóór Hans

Contents

Summary

The study of the flow in the carotid artery bifurcation is of great interest with respect to both the genesis and the diagnosis of atherosclerotic disease. The main objective of this thesis is to investigate the possibility of detecting minor stenoses (with an area reduction of 25%) in the carotid artery bifurcation from information on the velocity field in space and time. For that purpose experimental techniques (hydrogen-bubble visualization and laser Doppler anemometry) have been combined with a computational technique (finite element method). The experiments have been performed in rigid plexiglass models of a non-stenosed and a 25% stenosed carotid artery bifurcation under physiological flow conditions using a Newtonian fluid. The numerical analysis has been performed in models of the carotid artery bifurcation with degrees of occlusion of 0%, 25% and 50%.

The hydrogen-bubble visualizations have provided a qualitative and overall view of the locations of interest and fluid dynamical phenomena in the three-dimensional (3D) time-dependent carotid artery flow. The visualizations have shown that shortly after the onset of diastole vortex formation occurs in a shear layer, the interface between regions with low velocities near the non-divider wall and high velocities near the divider wall. Though the 25% stenosis only slightly influences the flow phenomena, the most striking influences are found in the stability of the shear layer. However, relatively small changes in the inflow conditions appear to influence the stability of the shear layer even more significantly.

The finite element computations of the flow problem offered the possibility of parameter variation with respect to the geometry and inflow conditions. The computations have given a useful and clear insight into the complex three-dimensional axial and secondary flow fields in the carotid artery bifurcation: (i) during systolic acceleration the region with reversed axial flow near the non-divider wall is 'washed away'; (ii) a region with reversed axial flow develops during systolic deceleration, reaching its largest dimensions in the initial phase of diastole and (iii) after systolic deceleration a significant secondary flow field is present, causing helical flow patterns in the bifurcation and resulting in an extension in circumferential direction of the region with high axial velocities. The influence of the 25% stenosis on the 3D velocity field mainly involves three aspects: (i) a decrease of the reversed axial velocity area at occluded sites in the initial phase of diastole; (ii) an increase of the reversed axial velocity area downstream the stenosis, coinciding with the shift of the main flow towards the divider wall and (iii) an increase of the near wall secondary velocities.

The laser Doppler method (LDA) has been used to gain accurate and detailed information on the time-dependent axial and secondary velocity fields, thus also offering the

possibility to validate the computational results. Interesting flow phenomena have been found in a period starting from systolic deceleration up until half of the diastolic phase. During systolic deceleration a reversed flow region is formed near the non-divider wall and large radial velocity gradients occur near the shear layer. In the initial phase of diastole significant oscillations occur in both the non-stenosed and the 25% stenosed models. After that, a smooth transition to the end-diastolic situation occurs, pointing at the quasi-static behavior at that time. The influence of the 25% stenosis on the axial velocities in the plane of symmetry is small and mainly involves two aspects: (*i*) a disturbance with enlarged velocities in the area with low velocity appears in the initial phase of diastole; (*ii*) oscillations in the shear layer, which are present in the non-stenosed model, seem to have larger amplitudes and lower frequencies in the 25% stenosed model.

In a comparison of the computational and the LDA results globally good agreement has been found. However, during systolic deceleration and in the initial phase of diastole the time scale of the computed unsteady shear layer behavior appeared to be smaller than that from the experiments. These differences are mainly ascribed to computational inaccuracies, due to the limitations of the finite element method as used in this study.

A model study on 2D unsteady shear layers in a simplified geometry, represented by a 2D rectangular channel, has provided useful knowledge on unsteady shear layer behavior. It was shown that unsteady vortex shedding occurs in the 2D shear layer during systolic deceleration and in the initial phase of diastole and that the vortices move downstream with the instantaneous local fluid velocity. Though these phenomena resemble the unsteady shear layer behavior in the carotid artery bifurcation, this 2D model situation may not simply be mapped on the complex 3D flow case of the carotid artery bifurcation.

In order to obtain parameters that can trace the differences between the flow fields of the non-stenosed and the stenosed geometries, the LDA data have been used. Several detection parameters have been evaluated. Together with a study on the influence of inflow conditions on these parameters, it has been shown that for none of the parameters considered a determinate method was found to detect minor stenoses by solely considering fluid dynamical aspects.

Considering the main objective of this thesis, the detection of minor stenoses, the following general conclusion can be formulated. Though the fluid dynamics of the flow in models of the 0% and the 25% stenosed carotid artery bifurcation indicate that the unstable shear layer behavior in the initial phase of diastole and the frequency contents of the velocity signals are influenced by the presence of a minor stenosis, even for well-controlled conditions and accurate experimental techniques this influence is not determinative for the detection of *minor* stenoses, since the effects on the flow field are small, local in time and space and dependent on other factors like the inflow conditions and the geometry. Only for *moderate* stenoses (50% area reduction) a possibly useful detection parameter may be the first velocity moment at peak systole, when it is evaluated as a function of the axial position in the internal carotid artery. Future research will be needed to investigate the value of this parameter for the detection of moderate stenoses. A combination of the information on the hemodynamics and local changes in wall distensibility might have more potential in the detection of minor stenoses (less than 25% area reduction).

Chapter 1

Introduction

1.1 Atherosclerosis in the carotid artery bifurcation

Atherosclerosis Atherosclerosis is a sclerotic arterial disease, the effects of which are the most important cause of mortality in the developed Western countries. The disease involves the vessel walls of large (muscular) arteries. The disease declares itself with initial intimal thickening of the arterial wall, subsequently followed by significant plaque formation, composed of intracellular and extracellular lipids, cholesterol, fibroblasts and smooth muscle cells. Lesions may vary in size between partial obstruction to complete obstruction of the vessel. Older lesions show calcification, ulceration and adherent thrombus formation that may be the source of emboli at downstream sites. Atherosclerosis occurs at many locations in the vascular system in the human body. Here, we will concentrate on one of those locations: the carotid artery bifurcation.

Carotid artery bifurcation The left and right carotid artery bifurcations are located in the human neck. The main blood supply to the neck, face and brain is carried through two common carotid arteries. In the upper neck, each common carotid bifurcates in two arteries. In figure 1.1 a schematic overview of this carotid artery bifurcation as derived from data given by Bharadvaj *et al.* (1982ab) is presented. The bifurcation consists of a main branch, the common carotid artery, which asymmetrically divides in two branches, the internal carotid artery and the external carotid artery. In the proximal part of the internal carotid artery a small widening exists, named the carotid sinus or bulbus. Arterial branches from the external carotid supply blood to the neck, face and crown of the head. The internal carotid supplies the eye and the brain from blood (Guyton, 1985). From clinical practice it is known that the bifurcation is very susceptible for the development of atherosclerotic disease. Mostly the lesions are found in the proximal part of the internal carotid artery at the so-called non-divider side of the carotid sinus as indicated in figure 1.1. As the atherosclerotic lesions may be associated with the formation of thrombi, release of emboli from the plaques in the carotid artery can obstruct smaller vessels of the brain at downstream sites. This may lead to stroke, often associated with irreversible brain damage,
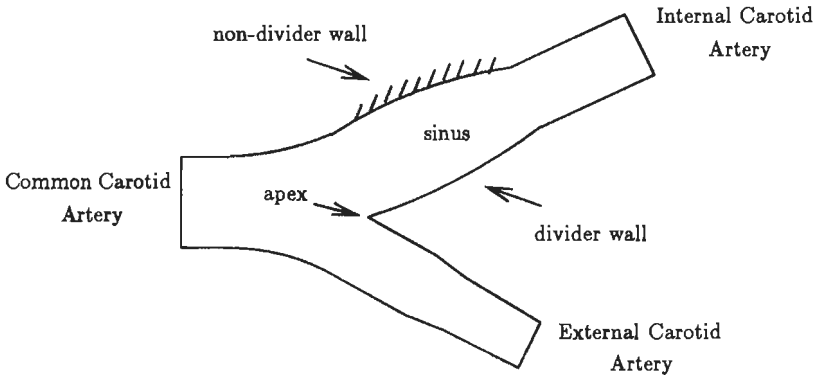
Figure 1.1: *Schematic overview of the non-stenosed carotid artery bifurcation, according to Bharadvaj (1982ab). At all sites the cross-sections are circular. The site of preference for atherosclerosis is marked at the non-divider wall of the internal carotid artery.*

transient ischemic attacks or even death.

The carotid artery bifurcation is well accessible to ultrasound measurements, because of its superficial location in the human neck. In clinical practice ultrasound measurements are commonly used to analyze the velocity field in the carotid artery bifurcation and to diagnose carotid artery stenoses in patients with and without neurological failures.

Objectives of the study   It goes without saying that the study of the evolution of the disease (Nerem, 1992) and the study for diagnostic tools at an early stage of the disease (see for instance Van Merode *et al.*, 1989) is of utmost importance. Detection of the disease at an early stage would also create possibilities to large scale investigation of the population on initial carotid artery disease, thus stimulating preventive approaches of the disease. Since it is believed that hemodynamical aspects of the blood flow play an important role in both the genesis and the diagnosis of atherosclerotic disease in the carotid artery bifurcation, in this study the influence of a minor stenosis (25% area reduction) on the flow field in the carotid artery bifurcation is investigated. A comparison of the results of the flow field in models of a non-stenosed and a minor stenosed bifurcation may lead to the definition of parameters of disturbance, that can possibly be used for early detection of the atherosclerotic disease.

1.2   Literature survey on carotid artery flow

Many previous studies have dealt with the hemodynamics of carotid artery flow. An overview of the main references on this subject is given in table 1.1. For each reference the flow conditions are given. The flow conditions in the carotid artery bifurcation are

characterized by three dimensionless parameters, the Reynolds number Re, the Womersley number or frequency parameter α and the flow division ratio γ, that are defined as follows:

$$Re = \frac{DU_0}{\nu}, \qquad \alpha = \frac{D}{2}\sqrt{\frac{2\pi}{\nu T}}, \qquad \gamma = \frac{Q_e}{Q_c}, \qquad (1.1)$$

where D represents the diameter of the common carotid artery, U_0 the cross-sectional averaged velocity in the common carotid artery, ν the kinematic viscosity, T the period time of the flow pulse and Q_c, Q_e the flows through the common and external carotid arteries. In table 1.1 additional information is given about the dimension of the study, the condition of the walls, the fluid behavior, the percentage area reduction and the methods that have been used. A more detailed description of the studies as mentioned in table 1.1, will be given in the sequel of this section.

2D analysis From steady two-dimensional (2D) flow analyses some striking flow phenomena are found, that are characteristic for bifurcation flow: (i) boundary layer separation occurs along the non-divider side walls, resulting in a reversed flow region which extends into the daughter branches of the bifurcation; (ii) because of the nature of the entrance flow in the communis and the bifurcation geometry, high axial velocities and velocity gradients are found near the divider walls; (iii) near the apex (the flow divider) a peak in the shear stress can be observed, which decreases in downstream direction.

In unsteady flow analyses similar features as mentioned above can be found. However, unsteadiness of flow also implies temporal variations in the location and length of the reversed flow region and in the values of the wall shear stress, that become significantly larger than their mean values.

A shortcoming of a two-dimensional analysis of bifurcation flows is the negligence of all secondary fluid motions, that occur in three-dimensional geometries. Since it is known that these secondary motions significantly influence the axial velocity distributions in the plane of symmetry (van de Vosse *et al.*, 1990), it is unlikely that the 2D flow analysis has much relevance to the present study. Therefore, in the sequel of this study only 3D flows will be considered.

3D analysis Many authors studied three-dimensional (3D) carotid artery flow (see also table 1.1). Characteristic flow features in the carotid artery bifurcation, found with steady flow conditions, can be summarized as follows.

- Flow separation occurs near the non-divider wall of the internal carotid artery, resulting in a reversed flow region that may extend in radial direction up to 60% of the local diameter of the carotid sinus near the center (Bharadvaj *et al.*, 1982a and Rindt *et al.*, 1988). At the divider side of the carotid sinus a region of high axial shear with high axial velocities is present, separated from the reversed flow region by a more or less pronounced shear layer. Near the apex the shear rates are maximal.

Author et al.	$\bar{Re}$	Re_d	Re_s	γ	α	D	wall	visc.	%AR	method
Baaijens ('93)	300			?	std.	2D	R	nN	-	FEM
Clark ('83)	?	?	?	?	2.8	2D	R	N	>25	FDM
Kleinstreuer ('91)	?	?	?	?	unst.	2D	R	N	50	FEM
Nazemi ('90)		150	750	?	6.1	2D	R	N	-	FEM
Perktold ('86)	200	90	600	0.3	?	2D	R	N	-	FEM
Rindt ('87)	710			0.35	std.	2D	R	N	-	FEM,LDA
		250	770	0.35	3.4	2D	R	N	-	FEM,LDA
v.d.Vosse ('90)	250	175	650	0.4	4	2D	R	N	25	FEM
Balasubram. ('79)	400-800			0.2-0.4	std.	3D	R	N	-	LDA,H$_2$
Bharadvaj ('82a)	400-1200			0.2-0.4	std.	3D	R	N	-	H$_2$,dye
Bharadvaj ('82b)	400-1200			0.2-0.4	std.	3D	R	N	-	LDA
Corver ('85)	700			0.3	std.	3D	R	N	5	LDA
Fei ('88)	400			0.3	std.	3D	R	N	>36	pulsed D.
LoGerfo ('81)	200-1200			0-0.55	std.	3D	R	N	-	dye
Motomiya ('84)	50-1200			0.1-0.8	std.	3D	R	N	-	tracer
Rindt ('88)	640			0.5	std.	3D	R	N	-	LDA
Rindt ('90)	640			0.5	std.	3D	R	N	-	FEM,LDA
Rittgers ('88)	400			0.3	std.	3D	R	N	>36	pulsed D.
Zarins ('83)	400-1200			0.2-0.4	std.	3D	R	N	-	LDA
Anayiotos ('91)	300		800	?	4	3D	D	N	-	LDA
Anayiotos ('92)		270	800	?	4	3D	D	N	-	LDA
Fukushima ('88)	323	0	615	0.21	3.8	3D	R	N	-	dye
Ku ('83)		400	1200	0.30	6.0	3D	R	N	-	H$_2$
Ku ('85a)	300		800	$\gamma(t)$	4.1	3D	R	N	-	LDA
Ku ('85b)	300		800	$\gamma(t)$	4.1	3D	R	N	-	LDA
Ku ('87)	300		800	$\gamma(t)$	4.0	3D	R	N	-	LDA
Liepsch ('93)	250		600	0.3	3	3D	D	nN	90	LDA
Perktold ('90)	200		600	0.3	5.6	3D	R	N	-	FEM
Perktold ('91a)	300		775	$\gamma(t)$	4.8	3D	R	N	-	FEM
Perktold ('91b)	300		775	$\gamma(t)$	4.8	3D	R	nN	-	FEM
Perktold ('93)	?	?	?	?	unst.	3D	R/D	N	-	FEM
Reuderink ('91)	200		500	0.3-0.4	5	3D	D	N	-	FEM
Rindt ('94)		190	910	0.3	6.5	3D	R	N	-	FEM,LDA
Caro ('92)			in	vivo		3D	D	nN	-	MRI
Ku ('85a)			in	vivo		3D	D	nN	-	pulsed D.
v.Merode ('89)			in	vivo		3D	D	nN	<50	pulsed D.
Reneman ('85)			in	vivo		3D	D	nN	<50	pulsed D.

Table 1.1: *Main references on hemodynamics in the carotid bifurcation. Notation: $\bar{Re}$, Re_d, Re_s: the mean, diastolic and systolic values of Re; γ: the flow division ratio ($\gamma(t)$ represents a time-varying γ according to Ku (1985b)); α: the Womersley number (std. / unst. means steady and unsteady flow); D: the dimension (2D/3D); wall: rigid wall (R) or distensible wall (D); visc.: Newtonian (N) or non-Newtonian (nN) fluid behavior; %AR: the percentage Area Reduction and method: pulsed D: pulsed Doppler ultrasound, H_2: hydrogen-bubble visualization, dye: dye visualization, tracer: visualization with tracer particles, LDA: Laser Doppler Anemometry, FEM: Finite Element Method, FDM: Finite Difference Method and MRI: Magnetic Resonance Imaging.*

- The reversed flow region near the non-divider wall in the carotid sinus is no classic recirculation zone (i.e. a region in which fluid particles are entrapped), but fluid particles are washed downstream along helical trajectories (Bharadvaj *et al.*, 1982a). This phenomenon is referred to as the horseshoe vortex by Fukushima *et al.* (1988). These helical trajectories are caused by the strong secondary flow field, showing great resemblance with a Dean vortex, that is typical for flows in bends (Rindt *et al.*, 1990). Since the bifurcation models in most of the studies are symmetrical, the secondary flows in the sinus consist of a pair of counter-rotating helices. Bharadvaj *et al.* (1982a) has found that these helices undergo oscillations for Reynolds numbers larger than 800.

The importance of unsteadiness in the 3D carotid bifurcation becomes clear from the work of Anayiotos *et al.* (1991,1992), Fukushima *et al.* (1988), Ku *et al.* (1983, 1985ab, 1987), Perktold *et al.* (1990, 1991ab, 1993), van Merode *et al.* (1989), Reneman *et al.* (1985), Reuderink (1991) and Rindt *et al.* (1988, 1990, 1994). Though many flow features are comparable to the flow situation in the steady case, in the unsteady flow case the flow field becomes even more complicated. The most important flow features of the 3D time-dependent flow field are summarized below.

- During flow acceleration the axial velocities in the whole bifurcation are positive, i.e. the reversed flow region fully disappears. The secondary velocities are small during flow acceleration.

- During flow deceleration a reversed flow region with negative axial velocities develops near the non-divider wall in the carotid sinus. The velocities near the divider wall remain relatively high, resulting in a significant shear layer at the boundary between the high and low velocity regions. Ku *et al.* (1983) report on a small vortex in the shear layer in the initial phase of diastole. The secondary velocities are significant during flow deceleration, causing the onset of helical flow patterns. Due to the secondary flow field, fluid particles with relatively high axial velocities near the divider wall are convected in circumferential direction, resulting in 'C-shaped' axial velocity contours (Rindt *et al.*,1994).

- The strong unsteady flow behavior continues to exist in the initial phase of diastole, but in late diastole the secondary flow field fades away and a smooth transition to the end-diastolic situation occurs.

Stenosed carotid artery flow　The influence of stenoses on the hemodynamics of the carotid bifurcation is less intensively studied in literature. A short summary is given here (for the conditions see also table 1.1). Clark *et al.* (1983) numerically analyzed 2D flow in mild and severe stenosed bifurcations, in which an asymmetrical smooth-contoured stenosis was positioned in the main branch upstream the bifurcation. They found enlarged shear stresses at the zenith of the stenosis, which increases with stenosis severity. For severe stenoses the authors found large pressure drops near peak flow.

Corver *et al.* (1985) experimentally analyzed the influence of a 5% stenosis, that was positioned at the non-divider wall in the carotid sinus under steady flow conditions. They found a little influence of the stenosis on the so-called velocity moments, as defined by Olson (1971). In chapter 7 the velocity moments will be discussed in more detail.

Fei *et al.* (1988) and Rittgers *et al.* (1988) studied stenosed carotid artery flow under steady flow conditions. The authors used smooth axisymmetric constrictor plugs with 0%, 36%, 64%, 85% and 96% area reduction, which were placed in the carotid sinus. Using a pulsed Doppler measuring technique, they found complete laminar flow for the 0% stenosed bifurcation, increased axial velocities at the constrictor for the 36% stenosis, an oscillatory jet for the 64% stenosis and a fully turbulent jet for the 96% stenosed bifurcation.

Kleinstreuer *et al.* (1991) numerically studied 2D flow in a 50% stenosed carotid artery in order to find a better carotid artery design with respect to plaque formation. They found that the presence of a stenosis reduces the extent of reversed flow zones in the carotid sinus.

Liepsch *et al.* (1993) experimentally studied a 3D 90% stenosed carotid bifurcation under pulsatile flow conditions using a non-Newtonian measuring fluid. The stenosis was positioned at the non-divider wall in the carotid sinus. The authors found flat profiles and high shear rates at stenosed sites, pointing at a 'jet-effect'. Further downstream highly disturbed flow was found.

Van Merode *et al.* (1988, 1989) studied the detectability of stenoses (less than 50% area reduction) in vivo, using a multigate pulsed Doppler system. The authors found that carotid artery lesions with a diameter reduction of 50% (equivalent to 75% area reduction for circular cross-sections) can be detected rather accurately by considering abnormalities in the blood flow patterns (Van Merode *et al.*, 1988). In a later study (Van Merode *et al.*, 1989) also local changes in vessel wall distensibility were considered in addition to the local disturbances of the blood flow patterns. The authors mentioned that carotid artery lesions with a diameter reduction up to 50% (equivalent to 50% area reduction) could be diagnosed.

Van de Vosse *et al.* (1990) numerically studied 2D pulsatile flow in a 25% stenosed bifurcation. The stenosis was positioned at the non-divider side of the carotid sinus. The influence of the 25% stenosis was expressed in (i) the smaller reversed flow region near the non-divider wall during systolic deceleration; (ii) the absence of a reversed flow region at the non-divider side during the second half of diastole; (iii) a small reversed flow region downstream the stenosis and (iv) increased wall shear stresses proximal to the maximal area reduction and a sudden decrease of the wall shear stress downstream the stenosis.

Other factors   In the references from table 1.1 additional information on the influence of various parameters on the hemodynamics in the carotid artery bifurcation is given. The most important phenomena will be listed below.

Wall distensibility The influence of wall distensibility on the hemodynamics of carotid artery flow by comparing results for the rigid and distensible case under identical conditions, has been investigated by Anayiotos *et al.* (1991, 1992), Perktold *et al.* (1993) and Reuderink (1991). Qualitatively it was found that the global flow fea-

tures in the rigid and distensible models were similar, though quantitatively the wall distensibility is found to reduce the effects that are typical for carotid artery flow. Reuderink (1991) and Perktold *et al.* (1993) found that the reversed flow region becomes smaller in size and that the velocities in this region are smaller in value in the distensible case, resulting also in smaller radial velocity gradients in the shear layer. On the other hand Anayiotos *et al.* (1991, 1992) report on larger reversed flow regions in space and time for the distensible case. The cause of this discrepancy is not clear. The values of the high shear rates near the divider wall are reduced, whereas the shear rates observed near the non-divider wall are less negative at end-systole (Reuderink, 1991). The 'C-shaped' curve of the axial velocity contours at end-systole is less pronounced in the distensible model (Reuderink, 1991). The values of the secondary flow peaks appear to be smaller in the distensible case (Anayiotos *et al.*, 1991 1992).

Non-Newtonian fluid behavior Blood is a suspension of red cells, white cells and platelets in plasma. The mechanical properties of blood are studied intensively in literature and it is well accepted that blood can be considered as Newtonian at high shear rates and non-Newtonian at low shear rates (Nerem, 1992). Baaijens *et al.* (1993) numerically studied the effect of this non-Newtonian fluid behavior in the carotid artery bifurcation, using stationary flow conditions in a 2D rigid model. They found that the global flow features are hardly influenced by the non-Newtonian fluid behavior. However, quantitatively the non-Newtonian influence is expressed by (i) 5 - 10% lower maximum values of the axial and secondary velocity profiles in the non-Newtonian case; (ii) lower values of the wall shear stresses along the divider wall and higher values along the non-divider wall (the maximum difference amounts 5%) and (iii) a slightly reduced dimension of the reversed flow region in radial direction.

Liepsch and Moravec (1984) studied the differences in flow behavior of Newtonian and non-Newtonian fluids in a simplified model of the human renal artery, using laser Doppler anemometry. Substantial differences were found in zones of flow separation and secondary flow. In a later study Ku and Liepsch (1986) experimentally studied the effect of the non-Newtonian behavior on the flow field in a 90°-T-bifurcation, using non-Newtonian viscoelastic fluids. They showed that for those geometries the location of reversed flow regions can be dramatically altered as compared to what is observed for Newtonian fluids.

Perktold *et al.* (1989) presented a pulsatile non-Newtonian blood flow simulation through a symmetric bifurcation with an aneurism. From a comparison of non-Newtonian and Newtonian results they conclude that there are no essential differences at the occurring high shear rates. It should be noted that the model fluids and the constitutive models, used for the computations, do not completely simulate the rheological behavior of blood. Therefore caution must be taken in the interpretation of these results and additional research is needed.

Bifurcation angle The influence of the bifurcation angle (i.e. the angle between the common carotid axis and the internal carotid axis) was investigated by Perktold *et al.* (1991b) and Rindt *et al.* (1994). It was found that with decreasing bifurcation angle a radial and temporal decrease of the reversed flow region occurs. Moreover, the velocities get less negative for decreasing bifurcation angles. The secondary velocities are smaller for decreasing bifurcation angles and as a result the C-shaped form of the axial velocity contours at end-systole gets less pronounced. It should be noted that decreasing the bifurcation angle with 15° only slightly influences the global flow phenomena (Rindt, 1994).

1.3 Model simplifications

In this section the model simplifications used in the present study, are described. The main interest will be on the effects of a stenosis and of a variation of the inflow conditions on the axial and secondary velocity fields. All other parameters, that can possibly influence the velocity field are kept constant and if possible are simplified for convenience. Therefore at this stage of the study, we restrict ourselves to rigid walls and Newtonian fluid behavior.

To study the 3D time-dependent flow field experimental and numerical techniques are used. The geometrical models and the flow conditions, used in the experiments and computations, are described next.

Modeling of the geometry   The geometry of the non-stenosed carotid artery bifurcation is based upon data of Bharadvaj (1982ab), who determined a standard geometry from over 100 angiograms (see also figure 1.1). To reduce the complexity of the in vivo situation, the author modeled the main branch and both daughter branches as straight tubes with circular cross-sections, which were supposed to be situated in one plane.

This non-stenosed bifurcation is used as a starting point for the geometry of the stenosed bifurcation. The shape of the stenosis is simply superimposed. A case study in cooperation with the department of physiology of the University of Limburg (Maastricht) was performed to determine the shape of the stenosis. Eighteen angiograms from 36 patients with neurologic failures were studied. Angiograms with complete occlusion, very irregular vessel walls and very complicated stenotic lesions were not taken into account. The shape of the stenoses was studied on the basis of longitudinal cross-sections of the bifurcation. From this case study it appeared that all stenoses are located at the non-divider wall of the carotid sinus and that there is a large diversity in the shape of stenoses. Nevertheless three main categories of stenoses can be distinguished: sharp-edged stenoses which are directed either (*i*) downstream or (*ii*) upstream, and (*iii*) smooth symmetrical stenoses. The smooth symmetrical stenosis was found to be most frequently present (44%), followed by the sharp edged downstream directed one (39%). Because of its geometrical simplicity for our experiments the sharp edged stenosis, that was directed downstream, is chosen. The resulting geometry is shown in figure 1.2 (left). The cross-sectional arterial lumen is chosen to be circular (see figure 1.2, right), since Zarins *et al.* (1983) and Ku *et al.*
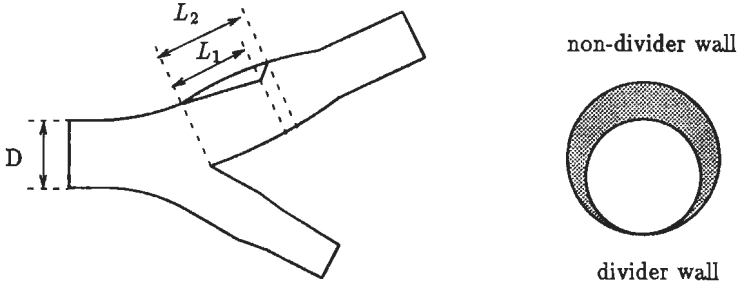
Figure 1.2: *Geometry of the 25% stenosed bifurcation in the plane of symmetry (left) and a cross-sectional view of the stenosed carotid sinus (right).*

(1985b) showed that this cross-sectional lumen remains approximately circular for moderately stenosed arteries. The area reduction of the cross-sectional arterial lumen amounts 25%. In the plane of symmetry the stenosed wall is formed by two intersecting straight lines. The sharp edge is somewhat rounded with a radius of $D/8$. The top of the stenosis is reached at $L_1 = 5D/4$ and the end of the stenosis is positioned at $L_2 = 11D/8$, where D represents the diameter of the common carotid artery.

Modeling of the flow pulse In section 1.2 it was shown that unsteadiness of flow significantly influences the flow phenomena in the carotid artery bifurcation. Therefore in the present study only pulsatile flow conditions are considered. A typical example of carotid artery flow is given in figure 1.3 (left), where the instantaneous flow rate during the cardiac cycle is presented, as measured by Ku *et al.* (1985b). The flow pulse consists of a systolic and a diastolic phase. In the first half of systole the flow accelerates to about 2.5 times its mean value, followed by a deceleration in the second half of systole. During diastole two smaller peaks in the flow rate occur and gradually a steady flow develops towards the end of diastole. The carotid artery flow can be characterized by the three dimensionless parameters as given in equation 1.1. Though literature shows a considerable variation of the parameter values (see also table 1.1), typical values for Reynolds number and the frequency parameter in the carotid artery bifurcation are: $Re_{diastole}=300$, $Re_{systole}=1000$ and $\alpha=6$. The physiological flow division ratio γ varies in time and amounts 0.45 at peaksystole, whereas for the temporal mean over the flow cycle a value of 0.30 is found (Ku *et al.*, 1985b). In the present study the flow ratio has been kept approximately constant at values of 0.35 or 0.45.

In the present study the physiological pulsatile flow is modeled by the simplified flow pulse as given in the center plot of figure 1.3. The simplified flow pulse has a cosine shape during systole, which is superimposed on a constant, diastolic flow. The definition of the simplified flow pulse offers the possibility to determine the influence of well-defined variations in the shape of the flow pulse on carotid artery flow. For that purpose the
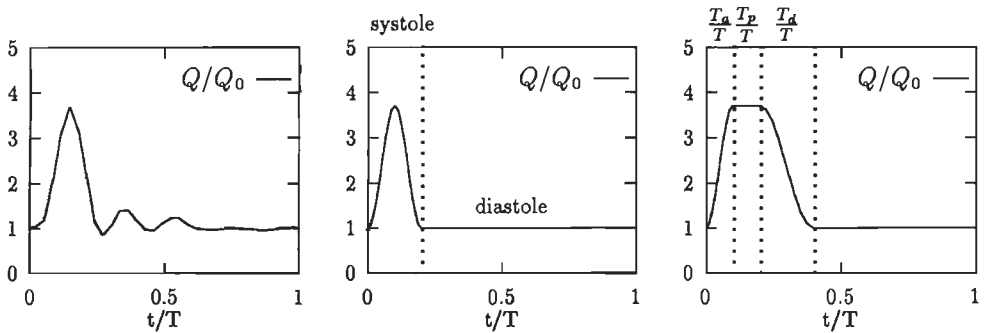
Figure 1.3: *Representations of the physiological flow pulse according to Ku et al. (1985b) (left), the simplified flow pulse, used in the present study (center) and the definition of parameters that are used to vary the shape of the flow pulse (right). All flow pulses have been made dimensionless with the end-diastolic flow rate Q_0.*

parameters T_a/T, T_p/T and T_d/T, defining the shape of the flow pulse are introduced and represented in the right plot of figure 1.3. The parameters T_a/T and T_d/T represent the relative systolic acceleration and deceleration time of the flow, whereas T_p/T represents the time between the systolic acceleration and deceleration. During the experimental and computational investigations, these parameters will be varied independently. In chapter 2 more attention will be paid to this subject.

1.4   Outline of the study

In this study the influence of a minor stenosis (25% area reduction) on carotid artery flow is studied by comparing experimental and computational results for the two cases under well-controlled, identical conditions. Two experimental techniques, hydrogen-bubble visualization and laser Doppler anemometry (LDA), and a computational (finite element) method have been used for that purpose.

To begin with, hydrogen-bubble visualization experiments have been performed, which are described in chapter 2. The visualization method has the advantage of giving a quick overview of large flow disturbances that occur in the carotid artery bifurcation. Though the visualization results can only be considered qualitatively, due to buoyancy and inertia forces acting on the hydrogen bubbles, the method appears to be very appropriate for the investigation of the influence of the stenosis in the flow field globally, thus showing the most striking features that are influenced by the stenosis. It is shown that the shear layer at the boundary of the reversed flow region plays a crucial role during flow deceleration and in the initial phase of diastole. In chapter 2 also the influence of the flow conditions on the shear layer behavior is described.

Next in chapter 3 finite element computations are considered, giving a description of the

total three-dimensional time-dependent flow field. The advantages of using this numerical method are: (*i*) performing one computation yields the fully 3D time-dependent axial and secondary flow fields, avoiding the very time-consuming and cumbersome process of experimentally measuring three velocity components at the entire 3D geometry; (*ii*) it is relatively easy to vary the geometrical and inflow conditions. However, it is a priori not evident whether the computational method describes all relevant physical phenomena adequately. Therefore, additional accurate experiments are indispensable.

In chapter 4 the LDA experiments are described, that have been performed under similar conditions as the computations. For reasons mentioned above, the measurements have been limited to a number of lines. The selection of the lines is based on the results of the hydrogen-bubble experiments. As far as the influence of the 25% stenosis is concerned, the role of the shear layer behavior will again be emphasized during these experiments. The results of the LDA experiments have also been used for a comparison of the experimental and computational results, which is described in chapter 5.

In the chapters 2 to 5 the methods with which the axial and secondary flow fields are investigated are described and the results are presented. The next chapters will go into the subjects of unsteady shear flow and the relevance of the measurements with respect to the detection of minor stenoses.

Since the role of the shear layer appears to be essential, a model study on unsteady shear layer behavior is presented in chapter 6. Here the complex 3D geometry has been simplified to 2D parallel channel flow. The study of the unsteady shear layer behavior under pulsatile flow conditions is used to obtain detailed information with respect to the vortex formation, that might be expected in the 2D shear layer.

Chapter 7 deals with the investigation of methods that can trace the differences between the non-stenosed and the stenosed geometries in order to obtain parameters that describe the influence of the stenosis. Finally, in chapter 8 the clinical applicability of the detection parameters is discussed and conclusions are drawn.

Chapter 2

Visualization studies

2.1 Introduction

The hydrogen-bubble visualization method is widely used to provide qualitative information of the flow field in space and time, and has been described in detail by Schraub *et al.* (1965). The principle of this visualization technique is that very small hydrogen bubbles (in the order of 5 - 50 μm), generated at a fine wire (10 - 50 μm) approximately follow the local fluid motions thus visualizing unsteady flow phenomena. The predominant force on the bubbles is the drag due to the local fluid motion. The hydrogen-bubble visualization method is very suitable for the detection of large coherent structures. However, the method has also some limitations: (*i*) because of the virtual inertia of the bubbles there is a limit to the frequency of velocity fluctuations that can be visualized appropriately, (*ii*) the size of the bubbles determines the spatial resolution of the method and (*iii*) buoyancy forces, being proportional to the square of the diameter of the bubbles, cause the bubbles to be displaced from the fluid path lines, thus introducing an uncertainty in the visualization.

To investigate the global flow features in the carotid artery bifurcation this hydrogen-bubble visualization method is used. In section 2.2 the experimental methods including the fluid circuit, the hydrogen-bubble generation and the experimental procedure are presented. The results of the visualization studies are described in section 2.3 by first considering the influence of a stenosis on the flow phenomena and next studying the influence of the inflow conditions. In section 2.4 the experimental results will be discussed and finally some concluding remarks are made (section 2.5).

2.2 Experimental method

Experimental setup

A schematic representation of the experimental equipment is given in figure 2.1. The flow system provides steady fluid flow between two tanks with a constant fluid level. A valve with a controllable cross-sectional opening is used to obtain an unsteady flow (see
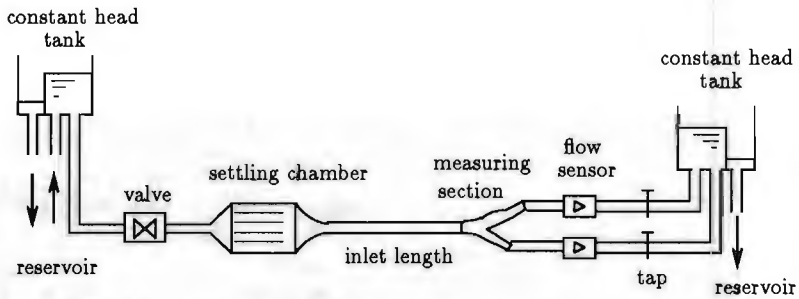
Figure 2.1: *Schematic representation of the experimental equipment.*

also Palmen *et al.* (1993)). Fluid from the upstream tank is passed through a number of flow straighteners and a settling chamber to break up the vortices and to provide a stable flow at the entrance of the inlet tube. An inlet tube with a length of approximately $30D$ is used to ensure a fully developed velocity field in the measuring section. Here D represents the diameter of the common carotid artery, being $D = 40\,mm$. In both daughter branches the flow is measured with electromagnetical flow sensors (Skalar-instruments, transflow 601). For that purpose a physiological salt solution (a solution of 0.9 weight percent NaCl in water) is used as measuring fluid. The flow signals are amplified with a differential amplifier, digitized by means of an A/D-converter and processed with the aid of a personal computer. The flow ratio between the two branches can be adjusted by means of taps in the internal and external arteries. After the fluid passes the downstream tank it is collected in a large reservoir from which the upstream tank is refilled again.

The models of the 0% and 25% stenosed carotid artery bifurcations that are used in the hydrogen-bubble experiments, are 5:1 enlarged models of the physiological case with a geometry as described in chapter 1. The experimental models are constructed of Poly Methyl MethAcrylate (PMMA, usually referred to as plexiglass). To create them a three-dimensional description of the bifurcation surface is generated with a CADCAM-program (Cadkey), that also produces the data for the control of a milling machine. After the two halves of the raw plexiglass model are constructed, the surfaces are polished with sandpaper and brass-polish and the complete three-dimensional model is assembled. The CADCAM-program offers also the possibility to use identical models for the experiments and the finite element calculations as described in the next chapter.

Hydrogen-bubble generation

In order to generate the hydrogen bubbles three platinum cathode wires and a gilded anode (diameter 4 mm) are mounted in the plane of symmetry in the measuring section. The three cathode wires are positioned at sites I_{05}, I_{10} and I_{15} ($0.5D, 1.0D$ and $1.5D$ downstream the apex respectively, see also figure 2.2), whereas the anode is positioned far more downstream (at $11D$ downstream the apex). Supplying voltage to the system causes
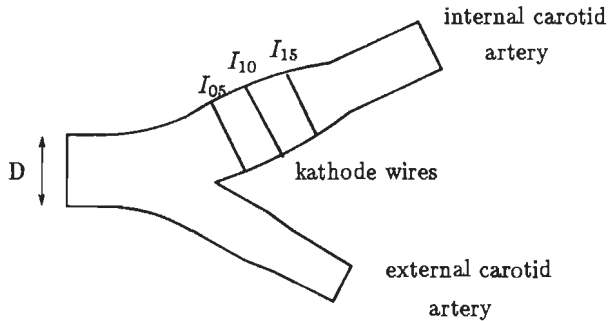
Figure 2.2: *Positions of the three cathode wires at sites I_{05}, I_{10} and I_{15} the hydrogen-bubble visualizations.*

the production of hydrogen bubbles at the cathode through electrolysis, whereas oxygen is released at the anode. The hydrogen bubbles are kept as small as possible for the following reasons: (i) to reduce the effects of buoyancy forces, (ii) to increase the spatial resolution and (iii) to increase the maximum frequency that can be followed by the bubbles. This is achieved by chosing small cathode wires (diameter 20 μm) and a low voltage (30 V). Since the voltage is supplied in the form of square-wave pulses with a frequency of 2.3 Hz and a duration of 0.12 s, discrete lines of bubbles are formed. The onset of each series is triggered by the controller of the flow pulse. Thus, the generation of the hydrogen bubbles starts at the onset of the flow pulse and it lasts until half of the diastolic phase. The hydrogen bubbles are made visible by illuminating the measurement section from the back side at an angle of approximately 20 degrees with respect to the vertical. The hydrogen-bubble profiles have been recorded on video tape.

Experimental procedure

First hydrogen-bubble visualizations have been performed in the non-stenosed and the 25% stenosed model of the carotid artery bifurcation for a Reynolds number varying from 400 at end-diastole up to 1200 at the peak-systole of the flow pulse. Two shapes of the flow pulse as described in section 1.3, are used: (i) a simplified flow pulse and (ii) a physiological flow pulse (see also figure 2.3). The Womersley parameter, based on the fundamental harmonic amounts $\alpha = 6$ for both cases. The flow ratio is almost constant during the flow pulse, being $\gamma = 0.45$. The results of the hydrogen bubble profiles for the non-stenosed and the 25% stenosed bifurcation are compared in order to determine the influence of the geometric variation of the 25% stenosis and are discussed in section 2.3.1.

Next the influence of variations in the shape of the flow pulse is determined. For that purpose the simplified flow pulse has been used. In order to determine the influence of the shape of the flow pulse, the parameters $T_a/T, T_d/T$ and T_p/T have been varied
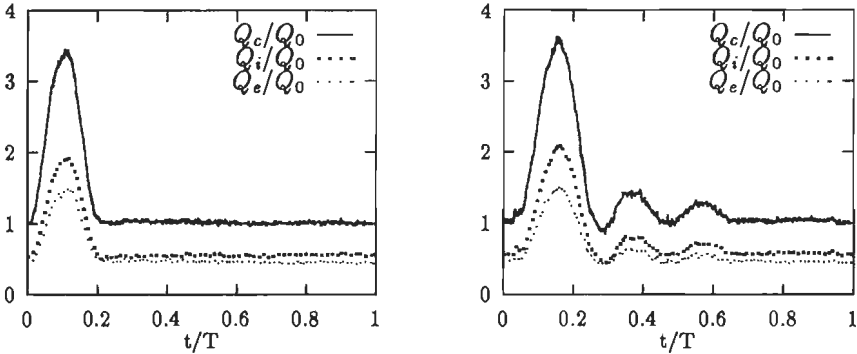
Figure 2.3: *Two kinds of flow pulses that are used in our experiments: (left) simplified pulse, (right) physiological pulse. The time and flow have been made dimensionless with respectively the period time $T = 69.3\,s$ and the end-diastolic flow rate through the communis $Q_0 = 0.5\,l/min$.*

independently. The parameters T_a/T and T_d/T represent the relative systolic acceleration and deceleration time of the flow, whereas T_p/T represents the time between the systolic acceleration and deceleration as defined in section 1.3. Also the influence of Re, α and γ on the flow phenomena has been determined. An overview of the parameters that have been varied for the simplified pulse is given in table 2.1. The parameters that mark the reference situation are printed in bold type. The visualization results for the varying inflow conditions are described in section 2.3.2.

Parameter	Values
Reynolds number range $Re_{end-diast} - Re_{peak-syst}$	215-800, **270-1000**, 400-1200
Womersley parameter (α)	4, **6**, 8
flow ratio (γ)	0.30, **0.45**
relative systolic acceleration time (T_a/T)	0.05, **0.1**, 0.2
relative systolic deceleration time (T_d/T)	0.05, **0.1**, 0.2
relative peak-systolic time (T_p/T)	**0**, 0.0156, 0.0312, 0.0625

Table 2.1: *Parameters of the simplified pulse that are used in the experiments.*

2.3   Results

2.3.1   Visualization in a 0% and 25% stenosed bifurcation

The hydrogen-bubble profiles as a function of time will be described for the non-stenosed and the 25% stenosed models of the carotid artery bifurcation. First the results for the simplified flow pulse are described ($T_a/T = T_d/T = 0.1$ and $T_p/T = 0$) with a Reynolds number varying from 400 at end-diastole up to 1200 at peak-systole. The other parameters amount $\alpha = 6$ and $\gamma = 0.45$. The left-hand side pictures of figure 2.4 represent the visualization results in the non-stenosed bifurcation for several phases of the flow pulse, which will be considered first. The times for which the results are presented are also given in figure 2.4. At peak-systole ($t/T = 0.1$) the axial velocities in the plane of symmetry are positive over the entire profile with higher values near the divider wall. High shear rates are found near the divider side wall and low shear rates occur near the non-divider side wall. During systolic deceleration ($0.1 < t/T < 0.2$) an area of low shear rates is formed near the non-divider side wall of the bifurcation. At $t/T = 0.15$ the high velocities at the divider wall are more pronounced and the onset of a shear layer (i.e. a layer where large axial velocity gradients in radial direction occur) near the centerline of the carotid sinus can be found. In the low-shear region the velocities are relatively low but still positive. At the end of systolic deceleration ($t/T = 0.2$) small negative velocities in the low-shear region occur. The shear layer becomes more definite and is shifted towards the divider side wall. In the initial phase of diastole ($t/T = 0.23$) the shear layer becomes unstable and a small vortex is formed near site I_{15} (this is difficult to see in figure 2.4). In the next period of time this vortex is convected downstream and at $t/T = 0.26$ a new stronger vortex is formed more upstream at site I_{10}. In the central part of the low-shear region positive axial velocities can be seen again. At time $t/T = 0.29$ the vortex has grown and convected downstream and the shear layer stabilizes again. During the period from $t/T = 0.29$ up to end-diastole a smooth transition from the existing velocity field to the end diastolic velocity field is found and the shear layer gradually becomes less definite.

   The visualization results for the 25% stenosed carotid artery bifurcation model (right-hand side pictures of figure 2.4) show features, that are very similar to the non-stenosed case. All phenomena described above, can also be seen in the 25% stenosed bifurcation, like the occurrence of the low velocity area during systolic deceleration and the existence of a shear layer with two clearly visible vortices at $t/T = 0.23$ and $t/T = 0.26$. Only some small differences can be seen in the *position* and the *stability* of the shear layer. The influence of the stenosis on the *position* of the shear layer is expressed by a slight shift of the shear layer at some phases of the flow pulse. This shift is not unique, since for example at $t/T = 0.15$ the relative position of the shear layer is closer to the non-divider wall, coupled with a relative smaller low velocity area in the 25% stenosed case; in contrast to this at $t/T = 0.29$ the shear layer occurs at a position, which is relative closer to the divider wall for the 25% stenosed case. In short, there is no unique influence of the presence of the stenosis on the position of the shear layer. The influence of the stenosis on the *stability* of the shear layer can be seen at $t/T = 0.23$, where the vortex seems to be more clear in
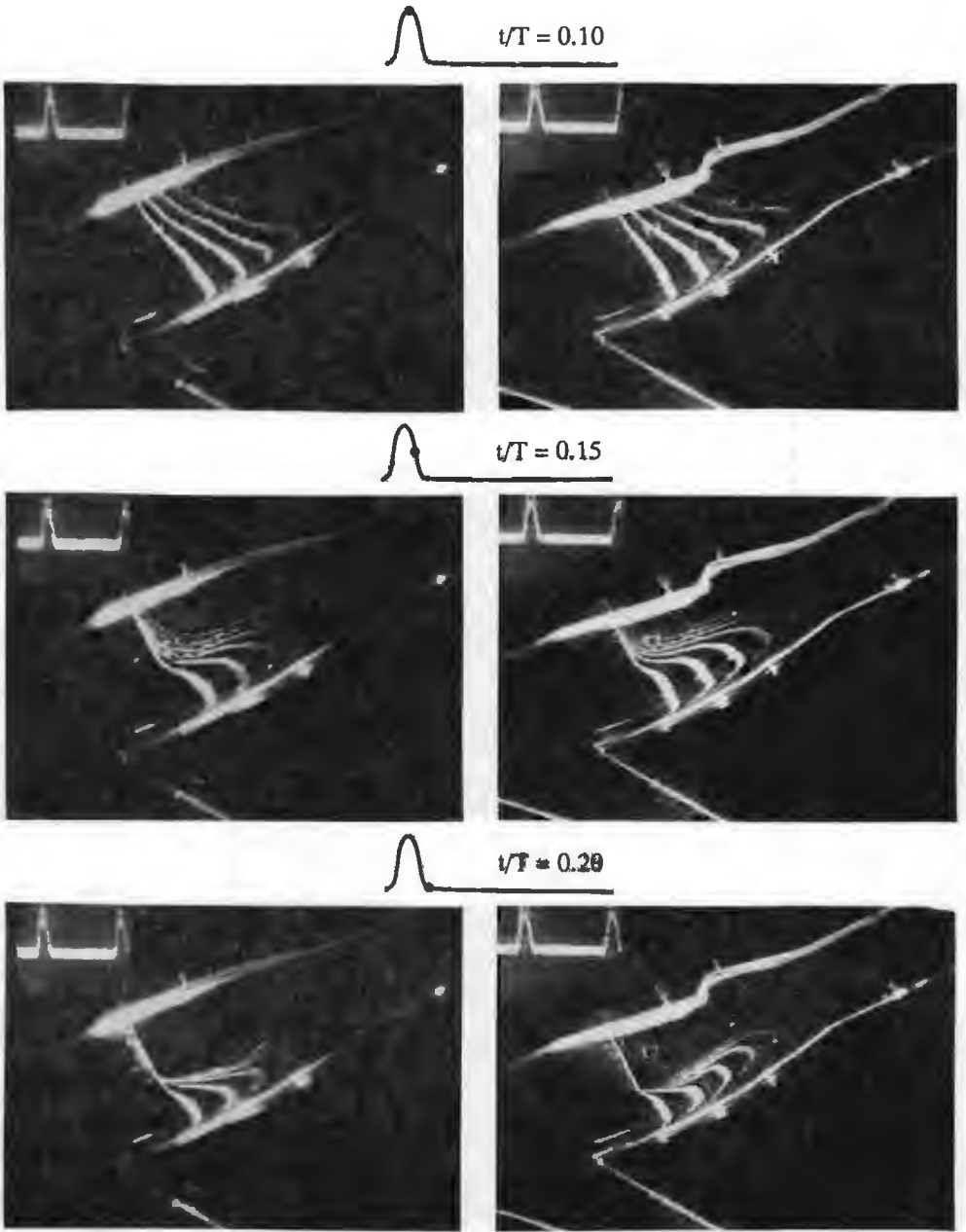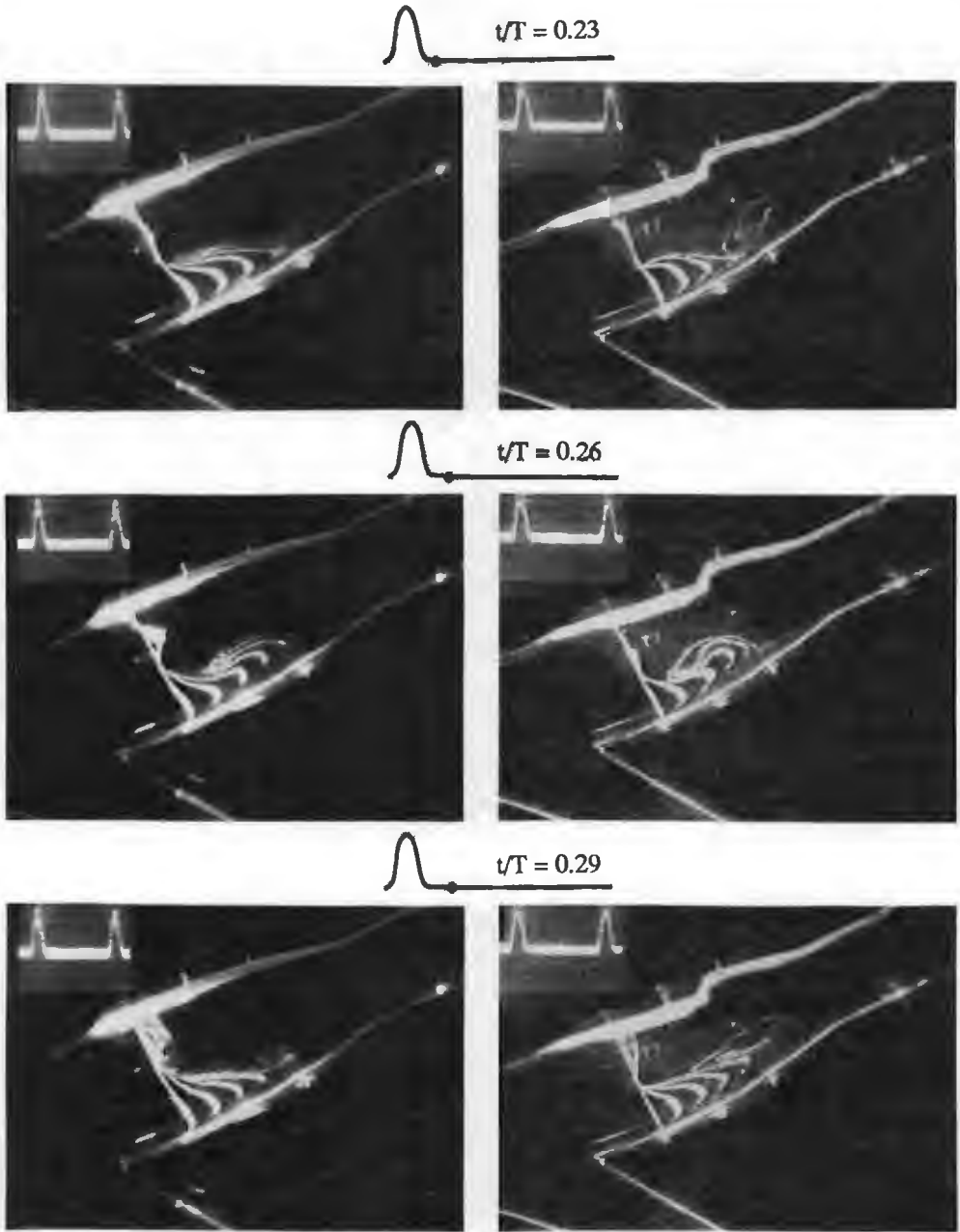
Figure 2.4: *Hydrogen-bubble visualization for a non-stenosed bifurcation (left) and a 25% stenosed bifurcation (right) at several phases of the flow pulse ($Re_{systolic} = 1200$, $\alpha = 6$ and $\gamma = 0.45$).*

$t/T = 0.23$

$t/T = 0.26$

$t/T = 0.29$

(Figure 2.4 continued)

the stenosed case. Moreover, at $t/T = 0.26$ the shape of the formed vortex structure is different for the stenosed and the non-stenosed case. Also the axial velocity gradient in radial direction in the shear layer seems to be slightly larger in the stenosed case as can be seen for example at time steps $t/T = 0.23$ and 0.29.

Also experiments with a physiological flow pulse have been performed for both the non-stenosed and stenosed model. The results resemble the case of the simplified flow pulse. Apparently, the precise shape of the flow pulse during diastole is of minor influence on the visualization phenomena and the simplified flow pulse may be considered as a good approximation of the physiological flow pulse.

2.3.2   Visualization results at various inflow conditions

The shape of the flow pulse is determined by the parameters $T_a/T, T_d/T$ and T_p/T. The influence of each parameter is briefly discussed. The other flow parameters are kept constant at a value of $Re_{diast} = 270, Re_{syst} = 1000, \alpha = 6$ and $\gamma = 0.45$ (reference situation). The most important results from the hydrogen-bubble visualizations will be reported here, without showing the many video prints. In general the evolution of the hydrogen-bubble profiles from the previous section will be a good guide for understanding the following investigations.

Relative systolic acceleration time (T_a/T): The relative systolic acceleration time has been varied between 0.05 and 0.2, while $T_d/T = 0.1$ and $T_p/T = 0$. For a slowly accelerating flow $(T_a/T = 0.2)$ the formation of the low-shear region with low axial velocities takes place during late systolic acceleration. Thus, at peak-systole a low-shear region already has formed, which is earlier than in the reference situation. During systolic deceleration the velocities in the low-shear region become negative and a very steep gradient of the axial velocities is observed at site I_{10}. Shortly after that two vortices develop in the shear layer, which grow and are convected downstream. Subsequently the flow stabilizes to a quasi-static diastolic state.

For a fastly accelerating flow $(T_a/T = 0.05)$ no low-shear region is formed during systolic acceleration. At peak-systole the axial velocities in the carotid sinus are positive at any location in the plane of symmetry, whereas for the reference situation at this time step low shears were already present at the non-divider wall. During systolic deceleration a low-shear region is formed. The velocities in this region near site I_{05} are negative and the gradient of the shear layer is large here. No vortex formation can be distinguished in the shear layer, but a rotating motion of the fluid in the plane of symmetry is found in the low-shear region (see also the left picture of figure 2.4, where the visualization is given at $t/T = 0.18$, being $t/T = 0.03$ after the onset of diastole).

Conclusion: for larger values of the relative systolic acceleration time (i) the shear layer is more pronounced and (ii) is located at a greater distance from the divider wall than for smaller values of T_a/T, and (iii) vortex formation becomes more important.
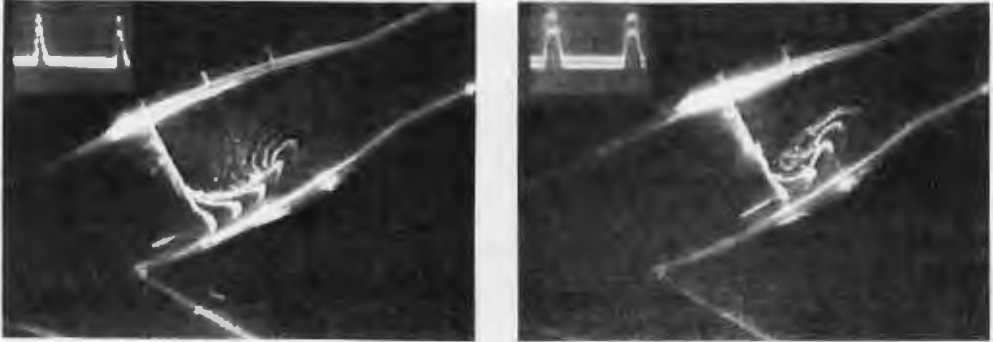
Figure 2.4: *Hydrogen-bubble visualization in the non-stenosed bifurcation at $t/T = 0.03$ after the onset of diastole for the experiment with $T_a/T = 0.05$ at $t/T = 0.18$ (left) and for the experiment with $T_p/T = 0.063$ at $t/T = 0.29$ (right).*

Relative systolic deceleration time (T_d/T): The systolic deceleration has been varied between 0.05 and 0.2. The other parameter values are $T_a/T = 0.1$ and $T_p/T = 0$. For a slowly decelerating flow $(T_d/T = 0.2)$ a low-shear region with negative velocities develops during systolic deceleration. At the end of systolic deceleration the gradient of the axial velocity in radial direction is larger at site I_{10} compared to the reference situation. Shortly after that vortex formation occurs.

For a fastly decelerating flow $(T_d/T = 0.05)$ the low-shear region appears to be larger in comparison with the reference situation. The velocities in the low-shear region seem to be smaller and the gradient of the axial velocities is smaller. No vortex formation is found for this case.

Conclusion: an increasing relative systolic deceleration time T_d/T results in (i) a slightly smaller reversed flow region with larger negative velocities in this region, (ii) a more pronounced shear layer and (iii) a more significant vortex formation.

Relative peak-systolic time (T_p/T): T_p/T has been varied from $T_p/T = 0.016$ to $T_p/T = 0.063$ while $T_a/T = T_d/T = 0.1$. For a flow pulse with a small peak-systolic time $(T_p/T = 0.016)$ the axial velocities are positive during systolic acceleration. During the systolic plateau the formation of a low-shear region with nearly zero axial velocities can be seen. Compared to the reference situation the low-shear region has more time to evolve to the (quasi-)steady flow situation. During systolic deceleration the velocities in the low-shear region become negative. The experiments do not show the formation of a localized vortex in the shear layer, but a rotating motion of the fluid in the low-shear region occurs.

For a flow pulse with a large peak-systolic time $(T_p/T = 0.063)$ the axial velocities are also positive during systolic acceleration and during the systolic plateau a low-shear region is formed, which approximates a steady flow situation quite well. During

systolic deceleration the gradient of the axial velocity is large near sites I_{05} and I_{10}. The position of the shear layer appears to be located more towards the divider wall during the vortex formation. Two clearly visible vortex formations, whose origins are located in the shear layer, can be seen shortly after systolic deceleration (one of them is shown in figure 2.4, where the situation is given at $t/T = 0.29$, being $t/T = 0.03$ after the onset of diastole).

Conclusion: for increasing T_p/T (i) the gradient of the axial velocity in the shear layer is larger, (ii) the position of the shear layer is closer to the divider wall during the vortex formation and (iii) the formation of vortices in the shear layer is more pronounced.

In the above it has been shown that there is a relevant influence of the parameters $T_a/T, T_d/T$ and T_p/T (i.e. the shape of the flow pulse) on the flow phenomena that occur in the shear layer. Next the influences of the parameters Re, α and γ are considered. The shape of the flow pulse is chosen according to the reference situation as presented in figure 2.3 (left) with $T_a/T = T_d/T = 0.1$ and $T_p/T = 0$.

Reynolds number: Experiments have been performed for ranges of the Reynolds number $Re = 215 - 800$, $Re = 270 - 1000$ and $Re = 400 - 1200$ (varying from diastole to peak-systole), while $\alpha = 6$ and $\gamma = 0.45$. At $Re = 215 - 800$ a low-shear region with nearly zero axial velocities is formed near the non-divider wall during systolic deceleration. In contrast to the reference situation no negative velocities occur, no clearly visible shear layer can be seen and no vortex formation is found.

At $Re = 400 - 1200$ the low-shear region, that develops during systolic deceleration, is smaller compared to the reference situation. The velocities in the low-shear region are negative and a large gradient of the axial velocities at the shear layer can be seen. In the shear layer the formation of two vortices is found.

Conclusion: increasing the Reynolds number results in (i) increasing negative velocities in the low-shear region, (ii) a more pronounced shear layer that is positioned on a larger distance from the divider wall, and (iii) a more significant vortex formation.

Womersley parameter: The Womersley parameter has been varied from $\alpha = 4, 6$ to 8 with $Re_{diast} = 270, Re_{syst} = 1000$ and $\gamma = 0.45$. For $\alpha = 4$ small negative velocities are found during systolic deceleration at the non-divider side of the low-shear region. The gradient of the axial velocities in the shear layer is small at site I_{05}, whereas at site I_{10} a very large gradient is found. Vortex formation occurs at $t/T = 0.21$ near site I_{15}. For $\alpha = 8$ no negative velocities are found during systolic deceleration in contrast to the reference situation. Only nearly zero axial velocities are found. The shear layer is positioned closer to the divider wall.

Conclusion: for increasing Womersley parameters (i) the position of the shear layer during systolic deceleration is shifted towards the divider wall, (ii) the gradient of the axial velocities near the shear layer is smaller and (iii) the vortex generation is diminished.

Flow ratio: During the experiments the flow ratio γ is chosen to be 0.30 and 0.45, while $Re_{diast} = 270$, $Re_{syst} = 1000$ and $\alpha = 6$. For decreasing flow ratio, i.e. for increasing flow into the interna, the shear layer shifts to a larger distance from the divider wall. The gradient of the axial velocity appears to be smaller and the vortex generation decreases (for $\gamma = 0.30$ no generation of vortices is seen).

2.4   Discussion of the visualization results

As stated in section 2.1 the predominant force on hydrogen bubbles is the drag force due to the local fluid motion, though buoyancy forces are also present. The rise velocity u_{rise}, due to these buoyancy forces is expressed by Schraub *et al.* (1965) as

$$u_{rise} = \frac{(\rho_f - \rho_p)g}{18\nu} D_p^2, \tag{2.1}$$

where ρ_p and ρ_f represent the density of the particle and the fluid respectively, D_p the diameter of the particle (estimated to be smaller than $100\,\mu m$), g the gravitational acceleration and ν the dynamic viscosity of the fluid ($\nu = 10^{-3} Pas$). Substituting these values, it follows that $v_{rise} \approx 5\,mms^{-1}$. In the range of the axial velocities found in the experiments, this rise velocity introduces an error in the axial velocities in the order of 15 percent of the maximum axial velocities during systole (determined from the experiments for Re=400-1200). For lower axial velocities which occur in the low-shear region, during diastole or at smaller Reynolds numbers, the errors due to buoyancy forces increase. As a result there is a discrepancy between the motion of the generated hydrogen bubbles and the local fluid motion. Despite these relatively large error estimates the experiments still give important and meaningful qualitative information about the large scale flow phenomena. Firstly, since the differences between the non-stenosed and 25% stenosed geometry are concerned under similar conditions, the changes in flow phenomena due to the geometric change can still be detected in a meaningful way. Secondly, the question arises whether the buoyancy forces might induce any vortex-like motions of the bubbles. Here it will be shown that this is not the case. Consider a single hydrogen bubble that exists in the shear layer during diastole. Due to the buoyancy force the bubble will rise and when it enters the reversed flow region, its path might become curved backwards. But its motion will never resemble a vortex, because the buoyancy force acts solely in the gravitational direction. Thus, an observed vortex is essentially caused by a local rotational fluid motion.

The maximum frequency response of hydrogen bubbles f_{max} is derived by Hinze (1975) as

$$f_{max} = 0.023 \frac{36\nu}{(2\rho_p + \rho_f)D_p^2}, \tag{2.2}$$

where ρ_p, ρ_f, D_p and ν are defined as mentioned above. Substitution of $D_p = 100\,\mu m$ and $\nu = 10^{-3} Pas$ results in $f_{max} \approx 80\,Hz$. Thus, the particles follow high frequency disturbances quite adequately. During the hydrogen-bubble visualization however the identification of the individual bubbles is hardly possible, due to the chosen line-wise flow

visualization technique. Therefore, it is not possible to find small local velocity oscillations of high frequency in the flow field.

In the hydrogen-bubble visualizations vortex formation occurs in the initial phase of diastole. This vortex formation shows a similarity with the visualization experiments of Ku *et al.* (1983), who also reported on a vortex at the boundary of the low velocity region near the divider wall at the onset of diastole. It is interesting to note that Van Merode *et al.* (1985) also report on abnormalities in the velocity profiles, even with small negative axial velocities, near the divider side of the carotid sinus after systolic deceleration. It is not clear whether these findings originate from the same fluid dynamical phenomena as in our experiments.

From the visualization results of sections 2.3.1 and 2.3.2 it is clear that the hydrogen-bubble visualizations give an excellent overview of the evolution of the large scale flow disturbances that occur in the shear layer of the carotid artery bifurcation. Some important findings are discussed below.

- As mentioned in the introduction and confirmed by the experiments, the stenosis is located in a region with low velocities. As a result no local vortex shedding down-stream the stenosis occurs. This phenomenon would be expected when the stenosis was located in the main flow as we know from the many studies on steady and pulsatile flow in axisymmetric narrowed tubes (Cassanova *et al.* 1978, Khalifa *et al.* 1981, Ahmed *et al.* 1983a,b and 1984). In those studies essential different phenomena were found during pulsatile flow compared to steady flow experiments. Two phenomena appeared to be important: vortex shedding downstream the stenosis at peak-systole and disturbances occurring during the deceleration phase of the flow pulse. The first phenomenon appeared to become more pronounced when the pulse frequency was increased. In all experiments the stenosis was located in the main flow, i.e. there was a relatively large axial wall shear stress. Since in the present study the stenosis is located in a region with low velocities and low shear stress, the axial wall shear stress at the top of the stenosis is very small and no significant vortex shedding from the rear edge of the stenosis will occur.

- From our experiments it appears that large scale instabilities occur in the shear layer, which separates the low-shear region from the high-shear region. It has also been shown that these instabilities are only slightly influenced by a 25% stenosis. A small influence can be seen on the position of the shear layer and the shape of the vortex structures that occur in the shear layer. The influence of the shape of the flow pulse appears to be more pronounced. Parameters like $Re, \alpha, T_a/T, T_d/T$ and T_p/T influence the development of the shear layer and the formation of vortices in the initial phase of diastole. This can be understood in the following way. For increasing relative peak-systolic time (T_p/T) and decreasing relative acceleration time (T_a/T) the formation of the low-shear region with nearly zero axial velocities at the non-divider wall becomes more pronounced in the carotid sinus. As a consequence the gradient of the axial velocity in radial direction is already large before the onset of systolic deceleration. During systolic deceleration an adverse pressure gradient results

in negative velocities in the low-shear region and a clearly visible shear layer with a large gradient of axial velocities is formed. From the theory of hydrodynamic stability it is known that such large gradients may lead to shear layer instabilities. These shear layer instabilities are assumed to be related to Kelvin-Helmholtz instabilities which are analyzed by Drazin and Reid (1981) for 2D steady flows in incompressible inviscid fluids. In chapter 6 more attention will be paid to this phenomenon.

It has been found that the vortex formation in the shear layer becomes more clear with increasing Reynolds number and decreasing Womersley parameter. The question arises whether the parameters Re and α, being the ratio between the steady and viscous forces (Re) and the ratio between the unsteady and viscous forces (α), are the most appropriate dimensionless numbers to describe the shear layer behavior. Assumed that the viscous forces are of minor importance compared to the steady and unsteady inertia forces, it is more likely that the Strouhal number $Sr = \omega D/U$, being the ratio between the unsteady and steady inertia forces, is a more significant parameter that describes the unstable shear layer behavior. The Strouhal number is dependent on α and Re and can be expressed as $Sr = 4\alpha^2/Re$. From the experiments we know that local vortex formation becomes more clear with increasing Re and decreasing α. Thus, it follows that vortex formation is more pronounced for decreasing Strouhal number, at least for the range of Strouhal numbers investigated.

Though it is not shown in the pictures of figure 2.4, the hydrogen-bubble experiments indicate that the particle paths of the hydrogen bubbles remain in the plane of symmetry, i.e. the bubbles do not leave this plane. This justifies the assumption that the flow in the models of the carotid artery bifurcation can be considered as a symmetrical flow problem.

From the hydrogen-bubble visualizations it appears that the influence of a 25% stenosis is relatively small compared to the influence of the inflow conditions and should be found in the shear layer. As the visualization studies only give qualitative information on the velocities in the plane of symmetry, it is useful to quantify the results with other methods. Moreover, additional information of axial velocities outside the plane of symmetry and quantitative information about axial and tangential velocities can be gained then. To map the total three-dimensional time-dependent flow field in the non-stenosed and the 25% stenosed carotid artery bifurcations, finite element computations have been performed and will be described in the next chapter. The information on the importance of the evolution of the shear layer, gained in the hydrogen-bubble experiments, has been used as a guideline for further experimental analysis by means of laser Doppler anemometry (see chapter 4).

2.5   Concluding remarks

In this chapter hydrogen visualizations of the flow in a non-stenosed and a 25% stenosed carotid artery bifurcation model are described. The experiments show that shortly after the onset of diastole vortex formation occurs in a shear layer, being the interface between a region with low shear rates at the non-divider wall and a region with high shear rates near the divider wall. Comparison of the hydrogen bubble profiles in the 0% and the 25%

stenosed models with similar flow conditions shows that the 25% stenosis only slightly influences the flow phenomena. The most striking influences are found in the stability of the shear layer.

In order to gain insight into other parameters that are important with respect to the stability of the shear layer, also experiments have been performed in which the influence of the inflow conditions (i.e. parameters T_a/T, T_p/T, T_d/T, Re, α and γ) on the flow phenomena is studied. It has been shown that relatively small changes in the inflow conditions influence the stability of the shear layer more than the presence of a 25% stenosis. Since the main objective of this study is to investigate the influence of a minor stenosis on the flow field, it is essential to chose well-defined inflow conditions. Therefore, in the sequel of this study the simplified flow pulse with a shape according to the reference situation (figure 2.3, left) with shape parameters $T_a/T = T_d/T = 0.1$ and $T_p/T = 0$ will be considered.

Chapter 3

Finite element computations

3.1 Introduction

As argued in chapter 1, computational methods play an important role in the analysis of complex three-dimensional time-dependent flow fields. In this chapter computations of the velocity field have been performed using a finite element method to solve the system of fluid equations. More detailed information about the method can be found in Cuvelier *et al.* (1986) and Van de Vosse *et al.* (1986,1987). A description of the application to the flow in three-dimensional non-stenosed models of the carotid artery bifurcation is given by Rindt (1989). In this study the computational method is used for the analysis of the flow in stenosed models. An extended description of the computational results of the flow in a 25% stenosed bifurcation model as compared to a non-stenosed model will be given in section 3.3. The chapter will be completed with a discussion of the numerical results in section 3.4.

3.2 Numerical method

Spatial discretization of the unsteady Navier-Stokes equations

The unsteady Navier-Stokes equations and the continuity equation for incompressible, isothermal fluids can be written as:

$$\frac{\partial \vec{u}}{\partial t} + \vec{u} \cdot \vec{\nabla}\vec{u} - \vec{\nabla} \cdot \boldsymbol{\sigma} = \vec{f}, \tag{3.1}$$

$$\vec{\nabla} \cdot \vec{u} = 0, \tag{3.2}$$

with $\vec{u}$ the velocity vector, $\vec{f}$ the body force per unit mass, $\partial \vec{u}/\partial t$ the local time derivative of the velocity, $\vec{\nabla}$ the gradient operator and $\boldsymbol{\sigma}$ the Cauchy stress tensor. For Newtonian fluids with constant dynamic viscosity η the following constitutive equation holds:

$$\boldsymbol{\sigma} = -p\boldsymbol{I} + \eta(\vec{\nabla}\vec{u} + (\vec{\nabla}\vec{u})^T), \tag{3.3}$$
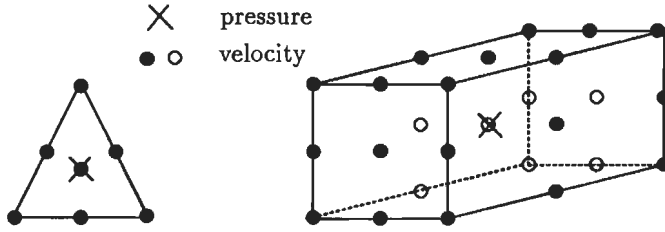
Figure 3.1: *The 7-noded (left) and 27-noded (right) Crouzeix-Raviart element, used to solve the 2D and 3D fluid motion equations respectively.*

with p the pressure. Substitution of equation 3.3 in equation 3.1 and introducing dimensionless variables yields

$$Sr \frac{\partial \vec{u}}{\partial t} - \frac{1}{Re} \nabla^2 \vec{u} + \vec{u} \cdot \vec{\nabla} \vec{u} + \vec{\nabla} p = \vec{f}, \tag{3.4}$$

$$\vec{\nabla} \cdot \vec{u} = 0, \tag{3.5}$$

where ∇^2 represents the Laplacian operator. Sr and Re denote the Strouhal number and the Reynolds number respectively, defined as $Sr = \omega L/U$ and $Re = UL/\nu$. Here L, U, and ω represent a characteristic length, velocity and angular frequency respectively and ν the kinematic viscosity. To solve equations 3.4 and 3.5 a standard Galerkin finite element method has been applied, which is implemented in the finite element package Sepran (Segal, 1984), using 27-noded Crouzeix-Raviart elements in 3D cases and 7-noded Crouzeix-Raviart elements in 2D cases (see also figure 3.1). Velocity unknowns are defined in all the nodal points of the element, i.e. there are 81 velocity unknowns per element. Pressure unknowns which are the pressure itself and its three spatial derivatives, are only defined in the center node. The accuracy is $O(\Delta x^3)$ for the velocity and $O(\Delta x^2)$ for the pressure, where Δx represents a characteristic dimension of the spatial discretization.

The spatial discretization results in the following set of non-linear first-order differential equations (Cuvelier *et al.*, 1986):

$$M\dot{u} + [S + N(u)]u + L^T p = f + b, \tag{3.6}$$

$$Lu = 0, \tag{3.7}$$

where $M\dot{u}$ represents the local acceleration term, Su the viscous term, $N(u)u$ the convective acceleration term, $L^T p$ the pressure gradient term and Lu the velocity divergence term. The body and boundary forces are represented by f and b respectively, while u and p are columns, containing the velocity and pressure unknowns in the interpolation points.

To reduce the computing time and memory a penalty function method is applied, in which the continuity equation is perturbed with a small parameter times the pressure. In

discrete form this can be written (Cuvelier *et al.*, 1986):

$$Lu = \epsilon M_p p, \tag{3.8}$$

with M_p the pressure matrix and ϵ the penalty parameter. For the problems solved in this study the value of ϵ was chosen to be $\epsilon = 10^{-6}$. Substitution of equation 3.8 into equation 3.6 leads to an uncoupling of the momentum equations and the continuity equation:

$$M\dot{u} + [S + N(u) + \frac{1}{\epsilon}L^T M_p^{-1} L]u = f + b, \tag{3.9}$$

$$p = \frac{1}{\epsilon}M_p^{-1} Lu. \tag{3.10}$$

Time integration

The local time derivative from equation 3.9 is approximated by a finite difference θ-method (Cuvelier *et al.*, 1986). Considering the equation

$$\dot{u} = f, \tag{3.11}$$

the application of the θ-method results in

$$\frac{u^{n+1} - u^n}{\Delta t} = f^{n+\theta} \quad , \text{with} \quad f^{n+\theta} = \theta f^{n+1} + (1 - \theta) f^n. \tag{3.12}$$

Here u^n is an abbreviation for $u(n\Delta t)$ with Δt the time step and θ represents a parameter in the interval $0 < \theta \le 1$. For $\theta = 1$ this scheme reduces to the Euler implicit method, having an accuracy of $O(\Delta t)$ for linear equations (i.e. f is not dependent on u). For $\theta = 0.5$ this scheme is known as the Crank-Nicholson scheme, which is $O(\Delta t^2)$ accurate for linear equations.

Both methods have the advantage of unconditionally numerical stability. However, the Euler implicit scheme is less suitable for application in simulations of flows with for example vortex shedding, because of its damping property (Van de Vosse, 1987). Therefore a Crank-Nicholson scheme ($\theta = 0.5$) is applied in this study.

The θ-method has been applied to the Navier-Stokes equations, using a two-step formulation. Besides that this two-step formulation yields a more efficient implementation, it also has superior stability properties for the pressure (Van de Vosse, 1987). The first step is an Euler implicit step to time level $n + \theta$ (where $\theta = 0.5$), which can be written as:

$$[\frac{1}{\theta \Delta t}M + S + J(u^n) + \frac{1}{\epsilon}L^T M_p^{-1} L]u^{n+\theta} = [\frac{1}{\theta \Delta t}M + N(u^n)]u^n + f^{n+\theta} + b^{n+\theta}, \tag{3.13}$$

$$p^{n+\theta} = \frac{1}{\epsilon}M_p^{-1} Lu^{n+\theta}. \tag{3.14}$$

Here, the non-linear convective term $N(u^{n+\theta})u^{n+\theta}$ is linearized by one step of a Newton-Raphson iteration scheme (Cuvelier *et al.*, 1986):

$$N(u^{n+\theta})u^{n+\theta} = J(u^n)u^{n+\theta} - N(u^n)u^n, \tag{3.15}$$

where $J(u^n)$ is the Jacobian matrix of $N(u^n)u^n$. Since the Jacobian is asymmetric, an asymmetric LU-factorization technique is used to solve the set of equations 3.13 and 3.14. The second step is an extrapolation of the velocities to time level $n+1$ as given by:

$$u^{n+1} = \frac{1}{\theta}[u^{n+\theta} - (1-\theta)u^n].$$ (3.16)

The finite element mesh

Although it is not evident a priori whether the flow may be considered symmetric with respect to the plane of symmetry, the hydrogen-bubble experiments indicate that for the physiological range of Reynolds numbers, the flow remains symmetrical. This justifies the use of only one half of the bifurcation geometry in the computations, which reduces the large number of unknowns and computations time substantially.

The carotid artery bifurcation has been divided into quadrilateral brick elements. A mesh generator, implemented in the package IDEAS (SDRC), has been used to generate a basic mesh (see left figure in figure 3.2). In the common carotid artery 15 elements are defined over the cross-section, whereas in the internal and external carotid arteries 33 and 12 elements are defined respectively. The mesh contains 11143 nodes in 1180 elements.

With the basic mesh as a starting point the meshes for the non-stenosed, the 25% stenosed and the 50% stenosed bifurcations were derived by means of a transformation. First the angles between the branches of the bifurcation and the common carotid artery were, if necessary, adjusted by performing two simple rotations of the branches. Next the three-dimensional basic mesh was rotated and translated such that the centerline of the external carotid coincided with the x-axis. Subsequently, the coordinates of all nodes were multiplied with a factor $k(x)$ depending on the axial distance in the external carotid, resulting in the desired geometry of this branch. A similar procedure was used for the internal carotid. As the cross-section of the stenosed internal carotid always remains circular, the
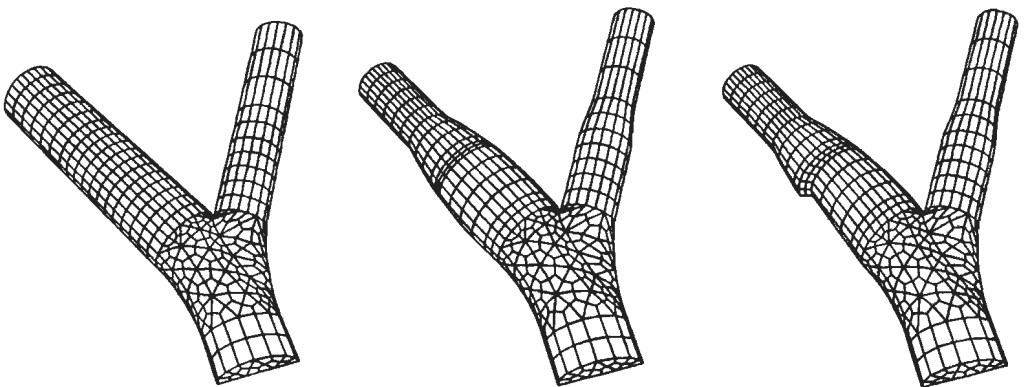
Figure 3.2: *The meshes for the numerical solutions of the fluid motion equations; the basic mesh (left), the non-stenosed bifurcation (center) and the 25% stenosed bifurcation (right).*

centerline of the desired carotid interna and the actual radius with respect to this centerline have been calculated and used for the transformation. In the internal carotid also mesh redistribution in axial direction has been applied. Small elements have been used (i) at the entrance of the internal carotid artery, since near the apex large velocity gradients are expected and (ii) in the region downstream the stenosis to minimize the deformation of the elements in the region downstream the stenosis. The resulting meshes for the non-stenosed and the 25% stenosed bifurcations are represented in the center and right-hand side plot of figure 3.2.

The boundary conditions

Boundary conditions have been prescribed in the plane of symmetry, at the wall of the bifurcation, at the outflow surfaces of the external and internal carotid arteries and at the entrance of the communis. The boundary conditions in the plane of symmetry are based on symmetry considerations:

$$\vec{u} \cdot \vec{n} = 0, \tag{3.17}$$
$$(\boldsymbol{\sigma} \cdot \vec{n}) \cdot \vec{t_1} = (\boldsymbol{\sigma} \cdot \vec{n}) \cdot \vec{t_2} = 0, \tag{3.18}$$

where $\vec{n}$ denotes the outer normal and $\vec{t_1}$ and $\vec{t_2}$ are two independent tangential directions. At the wall of the bifurcation the no-slip condition is applied (zero velocities).

At the outflow of the external and internal carotid arteries stress-free (i.e zero-stress vector) outflow boundary conditions are applied (since fully developed outflow conditions are too restrictive with respect to upstream influence of the flow field):

$$(\boldsymbol{\sigma} \cdot \vec{n}) \cdot \vec{n} = 0, \tag{3.19}$$
$$(\boldsymbol{\sigma} \cdot \vec{n}) \cdot \vec{t_1} = (\boldsymbol{\sigma} \cdot \vec{n}) \cdot \vec{t_2} = 0. \tag{3.20}$$

As a boundary condition at the entrance of the common carotid artery both tangential velocity components are set equal to zero, whereas the normal velocity component is described by an unsteady fully developed axial velocity field fitting to the applied flow pulse. The input flow pulse Q_c/Q_0, made dimensionless with the end-diastolic flow through the communis, is presented in figure 3.3. In this figure also the output flow pulses from the internal Q_i/Q_0 and external Q_e/Q_0 carotid arteries as determined from the computed outflow velocities, are given. The corresponding flow division ratio $\gamma = Q_e/Q_c$ is given at the right-hand side of figure 3.3. The inflow and outflow conditions are scaled using the dimensionless parameters Re, varying from 270 to 1000, the Womersley number $\alpha = 6$ and the flow division ratio $\gamma \approx 0.35$ (see also figure 3.3). In appendix A the derivation of the inflow velocities based on the theory of Womersley (1957), is given. At first the flow pulse is Fourier decomposed and 20 Fourier coefficients are determined. For each component the fully developed velocity profile for unsteady fluid flow $u_{axial}(r,t)$ in a rigid tube is calculated. Since for fully developed pipe flow the Navier-Stokes equations reduce to a linear form, summation of the velocity profiles for each Fourier component results in the velocity $u_{axial}(r,t)$. This is prescribed at the entrance of the common carotid artery.
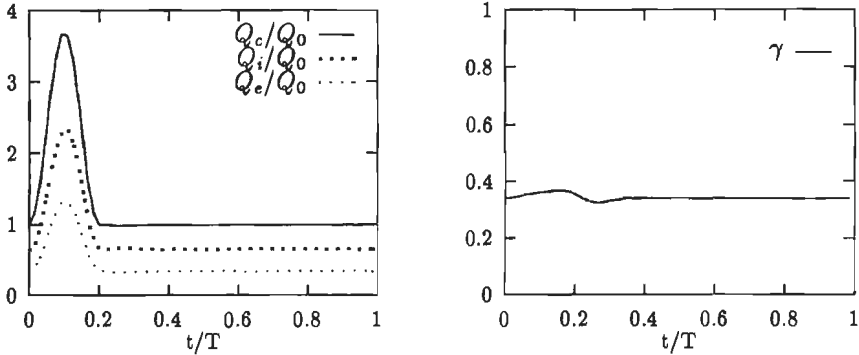
Figure 3.3: *Inflow Q_c/Q_0 for the finite element computations and outflow from the internal Q_i/Q_0 and external arteries Q_e/Q_0 (left) and the flow division ratio $\gamma = Q_e/Q_c$ in the computations of the non-stenosed bifurcation (right). The flow has been made dimensionless with the end-diastolic flow through the communis ($Q_0 = 0.4$).*

Computational specifications

As an initial condition for the unsteady computations the solution of the steady flow at end-diastole is used. This is justified, since a computation of the velocity field during 1.3 periods has shown that the differences between the velocity fields of the first and the second systole are less than 1%. Thus, at end-diastole a quasi-static flow is present and the steady flow solution can be used as an initial condition for the unsteady computations.

As will be discussed in section 3.4 the flow pulse has been divided into 256 time steps for the computation of the 0% and 25% stenosed bifurcations. The computations have been performed on a Cray-ymp computer, using 280 MByte internal memory and 210 seconds CPU-time per time step (i.e. approximately 15 hours CPU-time).

3.3   Results of the velocity field

In this section the computational results of the 0% and the 25% stenosed carotid artery bifurcation are presented. The plots have been produced with the visualization package Data Visualizer (Wavefront). This package has also been used to produce a video tape of the three-dimensional time-dependent flow field, using the solutions of all 256 time steps. Though the computations have been performed on one half of the bifurcation (see also figure 3.2), the results for the complete bifurcation are presented here. For this purpose the results have been reflected about the plane of symmetry. The 3D time-dependent flow fields for the non-stenosed and the 25% stenosed bifurcations are presented in figures 3.5 and 3.6 respectively. In the figures each column contains information about the velocity field at a certain time step. The results are given at time steps $t/T = 0$ (end-diastole), $t/T = 0.1$ (peak-systole), $t/T = 0.2$ (end-systole), $t/T = 0.25$, $t/T = 0.3$ and $t/T = 0.4$.

The actual time is indicated in the plot of the flow pulse. The upper plots represent the velocity vectors in the plane of symmetry. The other plots represent the axial and secondary velocity fields along cross-sections at sites I_{00}, I_{05}, I_{10}, I_{15} and I_{20}, which are marked in figure 3.4. The secondary velocities are represented by vector plots. The axial velocities are shown in 3D plots, where the elevation and the brightness of the figures are proportional to the axial velocity. In figure 3.4 (right) the grey scale of the axial velocities is given. The cross-sections are viewed in perspective, which is also illustrated in figure 3.4.
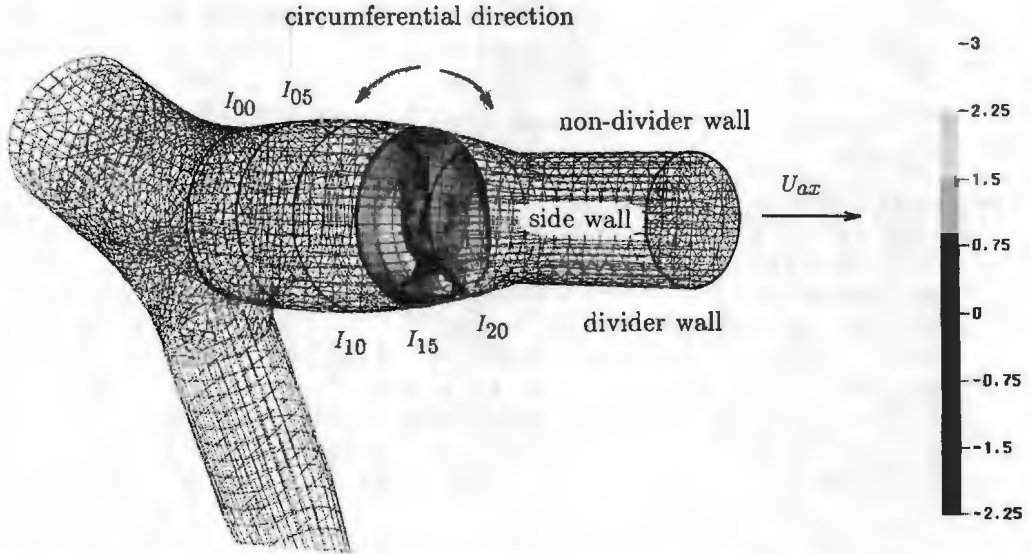
Figure 3.4: *Illustration of the perspective of the axial and secondary velocity plots at sites I_{00}, I_{05}, I_{10}, I_{15} and I_{20} (left), and the grey scale of the axial velocities (right).*

0% stenosed geometry

Here the computational results of the non-stenosed bifurcation from figure 3.5 will be summarized. For each time step a short description of the phenomena will be given. For the interpretation of the figure it should be noted that the time steps during diastole are such that approximately in one step convection of the velocities to the next cross-section occurs. Therefore, the reader is encouraged to read the diagrams diagonally.

$t/T = 0$ **(end-diastole)** At this time step positive axial velocities occur at all sites, except for an area with very small negative velocities near the non-divider wall at sites I_{00} and I_{05}. Near the divider wall the velocities and the shear rates are relatively high. The secondary flow field is not significant at this time step. At site I_{00} a

secondary velocity component towards the divider wall is present, due to the inertia of the fluid entering the internal carotid artery and thus having a component in secondary direction. This phenomenon can more or less be seen at all time steps and will not be mentioned anymore.

$t/T = 0.1$ **(peak-systole)** At peak-systole high axial velocities occur over the whole cross-section. The velocities near the divider wall are slightly higher than the velocities near the non-divider wall. The flattening of the axial profiles at sites I_{15} and I_{20} is caused by the decreasing arterial lumen at these sites.
The secondary velocities are still not very significant at peak-systole. Small secondary velocities, directed from the divider wall via the side walls towards the non-divider wall form a secondary vortex at each site. At cross-section I_{20} the secondary velocities are directed towards the center of the channel, due to the convergence of the geometry.

$t/T = 0.2$ **(end-systole)** Half-way systolic deceleration ($t/T = 0.15$, these figures are not included in figure 3.5) small regions with negative velocities appear near the non-divider wall. These negative velocity regions grow and the situation at end-systolic deceleration ($t/T = 0.2$) is given in figure 3.5. The area with negative velocities has its largest radial extent in the plane of symmetry. The axial velocities are maximal near the divider wall. Going from the divider wall towards the non-divider wall in the plane of symmetry, very large gradients in the axial velocities occur. This region of large radial gradients in the plane of symmetry is referred to as the shear layer. Outside the plane of symmetry the gradient of the axial velocities is smaller. At sites I_{05}, I_{10} and I_{15} the extension of the area with negative velocities in circumferential direction can be seen both at the center and near the non-divider side wall. As a result, at site I_{15} small negative velocities are present in a small zone near the side walls.
The figures of the secondary velocities show a strong secondary flow field near site I_{05} at $t/T = 0.2$. From the secondary and axial velocity distributions at side I_{05} it can clearly be seen that the axial velocity is convected by the secondary field from the divider side, along the side walls into the center of the interna. It also shows that during systolic deceleration helical flow patterns are present in the area with low shear. The helical patterns move both downstream and upstream, dependent on the local and momentary axial velocity field $u_{ax}(\vec{x}, t)$.

$t/T = 0.25$ In the plane of symmetry the axial velocities in the reversed flow region have become less negative. Moreover, the extent of the area with negative velocities outside the plane of symmetry has decreased. This is a result of the secondary velocity field, that transports fluid elements with high axial velocities towards the plane of symmetry. At site I_{10} high axial velocities occur in a narrow ring near the divider and side walls, whereas at the non-divider wall and in the center of the vessel negative velocities occur. At site I_{20} a very remarkable axial and secondary velocity field is present as a result of a combination of the present flow field and the tapering

of the lumen.

The secondary flow is strongly represented at sites I_{05} and I_{10}, indicating a helical fluid flow pattern. At site I_{05} the cores of the secondary vortex are located near the non-divider wall of the vessel, whereas at site I_{10} the cores have moved towards the divider wall. It should be noted that near the non-divider wall a second pair of vortices develops at this time.

$t/T = 0.3$ **and** $t/T = 0.4$ The area with negative axial velocities further decreases during diastole. The small regions with negative velocities near the side walls have fully disappeared at $t/T = 0.3$. The narrow ring of high axial velocities that was present at site I_{10} at $t/T = 0.25$, seems to have moved to site I_{15} at $t/T = 0.3$, though the phenomenon is less pronounced. At $t/T = 0.4$ it has fully disappeared. After $t/T = 0.4$ a smooth transition to the end-diastolic situation $(t/T = 0)$ occurs.

The axial position of the strongest secondary vorticity shifts to more downstream sites as diastole proceeds. Moreover, the secondary velocity field and thus also the helical flow pattern, gets less and less significant, fading away to the end-diastolic situation (at $t/T = 0$).

Figure 3.5: **(Next pages)** *Computational results of the 3D time-dependent flow field for the non-stenosed bifurcation. Each column contains information about the velocity field at time steps $t/T = 0$ (end-diastole), $t/T = 0.1$ (peak-systole), $t/T = 0.2$ (end-systole), $t/T = 0.25$, $t/T = 0.3$ and $t/T = 0.4$. The upper plots represent the velocity vectors in the plane of symmetry, whereas the other plots represent the axial and secondary velocity fields along cross-sections at sites I_{00}, I_{05}, I_{10}, I_{15} and I_{20}. The axial velocities are shown in 3D plots, where the elevation and the brightness of the figures are proportional to the axial velocity. Note that in this figure the secondary velocity vectors are scaled three times larger than the vectors of the axial velocity field.*

I_{10}

I_{15}

I_{20}
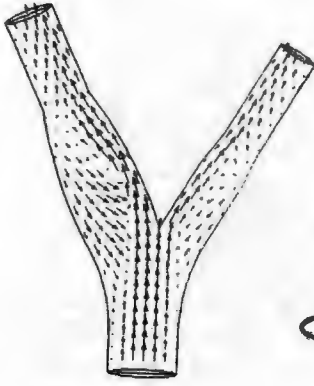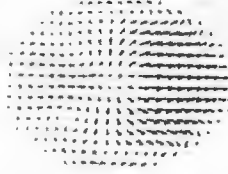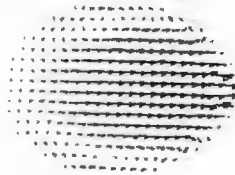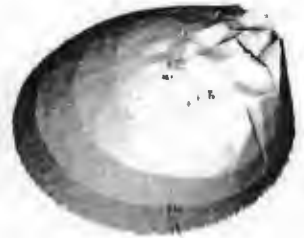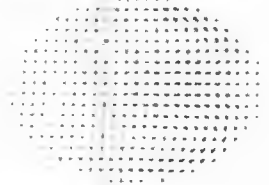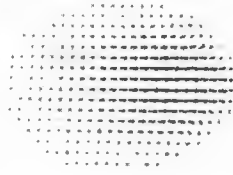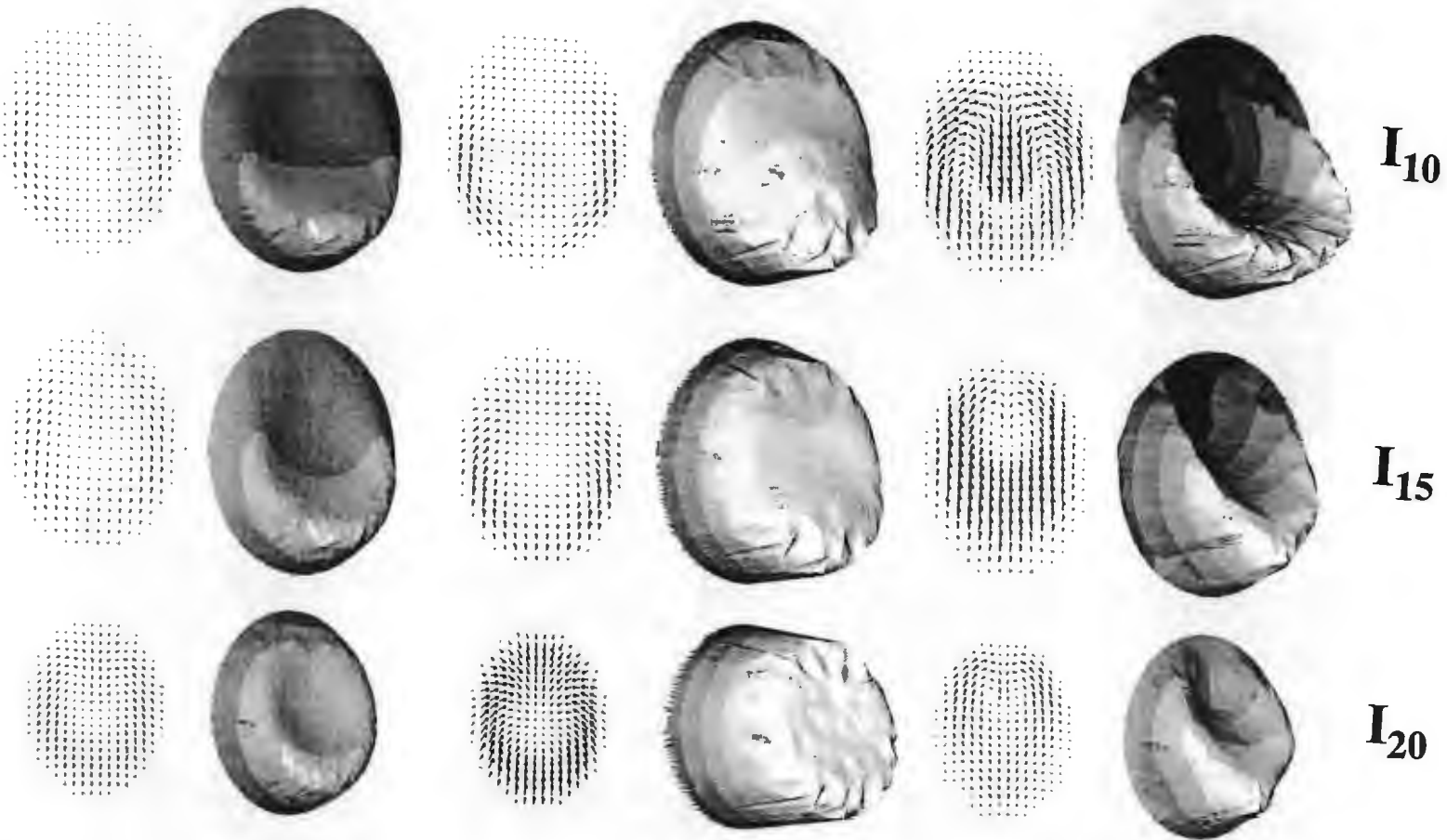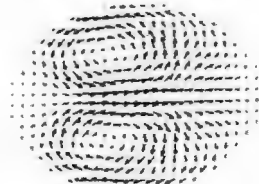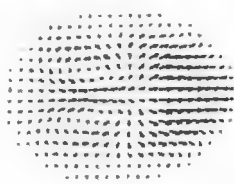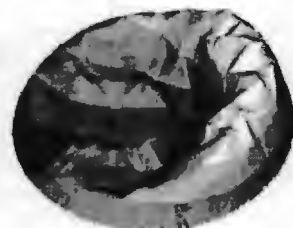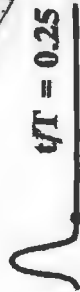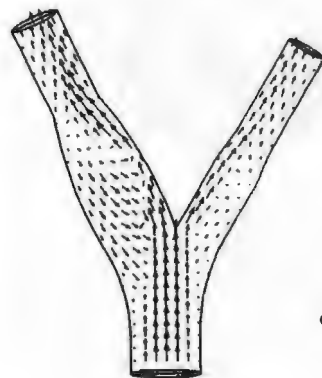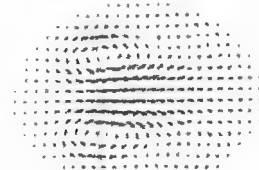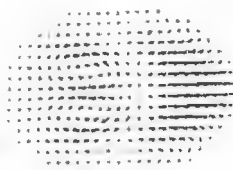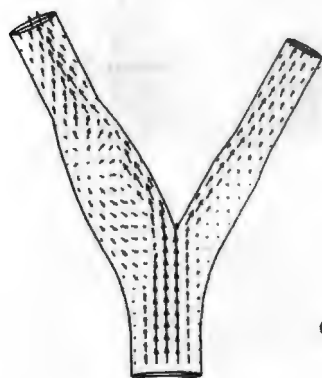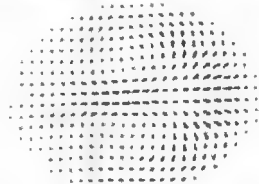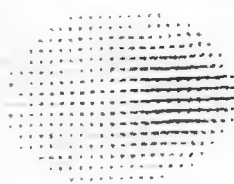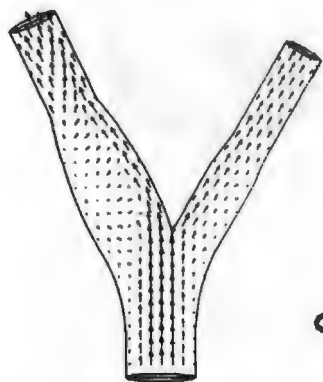
I_{10}

I_{15}

I_{20}
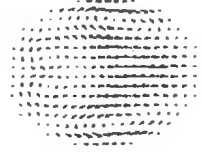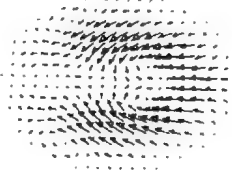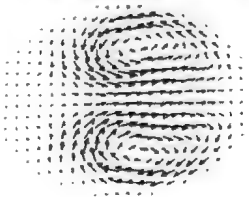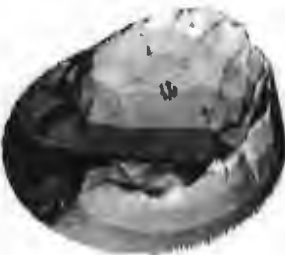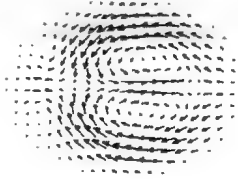
25% stenosed geometry

The computational results of the 25% stenosed geometry are presented in figure 3.6. The differences with the results of the non-stenosed bifurcation can be summarized as follows.

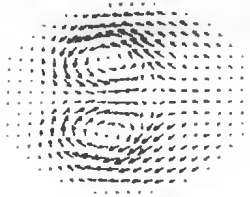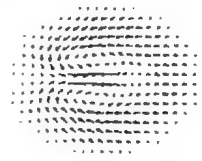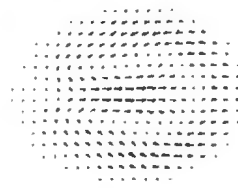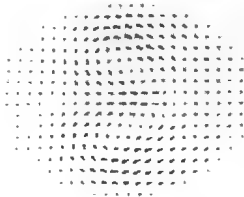$t/T = o$ **(end-diastole)** The small negative velocities, that were present in the non-stenosed bifurcation at sites I_{00} and I_{05}, can not be seen in the stenosed case.

$t/T = o.1$ **(peak-systole)** Compared to the non-stenosed case the situation of the 25% stenosed case at peak-systole is marked by: (i) slightly larger secondary velocities near the walls at sites I_{10} and I_{15}, (ii) a flattening of the profile at I_{10}, due to the decreasing arterial lumen and (iii) smaller gradient of the axial velocity downstream the stenosis (I_{15}), especially near the non-divider wall. As a result the main stream has slightly shifted towards the divider wall.

$t/T = o.2$ **(end-systole)** At end-systole the following flow features can be seen in the stenosed case compared to the non-stenosed situation. (i) The radial extension of the region with negative axial velocities in the plane of symmetry has decreased at sites I_{05} and I_{10}. (ii) The axial velocities at site I_{15} show a small influence of the stenosis, that is expressed in an enlarged negative velocity zone near the non-divider and side walls. The negative velocities in this region near the non-divider wall however, are smaller. At site I_{20} still small negative velocities are present. (iii) The secondary velocities near the non-divider wall are slightly enlarged.

$t/T = o.25$ Compared to the non-stenosed situation the features of the stenosed bifurcation are as follows. (i) At site I_{05} a stronger secondary vortex is present. (ii) The region with negative axial velocities is larger in circumferential direction at sites I_{10} and I_{15}, though the values near the plane of symmetry are less negative. (iii) The core of the secondary vortex at position I_{10} has shifted towards the divider wall. (iv) Downstream the stenosis (I_{15} and I_{20}) the main flow has shifted towards the divider wall, due to the presence of the stenosis.

$t/T = o.3$ It can be seen that in the 25% stenosed case (i) the axial velocity field at sites I_{10} and I_{15} is smoother, (ii) the secondary flow field is stronger at site I_{10} and (iii) the main axial flow has shifted towards the divider wall downstream the stenosis.

$t/T = o.4$ At $t/T = 0.4$ the differences between the non-stenosed and the 25% stenosed cases are not very evident anymore.

3.4   Concluding discussion

In the previous section the computational results of the non-stenosed and the 25% stenosed carotid artery bifurcation have been presented. It has been shown that a very complex 3D, time-dependent flow field is present in the bifurcation, where both the axial and secondary

flow fields play an important role. The results for the non-stenosed bifurcation can be compared with findings from Ku *et al.* (1985a), Perktold and Resch (1990) and Rindt and Van Steenhoven (1994), who also considered unsteady flow in 3D rigid non-stenosed carotid artery bifurcations (see also section 1.2). Ku *et al.* (1985a) performed LDA experiments, whereas Perktold and Resch (1990) studied the velocity field numerically. Rindt and Van Steenhoven (1994) performed both finite element computations and LDA experiments. Though the inflow conditions of studies mentioned above, differ from those in the present study (see also section 1.2), a striking similarity can be found between the global flow phenomena in those studies and the non-stenosed case in the present study, showing all the following features. (*i*) During systolic acceleration the region with reversed axial flow is 'washed away' (i.e. no negative axial velocities are found near the non-divider wall). (*ii*) A region with reversed axial flow develops during systolic deceleration, reaching its largest dimensions at the onset of diastole. (*iii*) During the second half of systolic deceleration and in the initial phase of diastole a significant secondary flow field is present in the bifurcation. As a result the region with high axial velocities extends in circumferential direction (Rindt and Van Steenhoven (1994) refer to this phenomenon as 'C-shaped axial velocity contours'). The similarity of this phenomenon with unsteady flow in a curved tube was shown by Rindt (1989).

From the results in section 3.3 it has become clear that the most significant and interesting flow phenomena can be found in the period starting from systolic deceleration up until $t/T = 0.4$. After that, a smooth transition to the end-diastolic situation occurs, pointing at the quasi-static behavior at that time. This is in qualitative agreement with the findings from chapter 2. Here the hydrogen-bubble experiments showed also an unsteady shear layer behavior during systolic deceleration and in the initial phase of diastole, and a quasi-static situation at end-diastole.

The influence of the 25% stenosis mainly involves three aspects. (*i*) A decrease of the reversed velocity area at sites I_{05} and I_{10} in the stenosed case in the initial phase of diastole. (*ii*) An increase of the reversed velocity area downstream the stenosis (I_{15}, I_{20}) with velocities that are less negative. This coincides with the shift of the main flow towards the divider wall downstream the stenosis. (*iii*) An increase of the near wall secondary velocities in the stenosed case. Though the influence of the 25% stenosis appears to be small, the information about both the velocities in the plane of symmetry and the secondary vortices outside the plane of symmetry seem to be important to describe the influence of the stenosis. Therefore in the next chapter LDA experiments will not only be performed in the plane of symmetry (like in the hydrogen-bubble experiments), but also along lines perpendicular to this plane. In this way also information on the helical patterns is gained.

Figure 3.6: (**Next pages**) *Computational results of the 3D time-dependent flow field for the 25% stenosed bifurcation.*
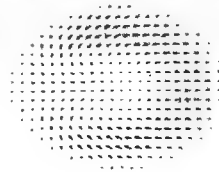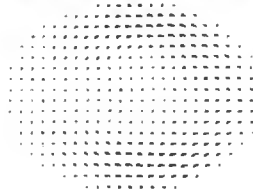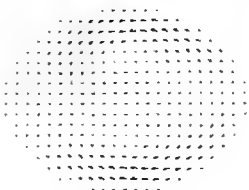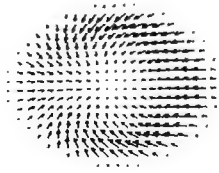
$t/T = 0.0$ $t/T = 0.1$ $t/T = 0.2$

I_{00}

I_{05}

I_{10}

I_{15}

I_{20}

t/T = 0.25   t/T = 0.3   t/T = 0.4
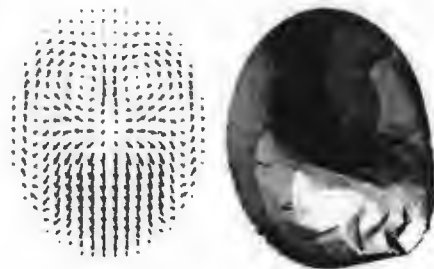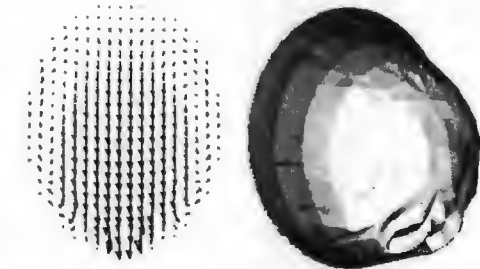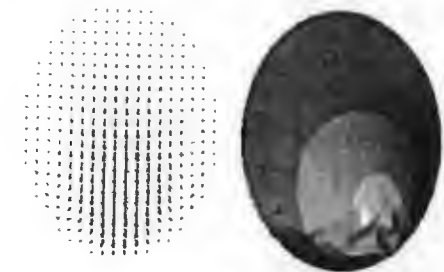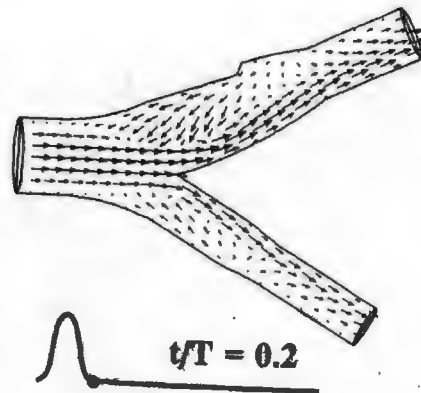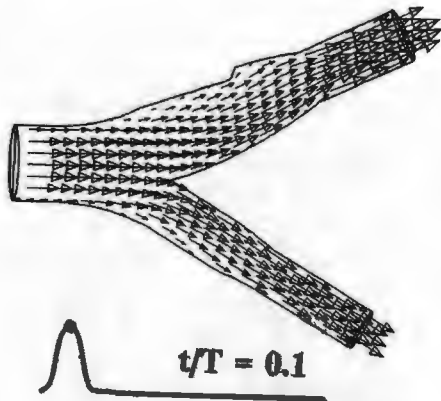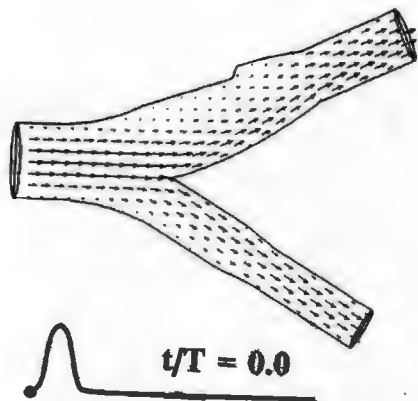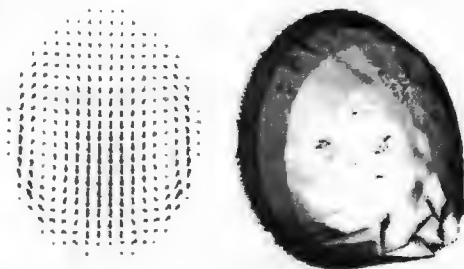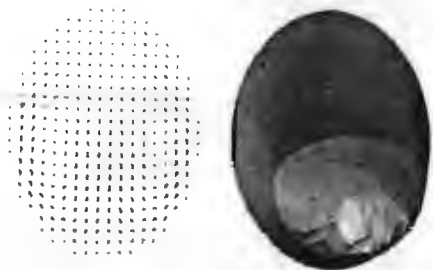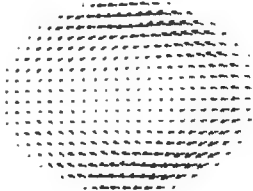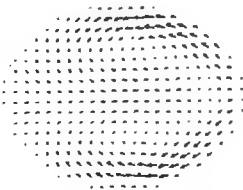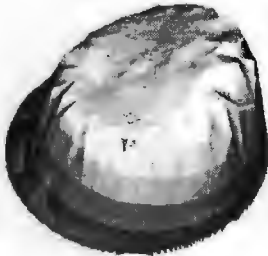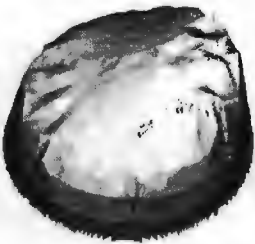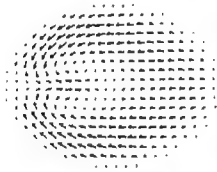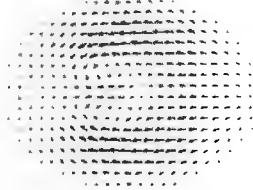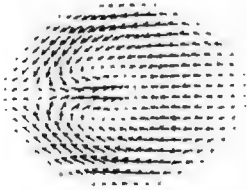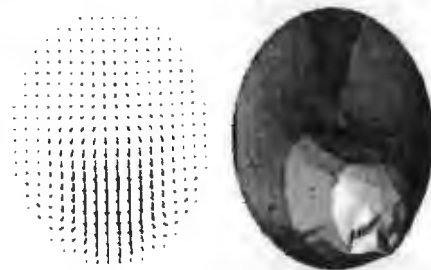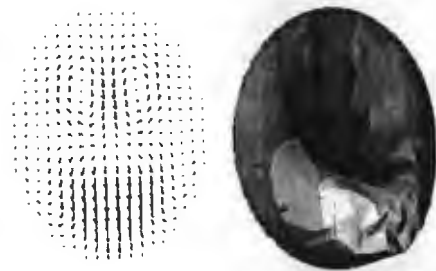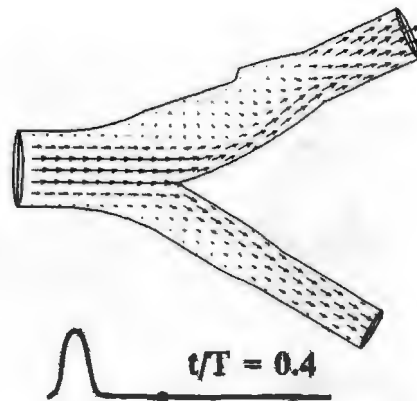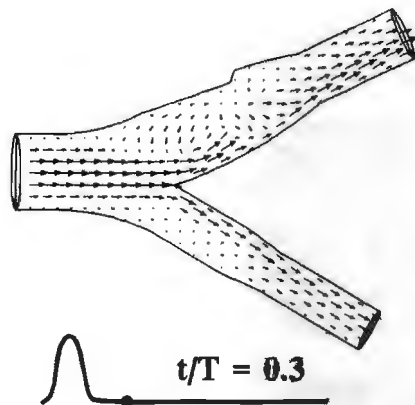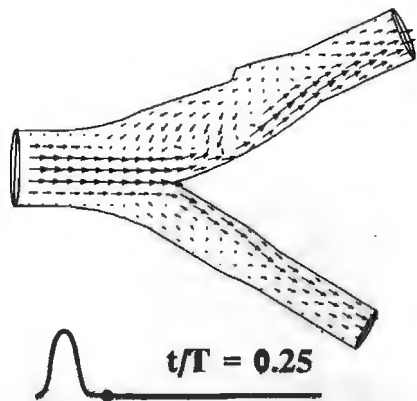
I_{00}
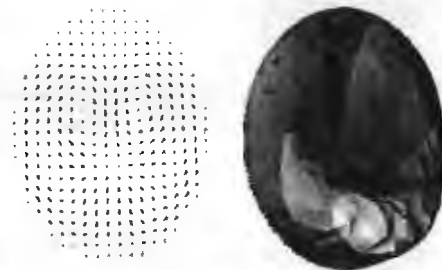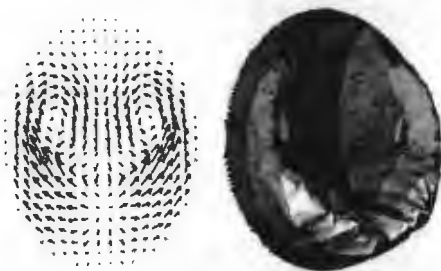
I_{05}
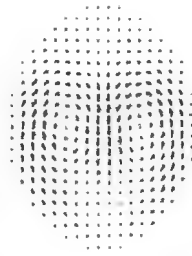
I_{10}
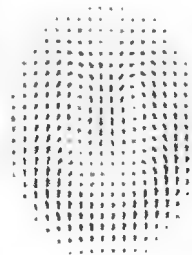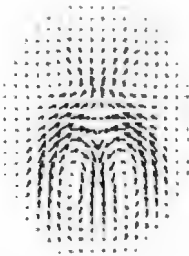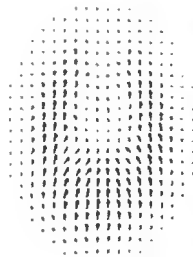
I_{15}
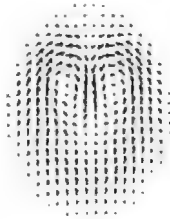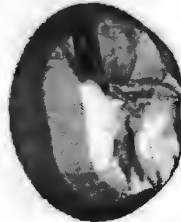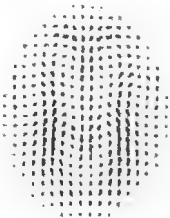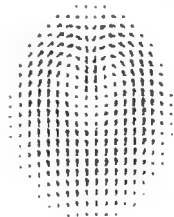
I_{20}

For the detectability of minor stenoses the shift of the main flow downstream the stenosis (see point (*ii*)), is an interesting feature which will be analyzed in more detail in chapter 7, where the skewness of velocity profiles is considered. It should also be noted that in the present chapter the global flow features are studied by only considering the flow field at discrete time steps. For diagnostic applications however, the velocity as a function of time may also contain important information. Therefore, in chapter 5 the computational unsteady flow phenomena will also be evaluated as a function of time.

As can be seen in the axial velocity plots from figures 3.5 and 3.6 the results of the axial velocity field are not very smooth, which can be attributed to computational inaccuracies and interpolation errors. The computational inaccuracies may be caused by several factors as mentioned below.

Spatial discretization. Computations with a finer mesh are expected to give more accurate and smooth results. However, mesh refinement would also require much higher amounts of computer memory, which can not be performed practically at this moment. The use of a high-order spectral element method (Timmermans, 1994), showing superior properties with respect to computational accuracy and efficiency, may provide a method that does not have the limitations mentioned above.

Time discretization. Time discretization also influences the computational accuracy. Especially in the phases of the flow pulse, where large velocity gradients in time occur, time discretization errors may influence the solution. From a comparison of computational results with 128 and 256 time steps, it seems that 256 time steps are a good choice with respect to numerical accuracy on the one hand and computing time on the other hand (see also section 5.4).

Element deformation. Due to the transformation performed in order to obtain a mesh for the final geometries, the elements are deformed. This deformation is small in almost the entire mesh, thanks to the local mesh refinement downstream the stenosis. Nevertheless, these deformations can be locally such that the final accuracy is decreased.

More detailed information on the computational accuracy will be given in chapter 5, where the computational results are compared with experimental data from LDA measurements in in-vitro models of the bifurcation.

Chapter 4

LDA-experiments

4.1 Introduction

In the previous chapter the numerical results of the axial and secondary velocity fields in a non-stenosed and a 25% stenosed carotid artery bifurcation have been described extensively. Since it is a priori not evident whether the computational method and the computational accuracy are sufficient to resolve all physical phenomena in detail, quantitative and accurate experiments are indispensable. Therefore, laser Doppler anemometry (LDA) experiments have been performed to gain accurate and time-dependent measurements of the axial and secondary flow fields. The experimental data are used to validate the computational results, as will be done in the next chapter.

In this chapter the LDA measurements in both the non-stenosed and the 25% stenosed model of the carotid artery bifurcation are described. In section 4.2 a description of the experimental methods is given. Next the LDA results are presented (section 4.3) and the chapter will be completed with a discussion (section 4.4).

4.2 Experimental methods

Fluid circuit

A schematic presentation of the fluid circuit is given in figure 4.1. The reservoir, containing the measuring fluid, is immersed in a water filled container of constant temperature of 36 °C. A gear pump is used for the generation of the steady flow component (micropump, Verder). The unsteady flow component is generated by a computer controlled plunger pump (superpump, VSI). Before entering the model the fluid passes a buffer and an inlet tube of length $150D$, where D represents the diameter of the common carotid artery. This guarantees stable and fully developed flow as the fluid enters the measuring section. Return tubes with taps and flow sensors (Transflow 601, Skalar-instruments) transport the fluid back to the reservoir.

The models are 2.5:1 enlarged models of the physiological case ($D = 20\,mm$) and they
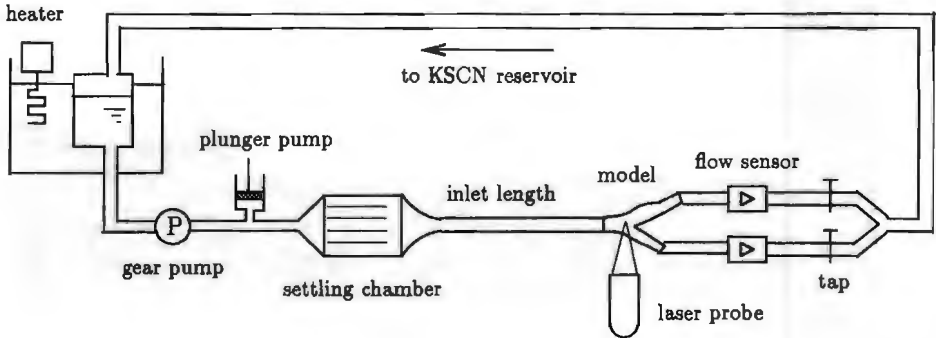
Figure 4.1: *Schematic presentation of the fluid circuit, used for the LDA experiments.*

have been machined out of PMMA (see also section 2.2), having an index of refraction equal to 1.491 ± 0.001. A concentrated solution of potassium thiocyanate (KSCN) in water is used as a measuring fluid to obtain an identical index of refraction of the fluid. The dependency of the index of refraction on the concentration of KSCN has been determined at a temperature of 36 °C and is presented in figure 4.2 (left). For the experiments a concentrated solution of 71 weight percent KSCN in water is used, having an index of refraction equal to 1.490 ± 0.005. The dynamic viscosity of the KSCN solution has been determined by means of a Couette viscosimeter (Rheometrics - RFS II). The results of the dynamic viscosity for various shear rates at a temperature of 36 °C are presented in figure 4.2 (right). The KSCN solution exhibits Newtonian fluid behavior with a dynamic
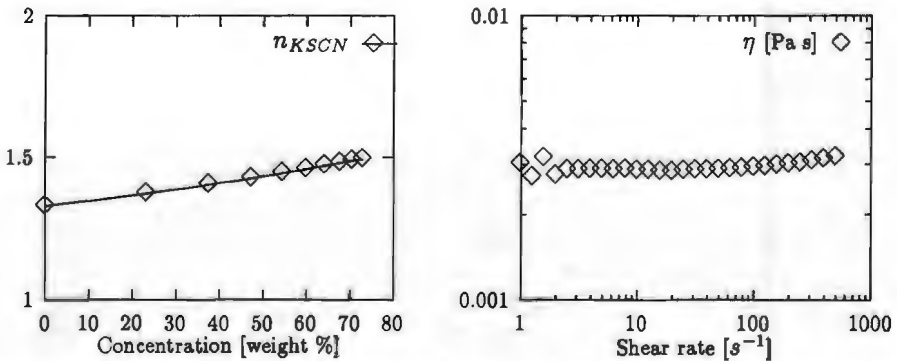
Figure 4.2: *Index of refraction of the KSCN solution as a function of the concentration at 36 °C (left) and the dynamic viscosity as a function of the shear rate for a 71 weight percent KSCN solution (right).*
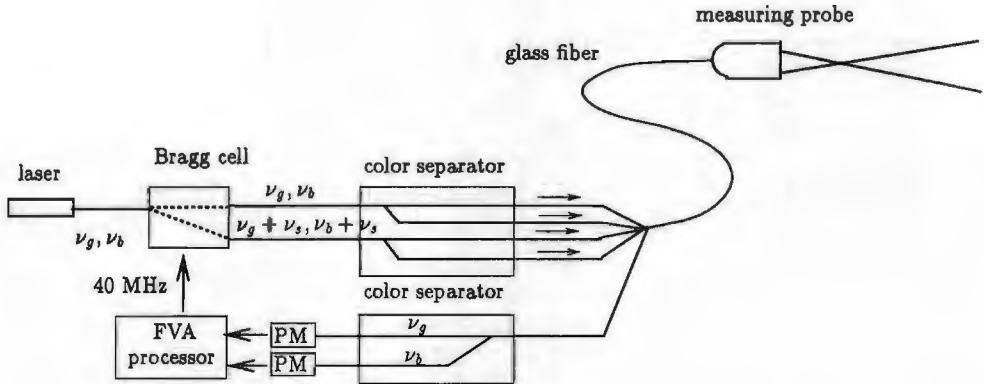
Figure 4.3: *Schematic draw of the LDA equipment; PM represents the photomultiplier and ν_g, ν_b and ν_s denote respectively the frequencies of the green and blue colors and the frequency shift, added by the Bragg cell.*

viscosity η determined at $(2.9 \pm 0.1) \cdot 10^{-3} kgm^{-1}s^{-1}$ for shear rates up to $100\,s^{-1}$. With the density of the KSCN solution $\rho = (1.410 \pm 0.005) \cdot 10^3 kgm^{-3}$ $(36°C)$, it follows that the kinematic viscosity amounts $\nu = \eta/\rho = (2.0 \pm 0.1) \cdot 10^{-6} m^2 s^{-1}$.

Laser Doppler equipment

A schematic drawing of the LDA equipment is given in figure 4.3. The equipment is based on the differential Doppler technique. The basic principle of this technique is described in appendix B. In the present section, only specifications of the LDA equipment are given. A laser beam is generated by a 300 mW Argon-ion laser (Ion Laser Technology 5500A). The laser beam is linearly polarized and contains three colors: green ($\lambda = 514.5\,nm$), blue ($\lambda = 488.0\,nm$) and violet ($\lambda = 476.5\,nm$). A two-dimensional configuration with only blue and green colors is used. After the laser beams have passed a Bragg cell, controlled by a Flow Velocity Analyzer (Dantec 58N20), two beams of equal intensity have been formed. The frequency of one of the beams has been shifted with a shift frequency of $\nu_s = 40\,MHz$. Next a color separator splits the beam into four laser beams, which are focused into four separate glass fibers. Together with one fiber for the received scattered light, these fibers are bundled together and lead to the measuring probe. Here, the four laser beams are emitted and a lens with focal length $f = 80\,mm$ focuses the four laser beams to form one measuring volume. The scattered light from particles in the measuring volume is received by the same measuring probe (backward scatter mode). Next, the scattered light is focused by the same focal lens and transported back through a fiber. A second color separator differentiates between the green and the blue light and both signals are detected by two photomultipliers. Here the optical signals are transformed into electrical signals, that are processed by the Flow Velocity Analyzer.

The spatial resolution of the LDA experiments is determined by the dimensions of the measuring volume. It can be shown that the measurement volume has an ellipsoidal shape and that the dimensions are determined by the angle θ between the two laser beams and the diameter of the laser beam in the measuring volume, provided that the waist of the beam is positioned in the measuring volume (Drain, 1980). In our case this leads to a measuring volume with dimensions $50 \times 50 \times 200\,\mu m$.

The temporal resolution of the LDA measurements is determined by the time interval between the scattering particles in the measuring volume. To guarantee a sufficient large effective data rate (i.e. the number of validated samples per second), scattering particles are added to the measuring fluid (referred to as seeding). The quality of the signal from the scattered particles is strongly influenced by the properties of the particles. Firstly, the density of the particles should approximate the density of the measuring fluid to prevent sedimentation or rising of the particles. Secondly, the particles need to have good reflecting properties to favor back scattering. Moreover, the diameter of the scattering particles needs to be in the order of magnitude of $\mathcal{O}(10\,\mu m)$, such that the reflecting area is large enough to detect the scattered light Goldstein (1983). However, if the diameter of the particles is much larger than the fringe spacing in the measuring volume, a diminished signal-to-noise ratio is resulting. To satisfy the conditions mentioned above, Rutile crystals with sizes smaller than 15 μm (Iriodine 111, Merck) are added to the measuring fluid. The optimal seeding concentration is determined under steady flow conditions and amounts about 20 gm^{-3}. The maximum frequency that can be followed by the particles due to inertia forces, can be determined using equation 2.2, that was also used for the H_2-bubbles in the visualization study. With the fluid properties as mentioned before and the density of the particles approximately equal to the density of the fluid, it can be shown that the particles can follow oscillations of the fluid up to $2kHz$.

Experimental procedure

The experiments have been performed for a simplified flow pulse with a shape according to the reference situation as defined in chapter 1 ($T_a/T = T_d/T = 0.1$, $T_p/T = 0$) and $Re = 270 - 1000$, $\alpha = 6$. The mean flow ratio between the flow in the external carotid artery and the common carotid artery during the flow pulse is $\gamma = 0.35$. In figure 4.4 the measured flows through the common (Q_c/Q_0), internal (Q_i/Q_0) and the external arteries (Q_e/Q_0) are given (left). The flows have been made dimensionless by the end-diastolic common carotid flow $Q_0 = 0.5\,l/min$. In the right plot of figure 4.4 the flow ratio as a function of time is presented.

Velocities have been measured along lines in the plane of symmetry and along lines in a plane perpendicular to this plane, which is schematically drawn in figure 4.5. The measurements in the communis (C) are taken along a line at a distance of $1.5D$ upstream the apex. In the interna, velocity measurements are taken at 5 different sites. Starting at the apex (I_{00}), new sites are defined every $0.5D$ moving along the axis of the interna (I_{05}, I_{10}, I_{15} and I_{20}), as drawn in figure 4.5. Two velocity components are measured simultaneously: the velocity component parallel to the axis of the vessel (axial velocity) and
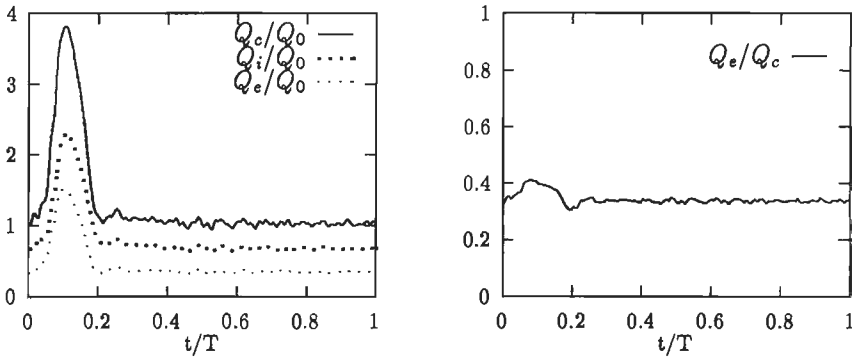
Figure 4.4: *Measured flows through the common (Q_c/Q_0), internal (Q_i/Q_0) and external (Q_e/Q_0) carotid arteries, made dimensionless with the end-diastolic common carotid flow $Q_0 = 0.5\,l/min$ (left), and the flow ratio between the external and the common carotid artery (right).*

the component perpendicular to this axis and parallel to the plane of symmetry (one of the secondary velocity components). During 16 cycles of $T = 6\,s$, velocities have been measured at each site with an effective data rate varying from about $30\,Hz$ at low velocity sites to $300\,Hz$ at high velocity sites. To gain a sample record which is equidistant in time, each cycle is divided into 64 intervals and the velocities in these intervals have been averaged. During the measurement of nearly zero velocities, occasionally no valid velocity measurements are present in a time interval. In such case an interpolation of the velocities between the previous and the next interval is made. Finally, the 8 cycles with the largest averaged data rate have been selected to compute the ensemble averaged velocity signal.
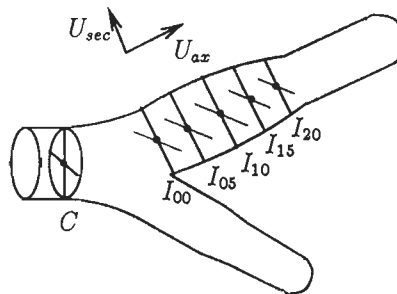
Figure 4.5: *Overview of the measuring sites along lines in the plane of symmetry, and along lines perpendicular to this plane.*

4.3   Results

Description of the flow field along lines in the plane of symmetry

The ensemble averaged signals are presented in three-dimensional plots (see also figure 4.6, where the ensemble averaged axial velocities at site C are given for the non-stenosed bifurcation). The axis 'time', 'velocity' and 'position' are made dimensionless using the period of the flow pulse $T = 6\,s$, the mean velocity in the communis at end-diastole $U_d = 29\,mms^{-1}$ and the local radius of the vessel $R = 10^{-2}m$. In the interna, '$r/R = -1$' defines the non-divider wall and '$r/R = +1$' is the divider wall. In the figures, the velocity values at the walls are set to $0\,ms^{-1}$ manually to eliminate the noisy signals when the measuring volume is positioned partially in the wall.
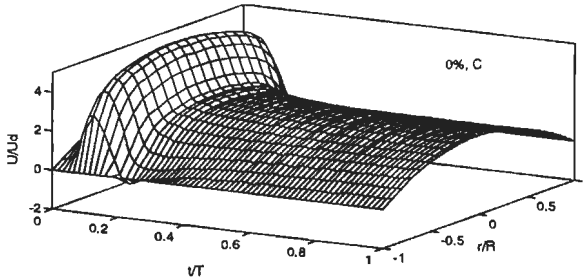
Figure 4.6: *Measured ensemble averaged axial velocities in the plane of symmetry at site C for the non-stenosed bifurcation.*

A description of the axial velocities in the plane of symmetry at the different sites is given below (see also figure 4.7).

site C : (figure 4.6) The velocity profiles in the communis are nearly parabolic during diastole, whereas the profiles are somewhat flattened during systole. Generally, the velocity signals follow the shape of the flow pulse in the communis. At near wall sites, small negative velocities can be seen at the onset of diastole. The inflow conditions in the normal and stenosed model are identical.

site I_{00} : (figure 4.7) During systole the velocity profiles show a slight asymmetry with higher velocities near the divider wall. During systolic deceleration a large velocity gradient in time near the non-divider wall marks the onset of a region with flow reversal. At near wall sites this region persists throughout diastole, gradually decreasing in radial extent as t/T increases. At $t/T = 0.3$ a large axial velocity gradient in radial direction can be seen, forming a transient shear layer. This is followed by a small oscillation at $t/T = 0.4$. After $t/T = 0.4$ a smooth transition takes place to the end-diastolic flow field with significant axial velocities near the divider wall and nearly zero velocities near the non-divider wall.

The influence of the stenosis involves two aspects. (i) A slight disturbance of the velocity field can be seen in the region with flow reversal, starting at $t/T = 0.3$. As compared to the normal model the velocities are slightly larger. (ii) Near the shear layer of the stenosed configuration a more pronounced oscillation of the axial flow field can be discerned.

site I_{05} : The asymmetry of the velocity profiles during systole is more pronounced at this site. Again a large velocity gradient in time is seen during systolic deceleration, followed by a region with negative and nearly zero velocities. This region appears to be larger than at site I_{00} for all times, though the velocities seem to be less negative. Near the divider wall a new feature appears in both the non-stenosed and the stenosed case as a second peak develops in the initial phase of diastole. The oscillation in the shear layer becomes more pronounced at this site for both the non-stenosed and the stenosed geometry.

The influence of the stenosis (i.e. the presence of enlarged velocities in the low velocity area and the oscillations in the shear layer) appears to be more pronounced than at site I_{00}.

site I_{10}: At site I_{10} the second peak near the divider wall has shifted slightly to a later phase of the flow pulse ($t/T = 0.3$). The region with flow reversal has become smaller, especially in the stenosed case. The disturbance in the low velocity region has grown and seems to have moved towards the divider wall. As a result remarkable differences can be seen in the disturbances in the shear layer for the non-stenosed and the 25% stenosed bifurcations. In the non-stenosed case the onset of small oscillations in the shear layer is visible, which seem to have a lower frequency and a larger amplitude in the 25% stenosed case.

site I_{15}: The main flow features as described for the previous site can also be found at this site. Some small changes are found in the diminished radial extent of the region with flow reversal at early diastole and the shift of the second peak near the divider wall to a later phase in diastole. For the stenosed bifurcation the disturbance in the area with low velocities is even more pronounced than it was at site I_{10}. This disturbance has moved further towards the divider wall and seems to interfere with the axial velocities in the shear layer. The differences between the non-stenosed and the 25% stenosed axial velocities are also very obvious at this site.

It should be noted that, apart from slightly diminished velocities downstream the stenosis during systole, no unsteady vortex shedding from the stenosis can be seen.

site I_{20} : At site I_{20} most of the features mentioned above have diminished, caused by the decreasing arterial lumen at this site. The asymmetry of the profiles during systole has become less pronounced, the regions with flow reversal have fully disappeared, no distinct shear layer is visible anymore and the oscillations of the shear layer have significantly diminished in amplitude.
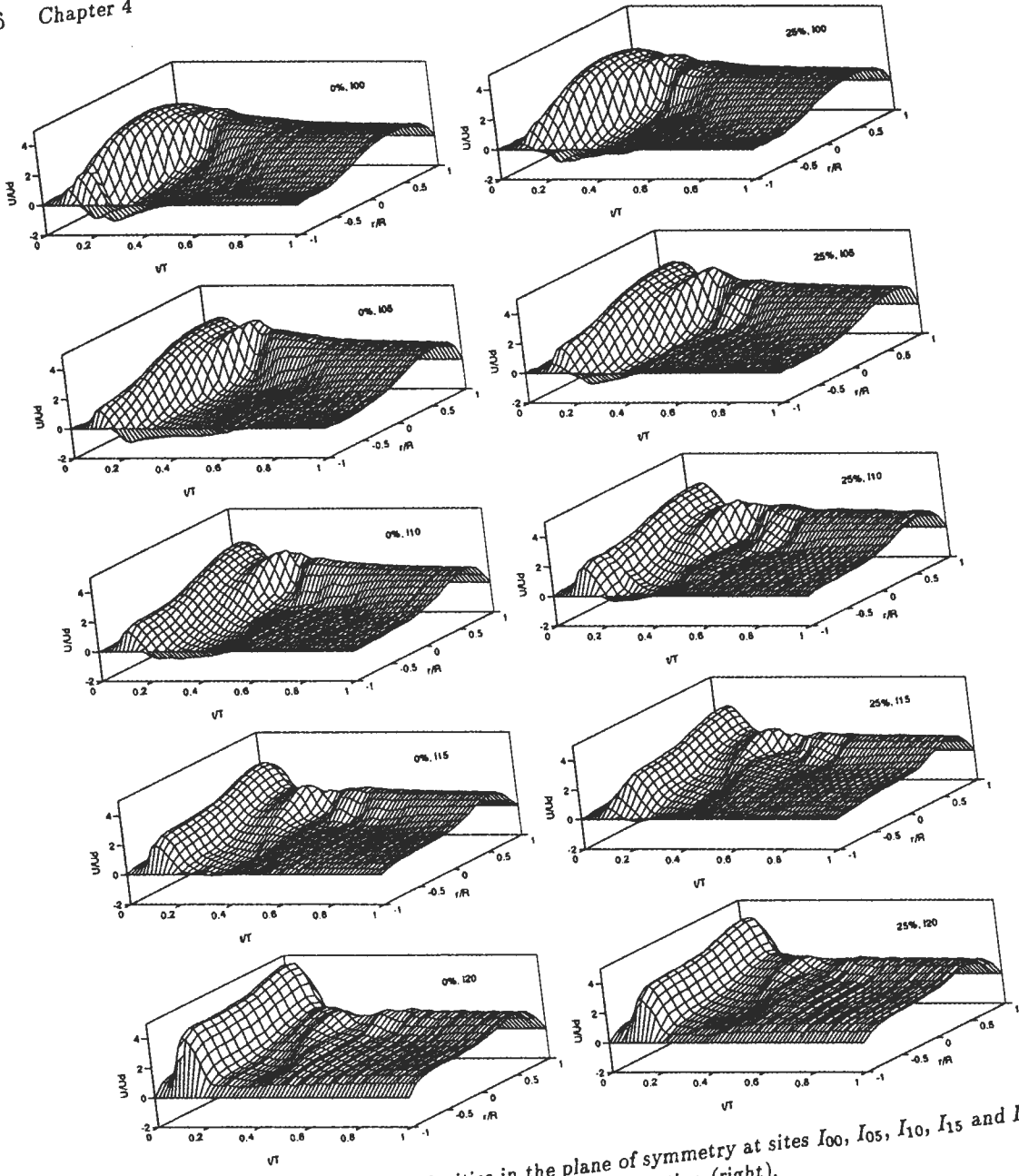
Figure 4.7: Measured axial velocities in the plane of symmetry at sites I_{00}, I_{05}, I_{10}, I_{15} and I_{20} for the non-stenosed (left) and the 25% stenosed bifurcation (right).

Description of the flow field along lines perpendicular to the plane of symmetry

Whereas in the previous paragraph the axial velocities in the plane of symmetry were considered, some features of the secondary flow field (causing the helical flow patterns as described in section 3.3) will be discussed presently. This is done with the help of figures 4.8 and 4.9, where the axial velocities and the secondary velocities along lines perpendicular to the plane of symmetry are plotted. In the figures the symmetry with respect to $r/R = 0$ is obvious. The flow phenomena can be summarized as follows.

site I_{00}: (figure 4.8) At site I_{00} after systolic deceleration a small dip in the axial velocity, appearing at $t/T = 0.2$, is followed by a peak at near wall sites at $t/T = 0.3$. From the figures of the secondary velocities (figure 4.9) it can be seen that the dip in the axial velocity at $t/T = 0.2$ coincides with a significant secondary flow at near wall sites directed from the divider side wall towards the non-divider side wall. From the figures of the axial velocities it is known that this also coincides with the occurrence of the region of reversed flow at $r/R = 0$ (the plane of symmetry). Soon after the occurrence of the secondary flow peak a second but smaller secondary flow peak can be discerned in figure 4.9 ($t/T = 0.3$) more towards the center of the internal carotid (at $r/R = 0.5$), showing similar flow features as described above. Apparently, two helical structures are found from which the cores move towards the center of the interna.

Comparison of the non-stenosed and the stenosed cases learns that the flow features are very similar. The only difference can be found in the slightly enlarged secondary velocities in the stenosed case.

site I_{05}: At site I_{05} the flow field looks very similar to that at site I_{00}. A small difference can be seen in figure 4.8, where the secondary flow peak has shifted to a later phase of the flow pulse. Moreover, the secondary flow at $r/R = 0.5$ seems to be stronger at site I_{05}.

sites I_{10} and I_{15}: Moving further downstream the secondary flow field seems to become less significant. In figure 4.8 the peak in the secondary flow field near the walls shifts to a later phase in the flow pulse and it also moves towards the center of the internal carotid. The smaller peak of the second helical pattern seems to become less and less important.

Comparing the non-stenosed and the stenosed cases it can be seen that in the stenosed case the secondary flow peak has shifted more towards the center of the channel ($r/R = 0.3$) compared to the non-stenosed case ($r/R = 0.5$). Moreover the amplitudes of the peaks are lower in the stenosed case. Apparently, the differences between the two models become more clear at sites I_{10} and I_{15}, though they remain relatively small.
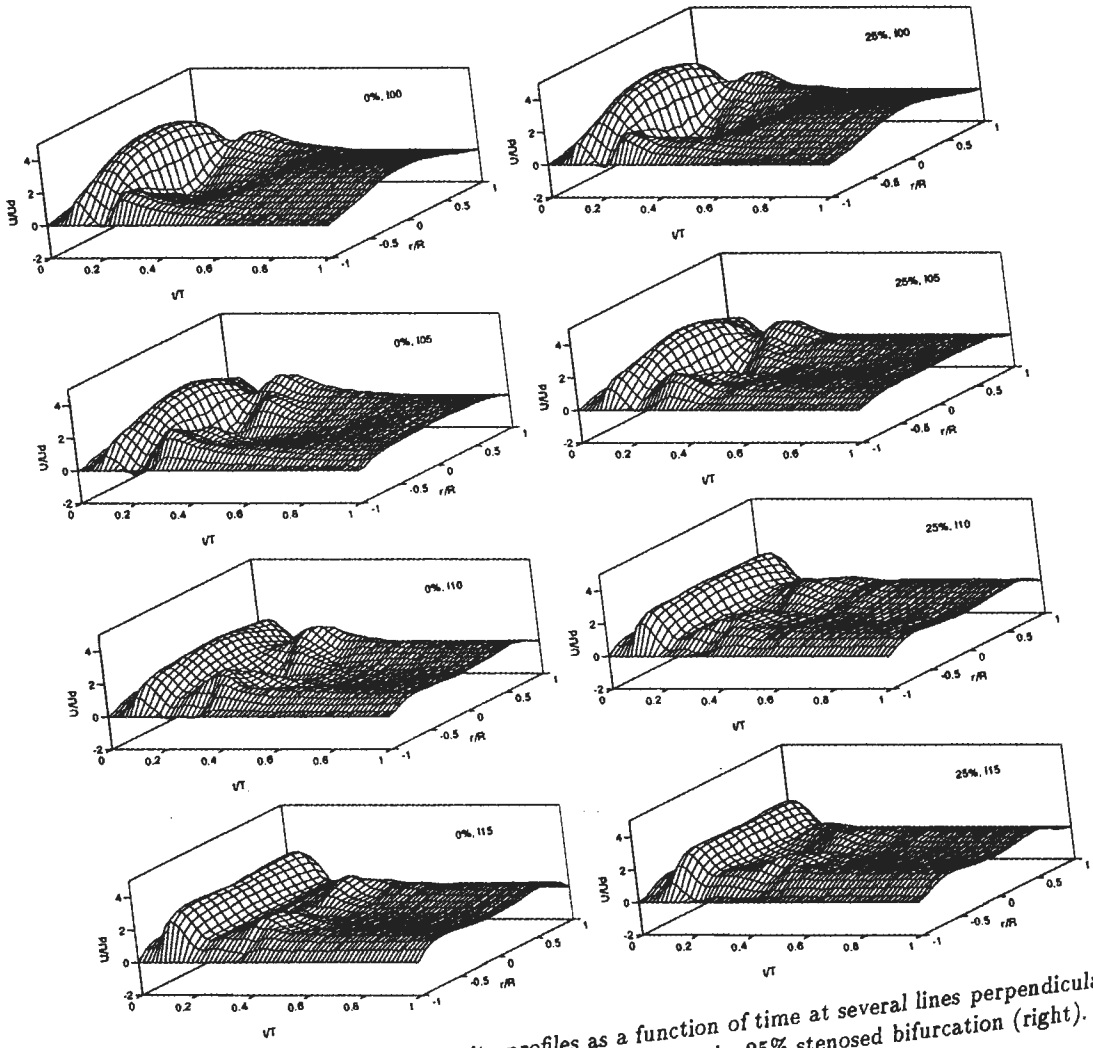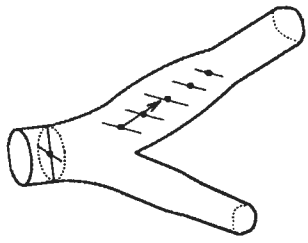
Figure 4.8: Measured axial velocity profiles as a function of time at several lines perpendicular to the plane of symmetry in the non-stenosed (left) and the 25% stenosed bifurcation (right).
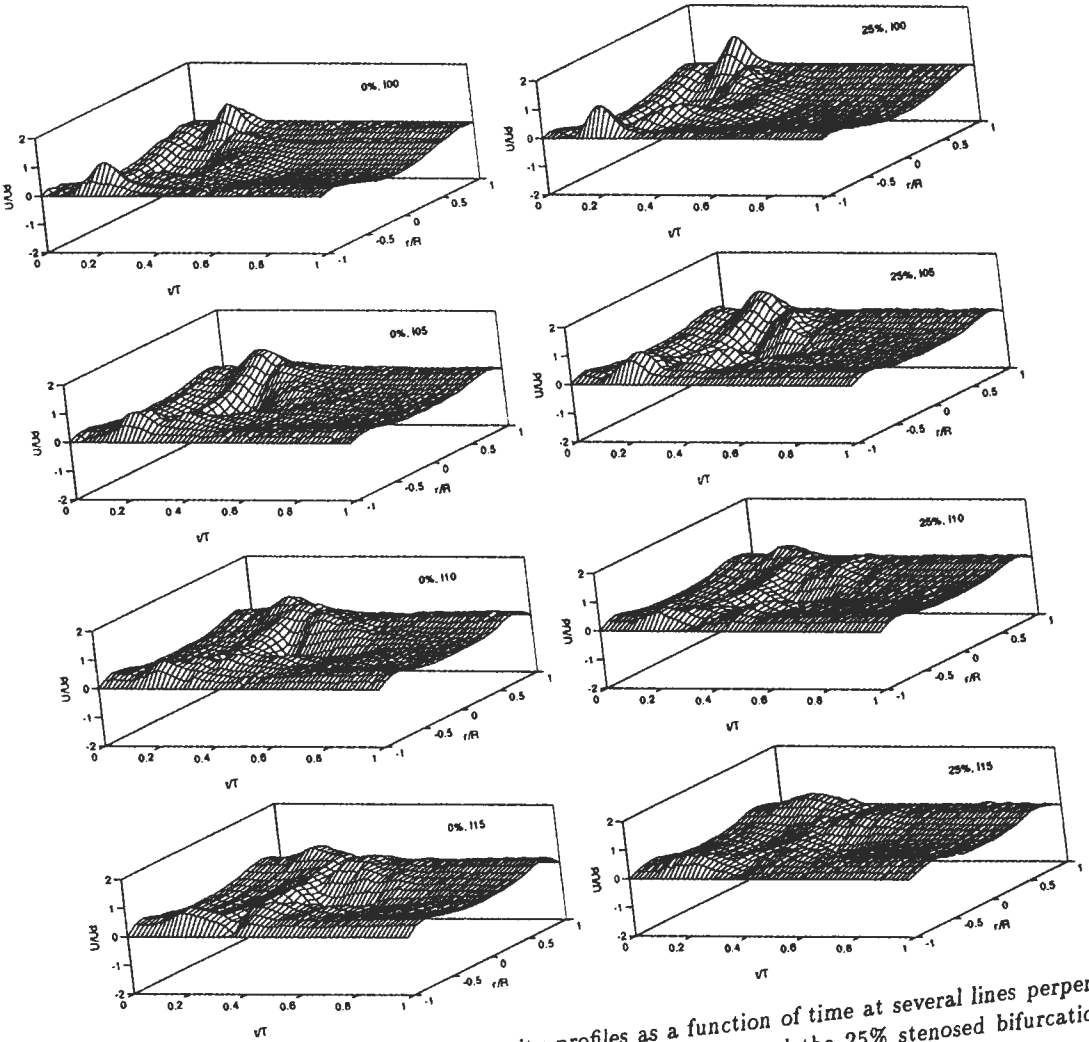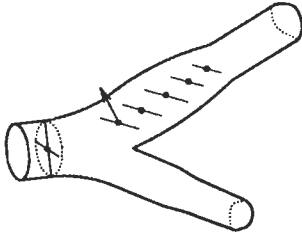
Figure 4.9: Measured secondary velocity profiles as a function of time at several lines perpendicular to the plane of symmetry in the non-stenosed (left) and the 25% stenosed bifurcation (right).
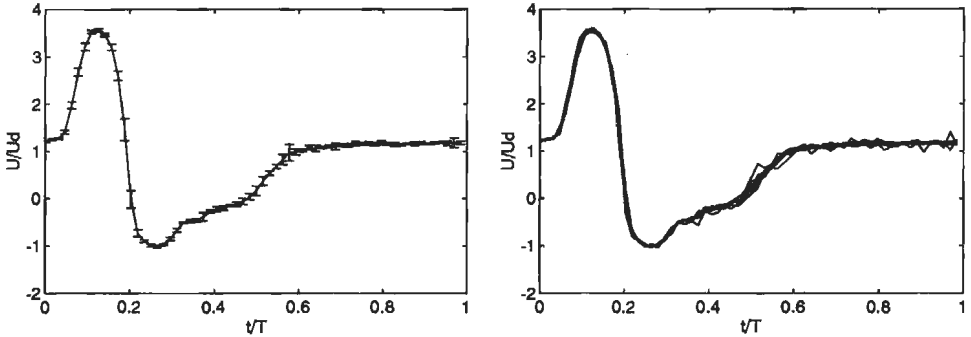
Figure 4.10: *Measurements of the axial velocities in the center point at site I_{00} for the 25% stenosed bifurcation; mean axial velocities and standard deviations as a function of time (left) and the eight periods from which the ensemble averaged velocities have been determined (right).*

4.4   Concluding discussion

Error estimates   The accuracy of the presented ensemble averaged velocity signals involves several aspects. (i) The error caused by the noise on the signal and the presence of a spatial velocity gradient in the measuring volume, is estimated by the Root Mean Square (RMS) values in stationary flow. In test experiments the RMS values appeared to be less than 1% for peak-systole and about 1% for diastolic flow. (ii) Due to significant temporal velocity gradients the application of the averaging procedure can lead to errors, that are estimated to be approximately 20% for steep temporal velocity gradients. To illustrate this, in figure 4.10 (left) the mean axial velocities as a function of time and their standard deviations

$$\sigma = \sqrt{\sum_{j=1}^{n}(x_j - \bar{x})^2/(n-1)} \tag{4.1}$$

are given for the center point at site I_{00}. Here $\bar{x}$ denotes the ensemble averaged velocity for each time interval and $n = 8$ represents the number of measurements to which the ensemble averaging procedure has been applied The errors, caused by the steep temporal velocity gradients predominantly occur during systolic acceleration and deceleration and mainly originate from small phase errors in the flow pulse. To show that the enlarged deviations during systolic deceleration do not originate from instabilities, the eight velocity measurements, from which the mean and the deviation are determined, are also presented in figure 4.10 (right). Clearly the broadening during systolic deceleration is caused by small phase shifts in the individual velocity measurements. The noise during diastole is caused by friction between the piston and the cylinder wall in the piston pump. (iii) Additional errors are introduced by the ensemble averaging procedure and the interpolation procedure in the case that no velocity measurements are available in a certain time interval. These

errors, however, only occur in the area with nearly zero velocities and they are estimated to be in the same order of magnitude as the resolution of the LDA measurements. For the range of velocities, used in the experiments, this resolution amounted $1\,mms^{-1}$. Since systematic errors induced by temperature fluctuations, misalignment of the system and evaporation of water from the salt solution (influencing the density, index of refraction and viscosity) are assumed to be much smaller, the error of the experiments is determined by the factors as described above.

Discussion of the flow features   The results of the velocity measurements in the two models compare well with the qualitative results of the visualization studies, as described in chapter 2. By means of both methods the following features are described: (*i*) the onset of a region with reversed flow near the non-divider wall during systolic deceleration; (*ii*) the oscillations that develop in the shear layer, indicating vortex formation.

The differences between the velocity patterns in the non-stenosed and the stenosed models are small. When studying the axial velocities in the plane of symmetry the differences mainly involve two aspects. First, a disturbance with elevated velocities appears in the region with flow reversal in the stenosed model, starting at $t/T = 0.3$. Secondly, oscillations and disturbances in the shear layer and the area with high velocity in the normal model, are more pronounced and seem to contain different frequencies in the stenosed model. Again it is noted that no disturbances of the velocities are found directly downstream the stenosis near the non-divider wall. This is due to the fact that the stenosis is located in a region with low velocities during the entire flow pulse. As a result, hardly any vorticity is created in the boundary layer at the wall of the stenosis and no significant vortex shedding occurs.

The global flow features as found in the non-stenosed model agree well with results from Ku *et al.* (1985a, 1987), who performed LDA measurements in a model of the carotid artery bifurcation, similar to the non-stenosed model in this study. The authors reported on disturbances of the shear layer as well. However, they attributed these oscillations to the oscillations of the (physiological) flow pulse, that was used. The experimental results described in this chapter show that these disturbances originate from vortex formation in the shear layer. In order to study the stability of the shear layer under pulsatile flow conditions in more detail, chapter 6 will be dedicated to this subject.

Chapter 5

Experimental validation of the numerical method

5.1 Introduction

In this chapter it is investigated whether the experimental results described in chapter 4, confirm the computational results presented in chapter 3. First a qualitative comparison between the computational results and the corresponding LDA results is made for the 25% stenosed model (section 5.2). Next in section 5.3 a quantitative comparison is made. Finally, the differences between the two methods are discussed (section 5.4).

5.2 Qualitative comparison

In figure 5.1 plots of the axial velocities along lines in the plane of symmetry (left) and the secondary velocities along lines in the plane perpendicular to this (right) are presented. A qualitative comparison with the LDA results for the 25% stenosed bifurcation, given in figures 4.7 and 4.9, learns that the global flow features show many similarities. However, also some striking differences between the numerical and experimental results of the axial velocities in the plane of symmetry can be discerned: (i) the computed axial velocities in the reversed flow area are more negative at sites I_{00}, I_{05} and I_{10}, whereas this area disappears at an earlier phase in the flow pulse in the computations; (ii) though the computed axial velocities also predict oscillations near the shear layer, the time scale of these oscillations is much smaller than that of the experimental results; (iii) the amplitude of the oscillations of the computed axial velocities near the shear layer is large compared to the experimental results, especially at sites I_{15} and I_{20}.

The secondary velocities along lines perpendicular to the plane of symmetry (right-hand side plots of figure 5.1) show similar features as described above: a smaller time scale of the oscillations in the computed velocities and larger amplitudes of these oscillations.
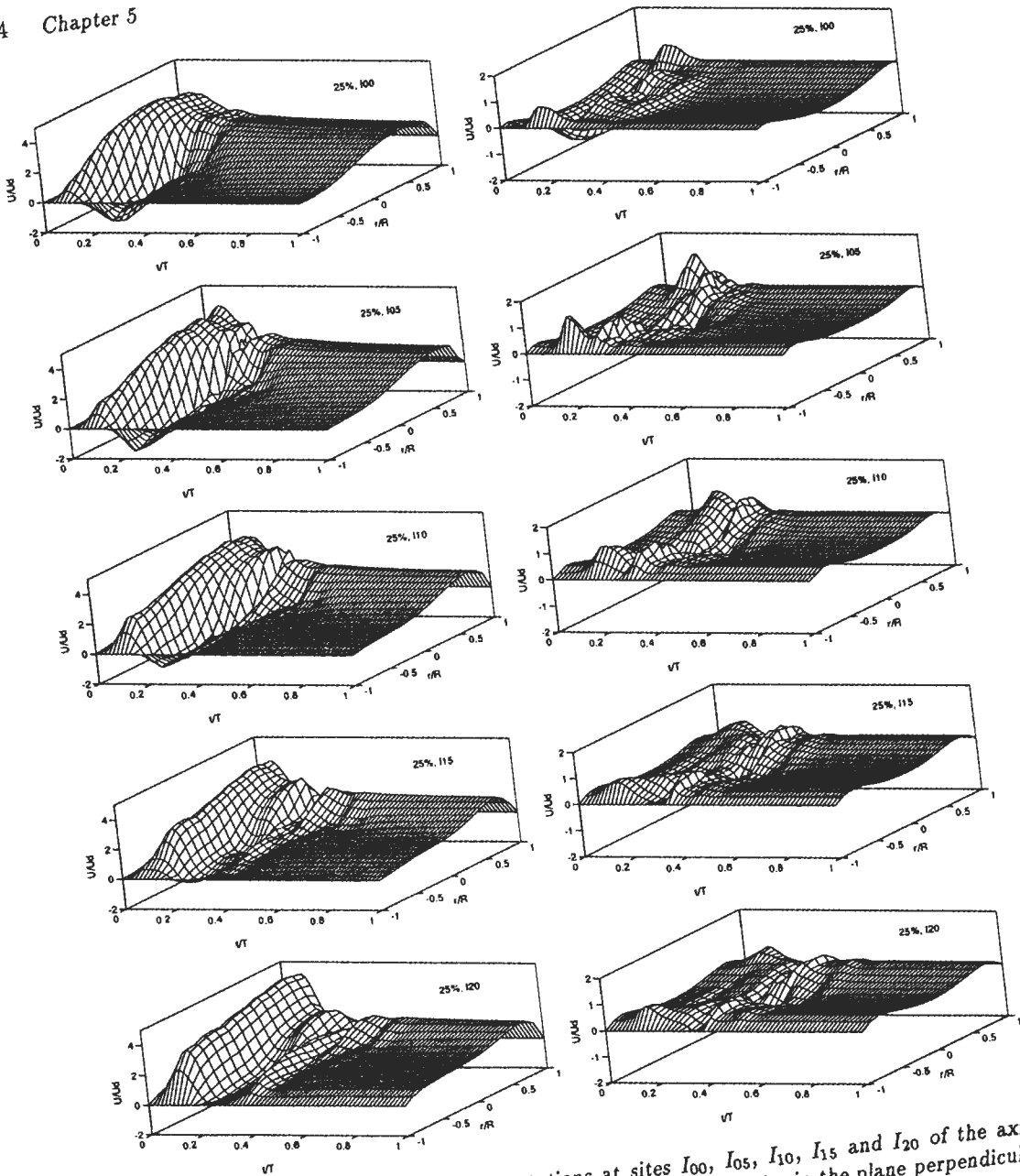
Figure 5.1: Results of the FEM computations at sites I_{00}, I_{05}, I_{10}, I_{15} and I_{20} of the axial velocities in the plane of symmetry (left) and the secondary velocities in the plane perpendicular to this (right); compare this figure with figures 4.7 (left) and 4.9 (left).

5.3   Quantitative comparison

In figure 5.2 the experimental and numerical axial velocities along lines in the plane of symmetry are given as a function of time. The experimental and numerical results are represented by markers (o) and solid lines (—) respectively. The upper and lower lines represent the divider and the non-divider wall. In figure 5.3 the secondary velocities along lines in the plane, perpendicular to the plane of symmetry, are given. Here, the upper lines are lines of symmetry, whereas the lower lines represent the side walls. The differences between the experimental and numerical results are summarized below.

- The computed systolic deceleration of the axial velocities is larger (sites I_{05} and I_{10}).

- The computed radial extension of negative axial velocities is larger and disappears at an earlier phase of the flow pulse (see for example at site I_{10}). Moreover the computed velocities in this area are more negative as compared to the experiments.

- The numerically predicted unsteady behavior of the velocity in the shear layer is significantly different from the experimental results. The time scale of the computed disturbances is smaller than in the experiments. This can also be seen in the results of the secondary velocities.

- The enlarged axial velocities in the area with low velocities, found in the experimental results at site I_{15}, are hardly present in the computations.

- In contrast to the results from the LDA experiments, at site I_{20} distinct disturbances are present in the computational results (see also figure 5.1).

5.4   Concluding discussion

In the preceding sections it has been shown that though the computations show features similar to the features in the experiments, the time scale and amplitude of the oscillations near the shear layer are different for the two methods. In the present sections these differences and their causes will be discussed.

Firstly, the FEM results show numerical disturbances near the divider wall at sites I_{00}, I_{05} and I_{10} (see also figure 5.1). These disturbances probably originate from inaccuracies, caused by the influence of the apex, where large radial velocity gradients occur. Local mesh refinement is expected to diminish this effect. Secondly, the computational results are not as smooth as the experimental results. At sites I_{05}, I_{10} and I_{15} numerical oscillations are present, that are invoked during systolic deceleration at site I_{05}. This is probably due to the large temporal and radial velocity gradients, causing the numerical solution to become inaccurate. To study the computational accuracy, the influence of both *mesh refinement* and increasing the *number of time steps* per period, should be investigated. As stated before in chapter 3 *mesh refinement* can practically not easy be performed at this moment,
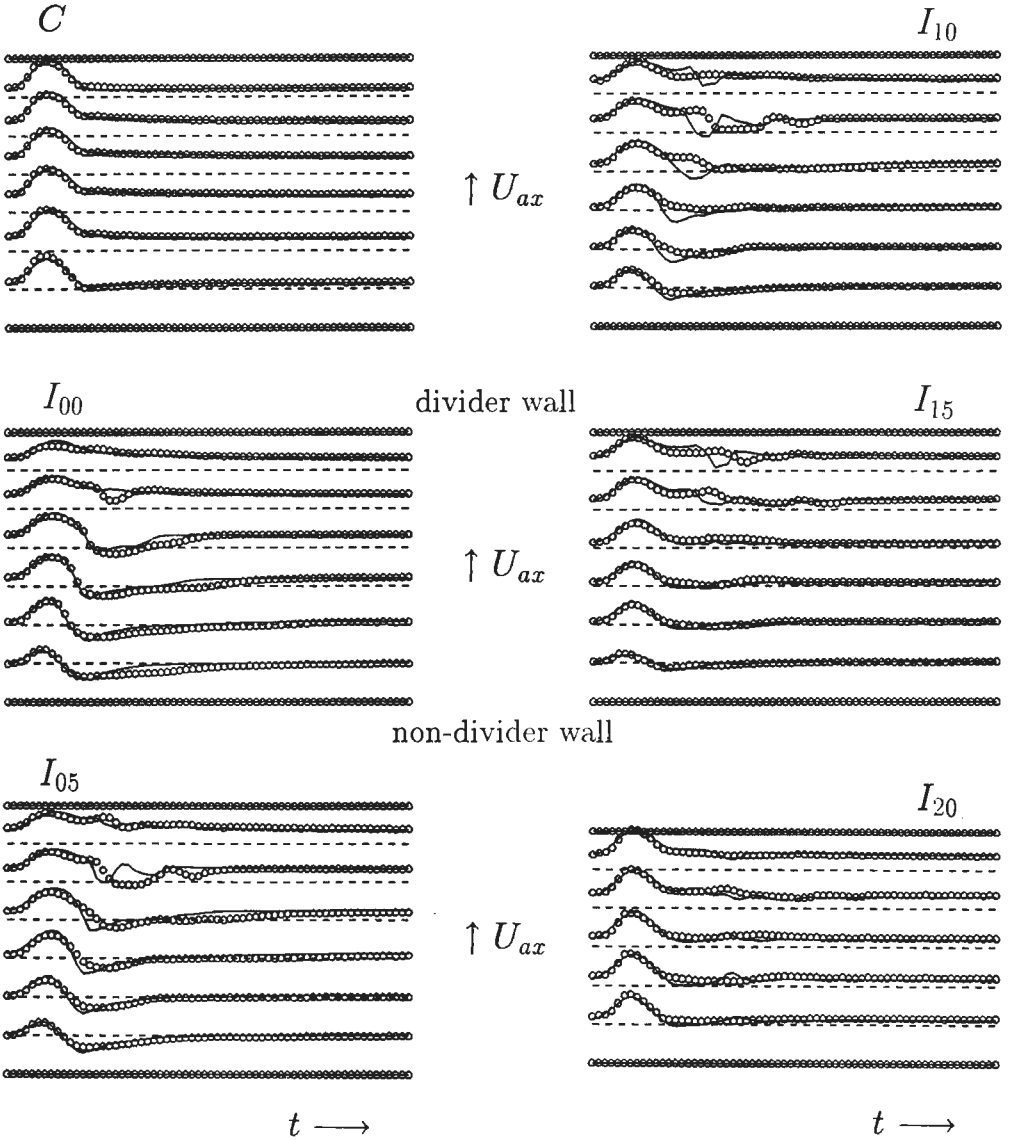
Figure 5.2: *Experimental (o) and numerical (—) results of the axial velocities for several points in the plane of symmetry at sites C, I_{00}, I_{05}, I_{10}, I_{15} and I_{20}.*
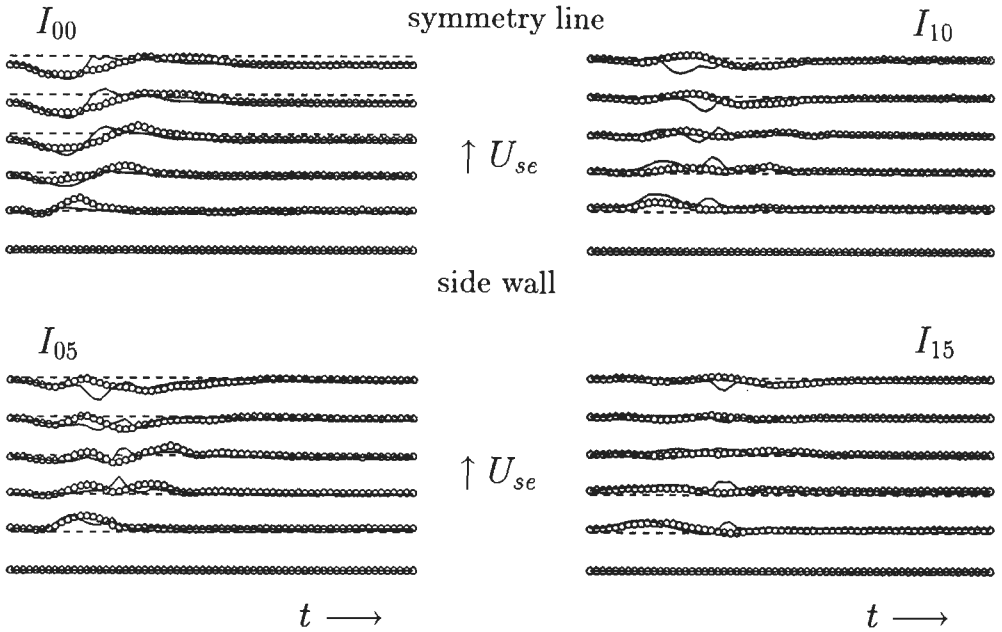
Figure 5.3: *Experimental (o) and numerical (—) results of the secondary velocities for several points in the plane perpendicular to the plane of symmetry at sites I_{00}, I_{05}, I_{10} and I_{15}.*

due to the very time and memory consuming character of the computations. Nevertheless, it is expected to give an increased numerical accuracy with smoother results. The influence of the *number of time steps* per period is shown in figure 5.4, where the computed axial velocities in the plane of symmetry at site I_{05} at location $r/R = 0.45$ (left) and $r/R = 0.64$ (right) are given. The dotted and solid lines represent computations with 128 and 256 time steps per period respectively. It appears that the computational results are only influenced by the size of the time step for $t/T = 0.2$ up to $t/T = 0.4$. This influence involves two aspects: by increasing the number of time steps the amplitude of the numerical oscillations decreases (see left plot of figure 5.4) and the oscillations may even fully disappear (see right plot of figure 5.4). Evaluating these results it seems to be significant to use even more time steps. Since the computations are very expensive, only for the 50% stenosed bifurcation (see also chapter 8), 512 time steps per period have been used.

Not only the computations suffer from inaccuracies. Also the LDA experiments intro- duce experimental errors, as described in section 4.4. To show that the numerical and experimental results differ significantly even when the experimental deviation is taken into account, in figure 5.5 the experimental results together with their standard deviation (see also section 4.4) are compared to the FEM computations for the center point at site I_{00}. Since the experimental errors are found to be small compared to the differences between
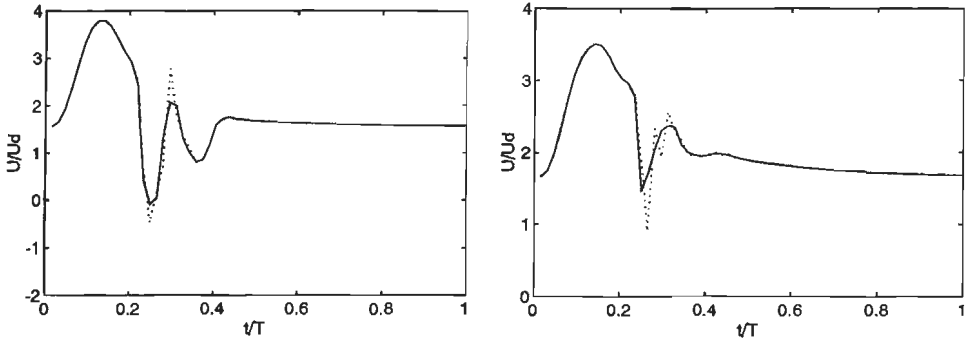
Figure 5.4: *Computed axial velocities in the plane of symmetry at site I_{05} at location $r/R = 0.45$ (left) and $r/R = 0.64$ (right). The dotted and solid lines represent computations with 128 ($\cdot\,\cdot\,\cdot$) and 256 (—) time steps respectively.*

the experimental and numerical results, it must be concluded that the computations are not suitable for the description of the unstable shear layer behavior from $t/T = 0.2$ up to $t/T = 0.5$. In figures 5.2 and 5.3 it was shown that especially the time scale of the unsteady shear layer behavior was smaller in the computational case. Since detailed information on this shear layer behavior is needed to describe the influence of the 25% stenosis, the computations are not suitable for that purpose. Nevertheless, the computations still give a useful and clear insight into the complex three-dimensional axial and secondary flow fields in the non-stenosed and the 25% stenosed carotid artery bifurcation.
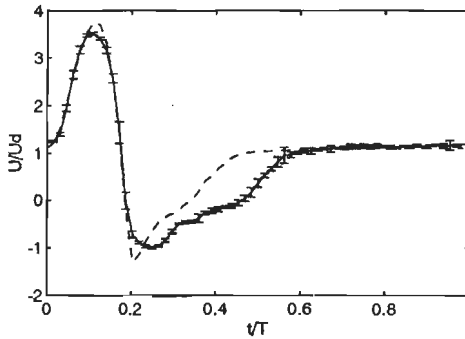
Figure 5.5: *Comparison of the experimental (—) and computational results (- -) for the center point at site I_{00} of the 25% stenosed bifurcation.*

Chapter 6

Model study on unsteady free shear layer behavior

6.1 Introduction

In the preceding chapters it has been shown that vortex formation occurs in the shear layer in the initial phase of diastole. Moreover, the shear layer appears to be a location that is sensitive to the presence of stenoses. Therefore in this chapter, the unsteady free shear layer behavior is studied in more detail. Because of the geometrical complexity of the three-dimensional carotid artery bifurcation and the occurrence of a strong secondary flow field in this bifurcation, here a simplified two-dimensional (2D) channel flow is considered. The shear layer is artificially formed by merging two parallel flows, initially separated by a thin plate (see also figure 6.1). By variation of the flow ratio between the upper and lower fluid flows the gradient of the axial velocity in the shear layer at a certain position can be influenced.

At first in section 6.2 some results from literature on shear layer instabilities will be given. To study this two-dimensional shear layer, similar experimental and numerical methods as described in chapters 3 and 4 respectively have been used. Specific details of the methods are described in section 6.3. Next the results of the experimental and
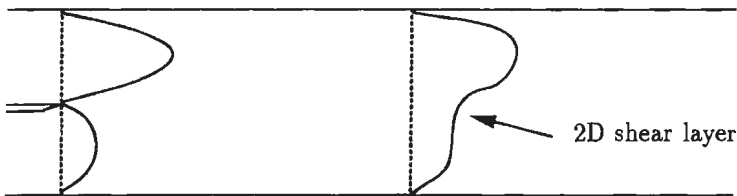
Figure 6.1: *Creation of a shear layer between two parallel flows in a two-dimensional channel.*

numerical analysis of the free shear layer are described (section 6.4). Finally, in section 6.5 a concluding discussion of the results is given. As far as possible a comparison with data from the literature on unsteady free shear layer behavior is made. Also the relevance of the two-dimensional shear layer results for the flow in the carotid artery bifurcation is discussed.

6.2   Some results from literature

The theory of hydrodynamic stability deals with the question whether laminar flows become unstable or not and how phenomena, occurring in unstable flows, can be described and understood. Physically the stability of a flow can be subdivided into three categories (Drazin and Reid, 1981): (*i*) a flow is called (asymptotically) stable when small disturbances of the undisturbed main flow die away; (*ii*) neutral stability occurs when the disturbances persist as disturbances of similar magnitude; (*iii*) a flow is called unstable when the disturbances grow in time (temporally) or in space (spatially). In appendix C a brief survey of the development of unstable flow behavior in shear layers assuming incompressible parallel fluid flow will be given. At first an example of the linear stability analysis for an unbounded inviscid and steady 2D shear flow is given, known as the Kelvin-Helmholtz instability. Next, some attention is paid to non-linear effects, that are responsible for phenomena like vortex roll-up and pairing of vortices. Finally the influences of viscosity and walls are briefly discussed.

Since in this thesis unsteady flows are considered, here we will focus on the influence of the unsteadiness of the main flow. The stability of unsteady flows is a relatively new and little studied topic in the theory of hydrodynamic stability. The mathematics are more difficult and even the meaning of instability is not clear when the main flow changes substantially with time. Davis (1976) used the following definitions to classify the stability of time-dependent periodic flows, (*i*) a periodic flow is called monotonically stable when each disturbance is damped on each moment; (*ii*) when every perturbation experiences a net growth over every period of the undisturbed main flow, the flow is called unstable; (*iii*) transient stability occurs when a perturbation only grows during part of the cycle, reaches a maximum amplitude and is damped next.

Unsteadiness of the main flow may introduce new mechanisms of instability. For main flows that are periodic in time this is the parametric instability or parametric resonance (Drazin and Reid, 1981). The essential mechanism is a resonance between the forced oscillation of the main flow and the natural perturbations of the flow, only when the frequency of the natural perturbation is half or an integral multiple of the frequency of the forced oscillation. In figure 6.2 an example of such a subharmonic resonance in stratified fluid flow is given. The upper shear is perturbed sinusoidally at half of the frequency of the natural perturbation, such that the motion is locked into the subharmonic. The figure corresponds to figure C.2, where the natural perturbation of the shear layer was shown.

Finally, some remarks on the initiation of disturbances in unsteady shear layers are made. For linear instability of steady flows the presence of initial disturbances is of utmost

Figure 6.2: *Parametric resonance in an unsteady Kelvin-Helmholtz flow. The upper stream is perturbed sinusoidally at half of the natural frequency and as a result the motion is locked into the subharmonic. (Copyright ©Van Dijke 1982, The parabolic press - Reprinted with permission).*

importance. Disturbances tend to emerge with frequencies, corresponding to the largest growth factors. After the stage of exponential growth, non-linear effects cause the shear layer to roll-up and pairing of vortices may occur. In time-dependent flows the situation is essentially different from the steady situation, since vorticity can be generated by time varying flows. For example consider a splitter plate in a bounded 2D channel. By varying the inflow conditions as a function of time for the upper and the lower part of the channel, a time varying vorticity (being dependent on the velocity difference $\Delta U(t) = U_1(t) - U_2(t)$) is shed at the separation point at the rear edge of the splitter plate and is convected with the fluid. If ΔU is kept constant, no disturbances of the shear layer will occur. In general the vorticity that is created at the rear edge of the splitter plate, varies with time and as a result an inhomogeneous vortex distribution in space will be present in the vortex layer. This inhomogeneous vortex distribution will be the initiator for instabilities to occur. The disturbances amplify and beyond a certain threshold roll-up of the shear layer occurs.

With this in mind, in this study we will focus on the evolution of initial disturbances in the shear layer, which are assumed to be caused by the time-dependent inflow conditions.

6.3 Methods

Visualization and LDA experiments

In order to generate a two-dimensional (2D) shear layer a 2D settling chamber and a measuring section have been constructed. The measuring section consists of a 2D channel with a height of $2H$ ($H = 5\,mm$) and a width of $12H$. The settling chamber with flow contractor is divided into two channels by a splitter plate, which has a thickness of $H/5$. In figure 6.3 this is schematically drawn. Downstream the flow contractor, the splitter plate extends for about $9H$ into the measuring section. The rear edge of the splitter plate is also presented in figure 6.3 and has an angle of approximately 16^0.

For the generation of the flow pulse the gear pump and piston pump as described in section 4.2 are used. The shape of the flow pulse is given in figure 6.4. The Reynolds
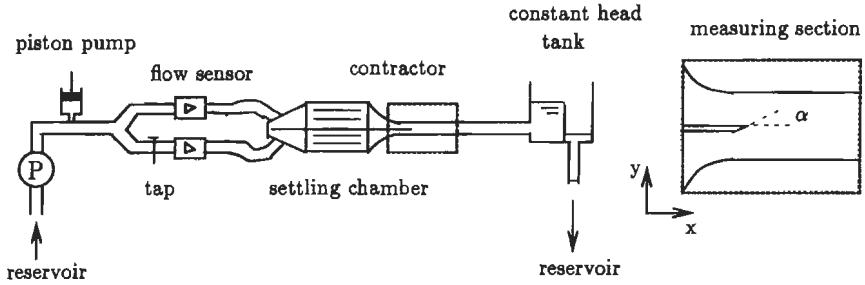
Figure 6.3: *Schematic representation of the experimental equipment for studying the 2D shear layer (left) and the measuring section with splitter plate (right).*

number varies from $Re = 270$ during diastole (which corresponds to a value of the cross-sectional averaged end-diastolic velocity of $U_d = 28.5\,mms^{-1}$) to $Re = 1000$ at peak-systole. The Womersley parameter amounts $\alpha = 6$, corresponding to a period time of $T = 4.33\,s$. The flow ratio between the bottom flow and the upper flow is also given in figure 6.4 and amounts about 0.37 during diastole. Due to the time varying difference in the absolute velocities between the bottom and the upper part during systole, a time varying vorticity is shed at the rear edge of the splitter plate. As a measuring fluid a solution of NaCl in water is used, enabling the flow measurements by means of the electromagnetic flow meters.

For the visualization of the shear layer, fluorescent dye is injected into the upper fluid before it enters the settling chamber. The density of the dye is matched to that of the fluid by addition of ethanol and NaCl, so that gravity influences can be neglected. Before the upper fluid enters the measuring section, the dye has mixed completely to a homogeneous colored fluid. From the top of the channel a sheet of light parallel to the x-y plane is
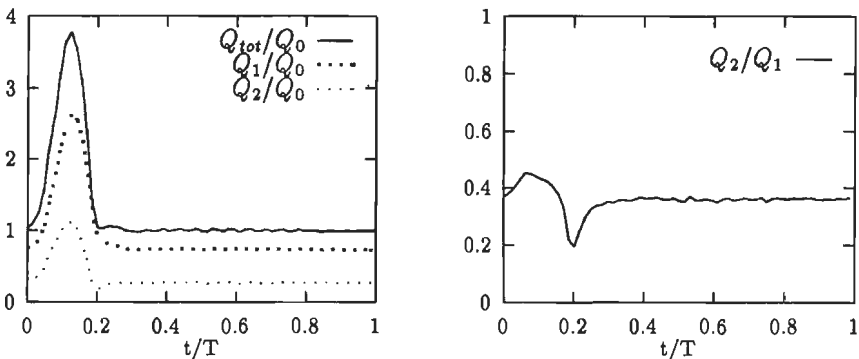
Figure 6.4: *The flow pulse in the visualization experiments, made dimensionless with the end-diastolic flow rate $Q_0 = 0.97\,l/min$ (left) and the flow ratio between the lower and the upper flow in the two-dimensional channel (right).*

created in the center of the channel with respect to the z-axis. The fluorescent dye scatters the incident light in all directions and the development of disturbances in the two-dimensional shear layer is made visible. The experiments have been recorded on video tape.

The LDA experiments have been performed with the equipment as described in section 4.2. Axial velocities have been measured as a function of time along lines parallel to the y-axis at several axial distances from the rear edge of the splitter plate $(Y_0, Y_4, Y_8,...)$ as given in figure 6.5. Here the subscripts represent the dimensionless axial distance from the measurement site to the rear edge of the plate relative to H. Also measurements have been performed along a line parallel to the x-axis, represented in figure 6.5 by X_0. The spatial distance between two measuring points in x-and y-direction is $5\,mm$ and $0.5\,mm$ respectively. The data acquisition and processing is similar to those described in section 4.2, resulting in ensemble averaged axial velocities derived from 9 periods. The results have been plotted in a similar way as described in chapter 4 and the reader is referred to this chapter for further details.
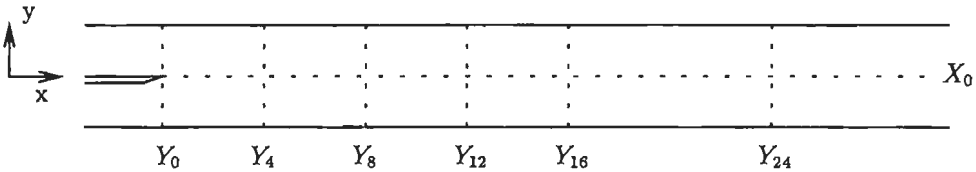
Figure 6.5: *Overview of the measuring lines along the x-axis and y-axis.*

Finite element computations

For the computation of the two-dimensional velocity field the finite element method as described in chapter 3, is used. Here the penalty function parameter is chosen to be $\epsilon = 10^{-6}$ (see also section 3.2). A Crank-Nicholson scheme $(\theta = 0.5)$ is applied for the time discretization. The flow pulse is computed in 64 time steps. The computational domain has been subdivided into 2080 elements, using the 7-noded two-dimensional Crouzeix-Raviart element (see figure 3.1). The height and length of the channel are $2H$ and $30H$ respectively. The boundary conditions for the two-dimensional channel flow are as follows: (i) at the walls no-slip conditions are prescribed; (ii) at the outflow of the channel stress-free outflow boundary conditions are applied (see also equations 3.19 and 3.20); (iii) at the inflow the time-dependent axial velocities as obtained from the LDA measurements at site Y_0 (as given in figure 6.6) have been prescribed.
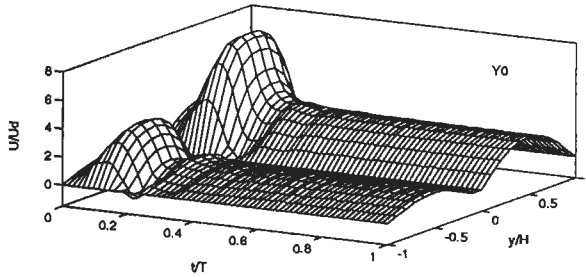
Figure 6.6: *LDA measurements of the axial velocities as a function of time at site Y_0. The data have been used as a boundary condition for the computations.*

6.4   Results

6.4.1   Flow visualization

The experimental and numerical visualization results of the developing disturbances in the shear layer are presented in figure 6.7 for several time steps of the flow pulse. For each time step three images are given: (i) a video print of the dye visualization experiment (top); (ii) a contour plot of the computational instantaneous stream lines of the velocity field (center) and (iii) a contour plot of the computational vorticity distribution of the 2D flow field (bottom). The vorticity distribution Ω is determined by calculating $\Omega = \partial v / \partial x - \partial u / \partial y$ of the computed velocity field. In the plots of figure 6.7 the y-axis is scaled with factor 5 to improve the resolution of the figure.

The evolution of the flow disturbances in the shear layer as a function of time will be described. Starting at the onset of systole of the flow pulse ($t/T = 0$), it can be seen from figure 6.7 that small disturbances from the previous flow pulse are remaining at about $25H$ downstream the rear edge of the splitter plate. During systole these disturbances are convected downstream and they have completely disappeared at peak-systole (see figure 6.7 at $t/T \approx 0.1$). During systolic deceleration small disturbances in the shear layer appear and at $t/T \approx 0.19$ small perturbations with wavelength ($\lambda = 8\,mm$) are obvious in both the experimental and numerical visualization results. The perturbations propagate with a velocity of about $71\,mms^{-1}$. These perturbations grow during the first part of the diastole and at $t/T \approx 0.25$ the amplitude has significantly increased. Next at $t/T \approx 0.38$ pairing of vortices can be observed, resulting in disturbances with wavelengths of $\lambda = 16\,mm$ and $\lambda = 20\,mm$, determined from both the experiments (with an uncertainty of $2.5\,mm$) and the streamline plots. During diastole the amplitude of the disturbances decreases and the wavelength slightly enlarges. The disturbances are convected downstream with a propagation velocity of 36 up to $42\,mms^{-1}$ during diastole.

The results of the dye visualization are qualitatively in good agreement with the finite element computations. Both methods predict the generation of disturbances during
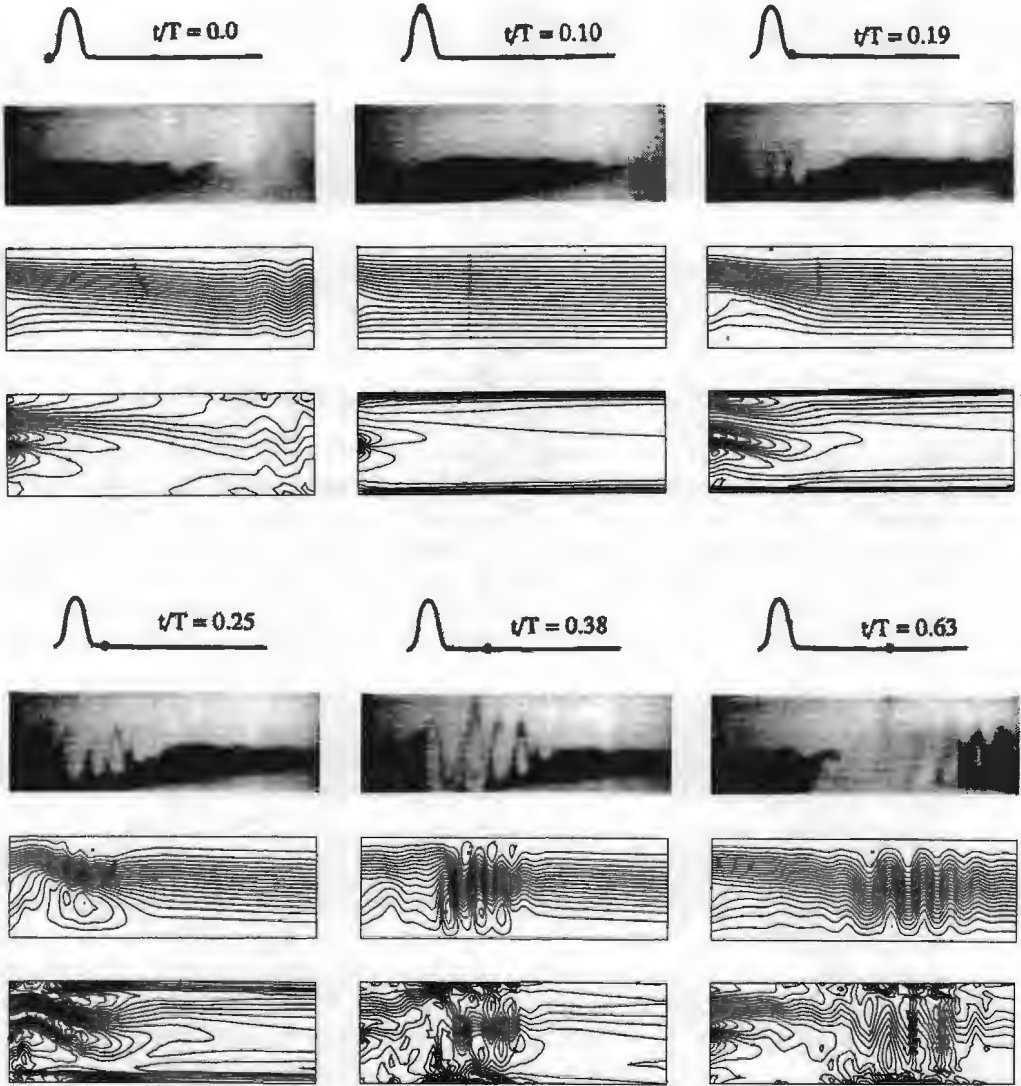
Figure 6.7: *Experimental and numerical visualization of the development of disturbances in the 2D shear layer; experimental dye visualizations (top), computed instantaneous stream lines (center) and computed vorticity distributions (bottom figures).*

systolic deceleration, the vortex pairing at $t/T \approx 0.38$ and the decreasing amplitudes and slightly increased wavelengths later in diastole. Moreover the propagation velocities of the disturbances and the wavelengths are in good quantitative agreement.

6.4.2   Axial velocity profiles

In this section the results of the LDA measurements and FEM computations of the axial velocities are presented. First the profiles along lines parallel to the y-axis are shown. The LDA measurements at site Y_0 have already been presented in figure 6.6. The experimental and numerical results at sites Y_4, Y_8, Y_{12}, Y_{16} and Y_{24} of the measuring grid from figure 6.5, are presented in figure 6.8. At the left-hand side the results of the LDA measurements are shown and at the right-hand side the FEM computations are presented. The parameters time, velocity and position have been made dimensionless by dividing by the period time of the flow pulse T, the end-diastolic value of the cross-sectional averaged velocity U_d and half the height of the channel H respectively. In the figure $y/H = -1$ defines the bottom wall of the flow channel and $y/H = +1$ the upper wall. A short description of the axial velocity field as a function of time will be given for the different sites.

site Y_0 Starting at the end of the rear edge (figure 6.6) it can be seen that a considerable boundary layer already has developed at both the splitter plate and the walls. During diastole the velocity profiles are nearly parabolic in the upper and lower half of the channel. At the onset of diastole a dip in the velocities in the bottom part of the channel is evident, followed by a moderate oscillation of the axial velocities in the upper and lower part of the channel. This dip is related to the dip in the flow ratio from figure 6.4. Near the bottom wall a small region with flow reversal can be seen.

site Y_4 A disturbance can be seen both experimentally and numerically during systolic deceleration. In the upper part of the channel the axial velocities are enlarged compared to the inflowing main stream, while in the lower part even negative velocities are observed. This phenomenon points to the presence of a vortex in the shear layer. Also some small oscillations in the axial velocity can be seen for times up to $t/T \approx 0.5$.

sites Y_8 and Y_{12} Further downstream the disturbances have shifted to later phases of the flow pulse. Some of the small disturbances from site Y_4 have developed into clearly visible vortices. Moreover, the shear layer and the disturbances have slightly shifted towards the bottom wall during systolic deceleration and in the initial phase of diastole. At later times the shear layer shifts to its original position in the center of the channel again, in accordance with the visualization results from figure 6.7.

sites Y_{16} and Y_{24} From the numerical results it can be seen that the vortices pass the measuring site at later phases in the flow pulse (due to convection of the vortices) and the amplitude of the structures diminishes (due to viscous forces).

The LDA results of figure 6.8 only show significant disturbances at sites up to Y_8. More downstream the vortex structures become indistinct or even disappear (at Y_{24}), while at
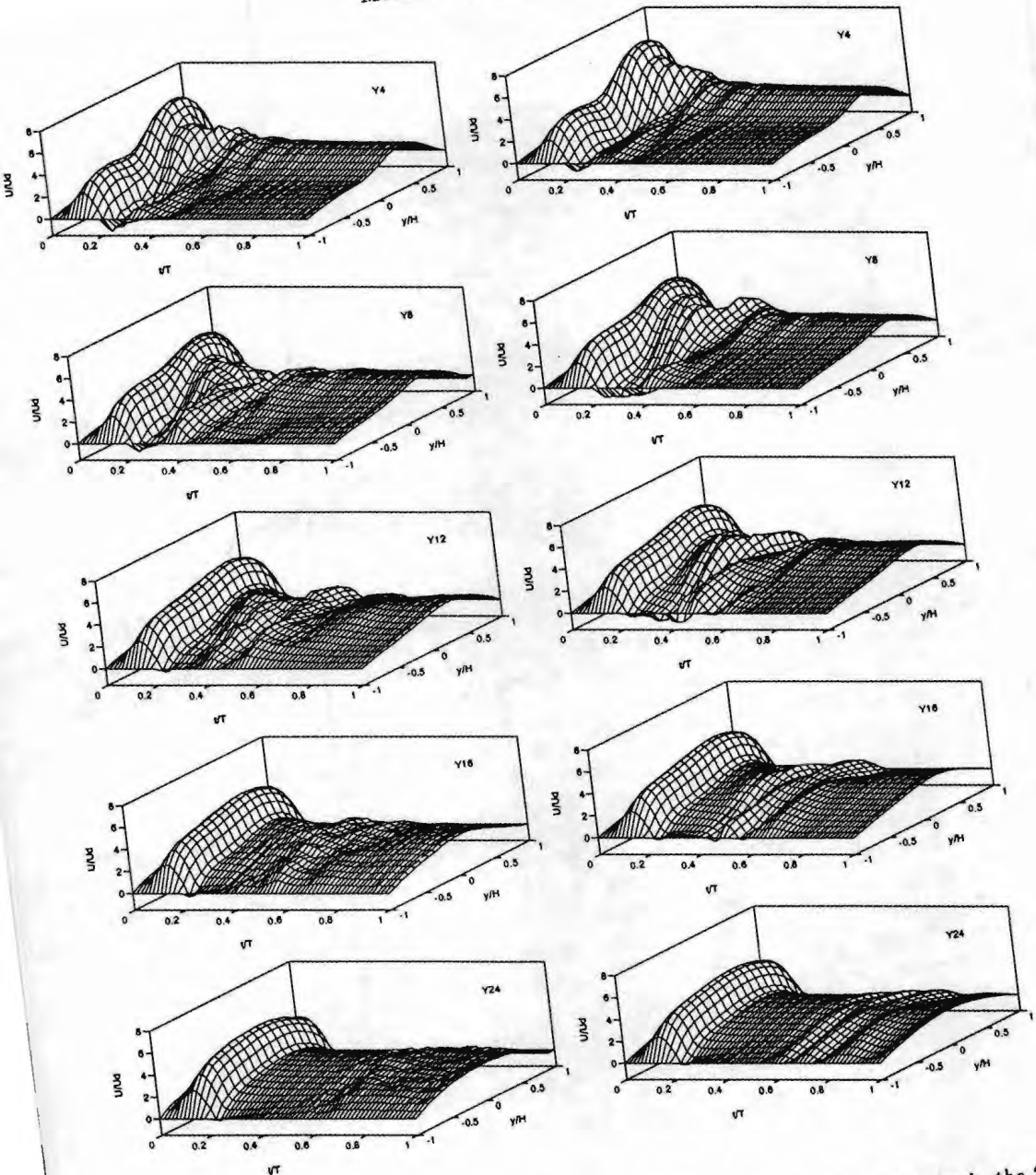
Figure 6.8: LDA results (left) and FEM computations (right) of the axial velocities in the 2D shear layer at sites Y_4, Y_8, Y_{12}, Y_{16} and Y_{24}
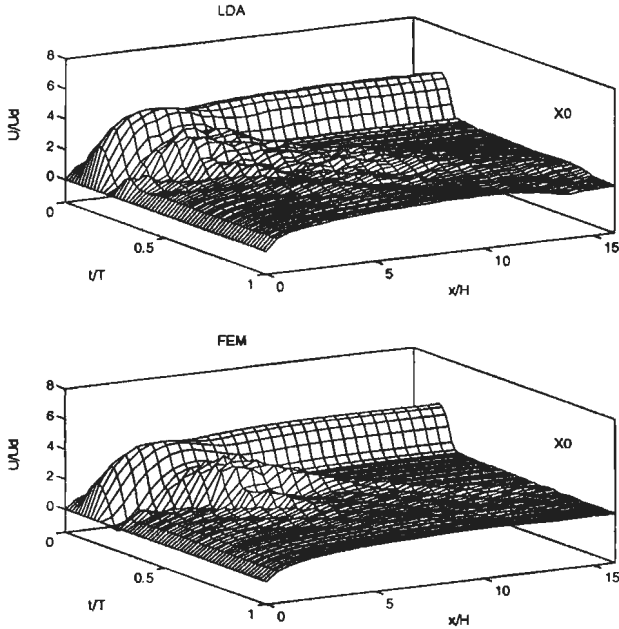
Figure 6.9: *LDA results (top) and FEM computations (bottom) of the axial velocities along the centerline of the channel with respect to the height.*

these sites vortices are still predicted in the computations. This fact is related to the ensemble averaging procedure and is discussed in section 6.5.

Next the axial velocities along lines parallel to the x-axis are presented. In figure 6.9 the LDA and FEM results are given for the centerline of the channel with respect to the height of the channel. Starting from position $x/H = 0$ (the rear edge of the splitter plate) it can be seen that for positions up to $x/H \approx 7$ disturbances are present during systolic deceleration. These disturbances travel forward with a propagation velocity varying from 36 up to $47\,mms^{-1}$. The amplitude of the disturbances diminishes with increasing time. The experimental and numerical results are qualitatively in good agreement. Quantitative differences appear as the computations predict small oscillations even for $x/H > 20$ in contrast to the LDA experiments (see also section 6.5).

6.5   Concluding discussion

A model study on shear layer behavior in 2D channel flow is described. To study the global features of the 2D shear layer behavior visualization experiments, LDA experiments and FEM computations have been performed. It appears that during systolic deceleration instabilities can be observed within 7 downstream the rear edge of the splitter plate. In

this stage the disturbances, having a wavelength of 8 *mm* seem to grow exponentially in time. During diastole the non-linear effects become more important, resulting in roll-up of the shear layer and pairing of vortices. As a result the wavelengths are approximately doubled to values varying from 16 up to 20 *mm*, due to the vortex interaction. The vortices move with velocities varying from 36 up to 47 *mms*$^{-1}$, which is approximately equal to the local velocity of the main flow. The amplitude of the structures diminishes for more downstream sites, due to diffusion and viscous dissipation.

Comparison of results with literature data   From the results it can be concluded that transient instability occurs in the 2D shear layer, according to the definition of Davis (1976). The instability can be interpreted as a temporal Kelvin-Helmholtz instability as described in appendix C. The spatial disturbance that initiates this temporal Kelvin-Helmholtz instability is caused by the time-dependent vortex shedding from the rear edge of the splitter plate. These disturbances are weak, which means that they do not locally disturb the flow around the splitter plate. They are convected with the fluid and meanwhile the small initial disturbances grow in time until non-linear terms cause the shear layer to roll-up. If an observer moves with the convective velocity of the disturbances, the pattern is that of a local temporal Kelvin-Helmholtz instability.

The role of the unsteadiness of the main flow on the vortex generation seems to be different from the parametric instability in an unsteady shear layer as described in section 6.2. In studies of parametric instability mostly harmonic disturbances are considered with small amplitudes compared to the steady flow component (Drazin and Reid, 1981). In the present study a quite different flow pulse is considered, since many harmonics of large amplitude are present. Therefore it is believed that in this study parametric instability does not occur. In the present study however, the unsteadiness of the flow has acted as a generator of vorticity, due to the time varying vorticity generation.

Relation to the flow in the carotid artery bifurcation   Obviously the disturbances which grow in the 2D shear layer behind the splitter plate and the disturbances occurring in the shear layer of the carotid artery bifurcation are of different origin. As in the bifurcation no splitter plate is present, essentially no vorticity can be generated in the shear layer itself. However, also in this case a strongly non-homogeneous vorticity distribution is present due to boundary layer separation and due to the secondary flow field. The secondary flow field, which is most pronounced during systolic deceleration and in the initial phase of diastole, can transport vorticity from the side walls into the shear layer. Also the time-dependent features of the global velocity field can cause redistribution of the vorticity.

Following the above, it is questionable whether the model study on the 2D shear layer is relevant for the study of flow disturbances in the carotid artery bifurcation. In the bifurcation (*i*) no splitter plate is present, (*ii*) due to the complexity of the geometry the flow is not parallel and strongly dependent on the axial position and (*iii*) the flow is essentially three-dimensional with a strong secondary velocity field. Nevertheless, some interesting similarities between the stability of the 2D channel flow and the 3D carotid

flow (analyzed in the plane of symmetry) can be seen. First, in both cases the generation of quite similar large scale vortices takes place during systolic deceleration (compare the results from figures 4.7 and 6.8). Secondly, in both situations the vortices move downstream with a phase velocity with is approximately equal to the instantaneous local fluid velocity.

LDA versus FEM results   The stability of the shear layer in 2D channel flow is studied by performing both LDA experiments and FEM computations. It was shown that there is a qualitative rather good agreement between the two methods, both predicting the occurrence of vortices with equal wavelengths and phase velocities in the shear layer during systolic deceleration and during diastole. However, in section 6.4.2 it was shown that differences between the two methods occur at sites, downstream Y_{12}. The vortex structures, measured by means of LDA become indistinct or even disappear, whereas the numerical method still predicts clearly visible vortices at these sites. This is also demonstrated in figure 6.10, where the experimental and numerical axial velocities are plotted for two points at sites Y_4 and Y_{16} in the lower half of the channel ($y = -0.4H$). It can be seen that at site Y_4 the largest differences occur during systolic deceleration and the initial phase of diastole, but still for both methods the initial disturbance is clearly predicted. At site Y_{16} however, the numerical results show a very distinct oscillation in the axial velocity, whereas this oscillation in the experiments is not clear anymore. Moreover, the experimental standard deviations of the ensemble averaged profiles appear to be large at this site. Apparently the experimentally observed vortex structures reproduce worse for downstream sites. This can be explained as follows: the experimental inflow conditions show small differences between the individual flow pulses during the measurements. The instabilities in the 2D shear layer are very susceptible to these small differences and small phase errors in the onset of the disturbances are resulting. Thus, the ensemble averaging procedure causes the oscillations in the experiments to disappear.
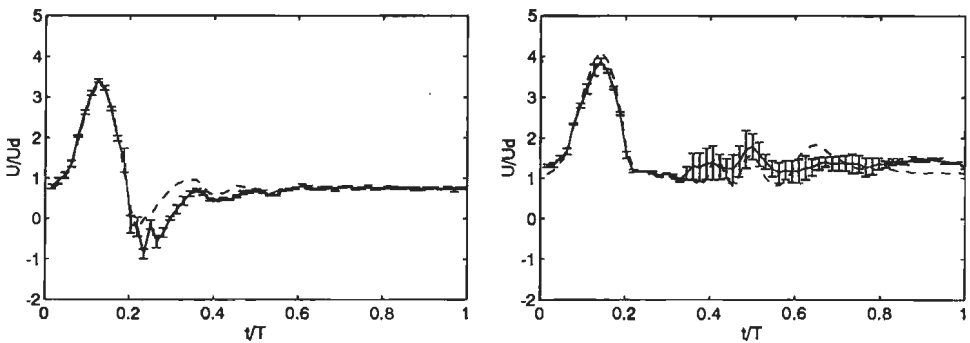
Figure 6.10: *Experimental (—) and numerical (- - -) axial velocities for two points at sites Y_4 and Y_{16} in the lower half of the channel at $y = -0.4H$.*

Chapter 7

Parameters describing the influence of the 25% stenosis

7.1   Introduction

In chapters 2, 3 and 4 the results of the flow in 0% and 25% stenosed carotid artery bifurcations have been presented. It has been shown that the influence of the 25% stenosis involves a shift of the main flow towards the divider wall, a different unsteady shear layer behavior and a decrease of the axial velocities in the reversed flow region. In this chapter methods are investigated that can trace and quantify these differences in order to obtain parameters that describe the influence of the stenosis. Since the LDA experiments predict the unsteady shear layer behavior more accurately than the computations (see also chapter 5), here only the results of the LDA experiments are considered. Firstly, different types of quantification methods are mentioned (section 7.2). Next the results are presented for: (i) the velocity moments derived from axial velocity profiles in the plane of symmetry (section 7.3), (ii) the size of the reversed flow region (section 7.4), (iii) a number of indices, used in clinical practice to detect stenotic plaques (section 7.5) and (iv) the Fourier transforms (section 7.6). Finally, a concluding discussion is given in section 7.7.

7.2   Quantification methods

The methods that can be used to quantify the differences between the flow in 0% and 25% stenosed bifurcations, can be subdivided into three categories: analysis in the spatial, temporal and frequency domain. Each category will briefly be discussed.

Analysis in the spatial domain.

Firstly, it is possible to analyze the velocity profiles by calculating the velocity moments. To characterize the flow in the carotid sinus, the moments of the axial velocity profiles along lines in the plane of symmetry are used. Olson (1971), who applied these quantities

to the flow in bends, determined the velocity moments as follows:

$$S(t) \;=\; \int\limits_{-1}^{1} |U(r,t)|\,dr, \tag{7.1}$$

$$\bar{r}(t) \;=\; \frac{1}{S(t)} \int\limits_{-1}^{1} r|U(r,t)|\,dr, \tag{7.2}$$

$$\sigma(t) \;=\; \sqrt{\frac{1}{S(t)} \int\limits_{-1}^{1} (r - \bar{r}(t))^2 |U(r,t)|\,dr}, \tag{7.3}$$

with r the dimensionless position. Olson (1971) derived these quantities from statistical probability distributions. Since he applied this to velocity profiles, the author considered the absolute value of the velocities $|U(r,t)|$ (Olson, 1971). Though the probability distribution can not simply be translated to the distribution of velocities in the profile, the interpretation of the moments is quite similar. The zeroth moment $S(t)$ is proportional to the mean value of the absolute velocity along the profile. The first moment $\bar{r}(t)$ represents the skewness or center of momentum of the profile and the second moment $\sigma(t)$ is a measure for the deviation from this. With respect to the intervals of integration the question arises whether the velocity moments must be derived from a dimensionless radius or not. Since the velocity moments are used to characterize the influence of a stenosis without having the possibility of comparing a non-stenosed and a stenosed case (in clinical situations), the dimensionless approach is the only way to calculate the moments.

The second way to study the influence of stenoses in the spatial domain is for example to determine the position of the shear layer, by calculating $\partial u_{ax}/\partial r$ as a function of radial position and time, or to determine the size of the reversed flow area in the plane of symmetry as a function of time.

In clinical practice also the shape of the velocity profiles is used to distinguish healthy from stenosed arteries, but in a more global way. Van Merode (1989) used a multi-gate pulsed Doppler system to measure velocity profiles as a function of time in the carotid artery bifurcation. Moreover, Van Merode extracted the on-line changes in arterial diameter during the cardiac cycle from these measurements, by estimating the width of the velocity profiles, giving information on the distensibility of the arterial wall.

Analysis in the temporal domain.

In the last decade much clinical research on ultrasound measurements in the carotid artery bifurcation has been done, using both continuous wave and pulsed Doppler ultrasound techniques. The continuous wave technique can be used to produce sonograms (i.e. the velocity distribution of particles moving through the sound beam as a function of time; in this technique the velocity information is independent of the distance to the transducer). With the development of (single-gate) pulsed Doppler systems it has become possible to position the scattering volume at a given distance from the transducer, thus determining

the mean velocity in a small sample volume as a function of time. With (multi-gate) pulsed Doppler systems it is even possible to record velocities at different sample volumes simultaneously, thus enabling the on-line measurement of velocity profiles as a function of time in vivo (see also van Merode, 1989). With these methods many ultrasound studies have been performed in healthy volunteers and patients suffering from carotid artery stenoses, concentrating on the differences between the non-stenosed and the stenosed cases. Many attempts have been made to quantify the shape of the velocity waveform originating from for example sonograms or the centerline velocity at stenosed sites. An overview of the most important methods, concentrating on particular aspects of the shape of the velocity waveform in the carotid artery bifurcation is given below.
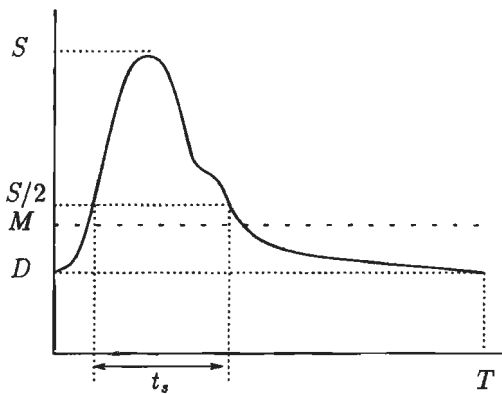
Figure 7.1: *Diagram illustrating the variables involved in the definitions of the pulsatility index, the height width index and the Pourcelot's resistance index (see text below). The vertical axis may represent the envelope of a sonogram, the centerline velocity or another quantity related to flow velocities.*

Maximum velocity. Johnston *et al.* (1982) analyzed the maximum velocity over a cross section of the vessel, since for moderate stenoses a reduction of the cross sectional area will lead to an increased maximum velocity. This method appears not to be suitable for the detection of stenoses with less than 40% area reduction (Jungquist *et al.*, 1989).

Pulsatility index PI. A widely used index is the pulsatility index $PI = (S - D)/M$, introduced in this form by Gosling and King (1974). Here, S and D represent the maximum and minimum values of the amplitude of the flow pulse during one cardiac cycle and M is the mean height of the waveform (see also figure 7.1). The PI appears to be influenced by many factors like proximal stenosis, distal stenosis and peripheral resistance (Evans *et al.*, 1980; Junger *et al.*, 1984).

Height width index HWI. Johnston *et al.* (1984) combined information of the pulsatility of the waveform and the time relationship, by the definition of the height width index $HWI = PI \cdot (T/t_s)$, where t_s represents the duration of the systolic peak measured between the half amplitude points (figure 7.1). The value of HWI decreases with increasing arterial stenoses, because waveforms distal to stenoses have relatively small pulsatile components and relatively wide systolic peaks.

Pourcelot's resistance index RI. Another widely used index of pulsatility is Pourcelot's resistance index (RI), which is defined as $RI = (S - D)/S$, with S and D as defined before. The index gives an indication of the circulatory resistance beyond the measurement point. Pourcelot (1976) used this index to detect waveform changes in internal carotid stenoses (larger than 60%).

Broadening indices. Many investigators use broadening indices, that do not concentrate on the shape of the velocity waveform, but on the distribution of velocities within the ultrasound beam. Sonograms recorded from normal vessels exhibit a clear window under the systolic peak, resulting from a relatively flat velocity profile at this time step. Diseased vessels show a degree of broadening in the velocity distribution of the velocities within the ultrasound beam, which is related to the degree of proximal stenosis (Reneman and Spencer, 1979). In literature many definitions of broadening indices were used with varying degree of success (Evans *et al.*, 1989).

Analysis in the frequency domain.

The most well-known technique to analyze a signal $u(t)$ in the frequency domain is the calculation of the Fourier transform $U(f)$

$$U(f) = \int_0^T u(t)e^{-2\pi i f t}dt. \tag{7.4}$$

From this the autopower spectrum $P_{uu}(f)$ can be calculated as follows

$$P_{uu}(f) = \frac{2}{T} \, |U(f)|^2. \tag{7.5}$$

In the present study analysis in the spatial domain (i.e. the determination of the velocity moments and the size of the reversed flow region), analysis in the temporal domain (i.e. the calculation of the pulsatility index PI, the height width index HWI and the resistance index RI) and analysis in the frequency domain (i.e. Fourier analysis) have been performed. In the following sections the results of these analyses will be presented.

7.3   Velocity moments

The axial velocity profiles in the plane of symmetry have been used to calculate the three velocity moments as defined in equations 7.1, 7.2 and 7.3. For each time step the zeroth,

first and second velocity moments are calculated and the results are presented in the left, center and right plots of figure 7.2 respectively. In the upper plots of figure 7.2 the situation in the common carotid is given. At this site the flow is still axisymmetric and the zeroth moment varies with the shape of the flow pulse. The first moment is nearly zero due to the nearly perfect (axi-)symmetry. The second moment shows a small enlargement during systole, that is caused by the flattening of the axial velocity profiles. As expected, for both models (0% and 25% stenosed) the results are almost identical at this site. Next, the moments at sites I_{00}, I_{05}, I_{10}, I_{15} and I_{20} will be considered (see also figure 7.2).

Zeroth velocity moment $S(t)$: For all sites the zeroth velocity moment $S(t)$ shows some kind of pulsatile behavior, in which the peaks coincide with peak-systole. However, the shapes of the curves in the internal carotid artery do not resemble the shape of the input flow pulse, due to the fact that the flow field is not axisymmetric anymore. During systole $S(t)$ is larger at site I_{10} for the 25% stenosed case, whereas at sites I_{15} and I_{20} it is smaller. The influence of the stenosis at these sites, results in enlarged axial velocities during systole at stenosed sites and decreased axial velocities at sites downstream the stenosis. During diastole $S(t)$ of the non-stenosed case is larger at site I_{05} than the one for the 25% stenosed case. This phenomenon originates from the negative velocities in the reversed flow region in the non-stenosed case (see also figure 4.7), which contributes to the zeroth velocity moment, since in the definition of $S(t)$ the absolute values of the axial velocities are considered (see also equation 7.1). Although there are some differences between the 0% and the 25% stenosed case, it should be noted that these differences are rather small.

First velocity moment $\bar{r}(t)$: The first velocity moment, representing the skewness of the profiles, are given in the center plots of figure 7.2. For all sites in the carotid interna, $\bar{r}(t)$ diminishes during systolic acceleration to relatively small values at peak-systole, indicating rather symmetric velocity profiles at that time (see also figure 4.7). During systolic deceleration $\bar{r}(t)$ increases again, due to the occurrence of the low velocity area near the non-divider side. In the initial phase of diastole significant differences between the non-stenosed and the stenosed case can be seen at sites I_{05}, I_{10} and I_{15}. The low values of $\bar{r}(t)$ in the non-stenosed case (see for example the result at site I_{10} at $t/T = 0.35$) can be explained from the occurrence of the large reversed flow region with negative velocities, resulting in a more or less anti-symmetric velocity profile. As in our definition of $\bar{r}$ the absolute values of the axial velocities are considered, the first moment of the velocity profile can not distinguish between symmetric and anti-symmetric profiles. In the stenosed case the area with negative velocities is much smaller and as a result the values of $\bar{r}$ are higher. In summary it can be said that the influence of the 25% stenosis on the first velocity moment is significant in the initial phase of diastole at sites I_{05}, I_{10} ($0.3 < t/T < 0.7$) and I_{15} ($0.25 < t/T < 0.5$).

Second velocity moment $\sigma(t)$: The second velocity moments given in the right-hand-side plots of figure 7.2, show a slight increase during systolic acceleration, due to the flattening of the velocity profiles and a decrease during systolic deceleration. During
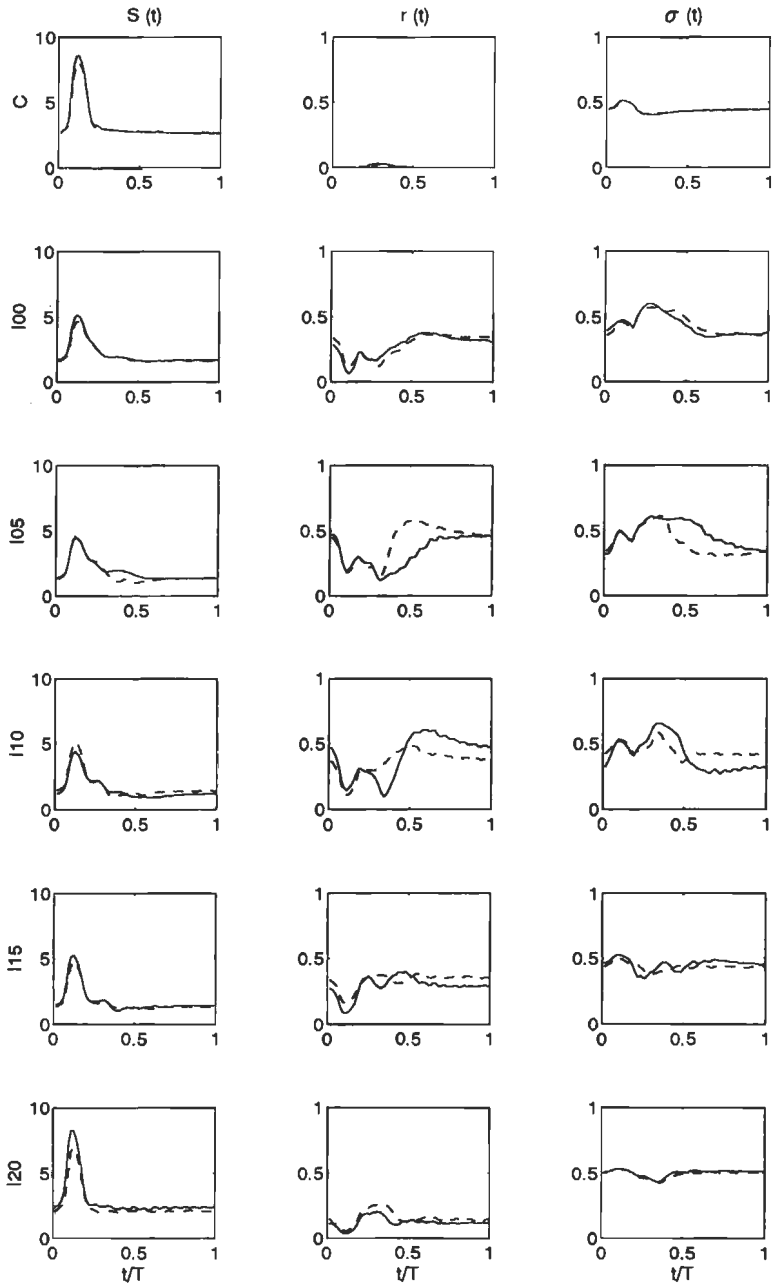
Figure 7.2: Zeroth $S(t)$ (left), first $\bar{r}(t)$ (center) and second $\sigma(t)$ (right) moment of the axial velocity profiles at different sites in the plane of symmetry in the non-stenosed (—) and the 25% stenosed (- -) model of the carotid artery bifurcation.

diastole the largest values of $\sigma(t)$ are reached (from $t/T = 0.25$ up until $t/T = 0.5$). The differences between the non-stenosed and the stenosed cases are maximal during diastole and involve a significant lower value of $\sigma(t)$ at site I_{05} and a slightly enlarged value of $\sigma(t)$ at site I_{10} for the 25% stenosed case.

The question may arise whether the velocity moments as used by Olson (1971) are most suitable for carotid artery flow. Since Olson uses the absolute values of the velocities and considerable negative velocities occur in the initial phase of diastole, the moments may be significantly influenced by this definition. Therefore, the following definition of the zeroth and first velocity moments seem to be more appropriate for this specific flow problem:

$$S'(t) \;=\; \int_{-1}^{1} U(r,t)dr, \tag{7.6}$$

$$\bar{r}'(t) \;=\; \int_{-1}^{1} rU(r,t)dr, \tag{7.7}$$

In this definitions the first velocity moment $\bar{r}'(t)$ is not normalized with the zeroth moment $S'(t)$ as in equation 7.2, since $S'(t)$ may become zero in the present definition. The physical meaning of the second velocity moment becomes unclear in this case (note that $\sigma'(t)$ may become imaginary). The moments $S'(t)$ and $\bar{r}'(t)$ have been evaluated for the 0% and 25% stenosed bifurcations, but no significant differences between the two cases appeared. But as could be expected from the discussion earlier in this section, the difference that occurred with the original definition (which was attributed to an earlier disappearance of negative velocities in the 25% stenosed case) was not found anymore.

7.4   Size of the reversed flow region

The size of the reversed flow region has been determined from the ensemble averaged axial velocities, as presented before in figure 4.7. In figure 7.3 the contours with zero velocity (i.e. the boundary of the reversed flow region) at sites I_{00}, I_{05}, I_{10} and I_{15} are presented for the non-stenosed (solid lines) and the 25% stenosed case (dash-dotted lines). From this figure it appears that hardly any influence of the 25% stenosis on the reversed flow area can be seen upstream the stenosis (site I_{00}). The local distortion at $r/R = -0.8$ and $t/T > 0.6$ for the non-stenosed case is caused by small inaccuracies in the LDA experiments at this site (see also figure 4.7). Downstream the stenosis (site I_{15}) a small influence of the 25% stenosis appears from the onset of the reversed flow region at an earlier phase of the flow cycle and a later disappearance of this region. The most significant influence of the 25% stenosis can be found at stenosed sites (i.e. I_{05} and I_{10}). Here, the presence of the stenosis diminishes both the radial extent (sites I_{05} and I_{10}) and the temporal extent (site I_{10}) of the reversed flow region.
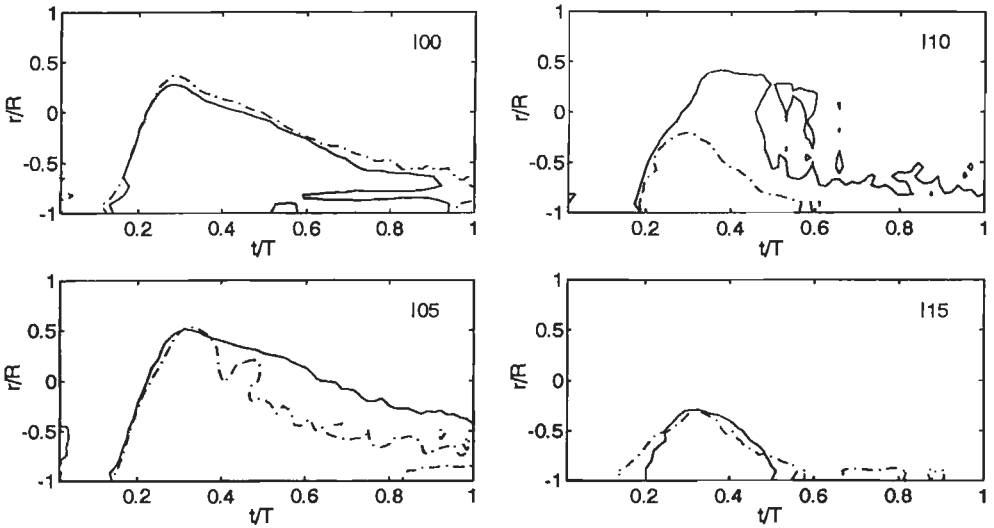
Figure 7.3: *Size of the reversed flow region as a function of time and radial position at sites I_{00}, I_{05}, I_{10} and I_{15} of the non-stenosed (—) and the 25% stenosed bifurcation (- · -).*

In conclusion it can be noted that the influence of the 25% stenosis on the size of the reversed flow region, can mainly be found at stenosed sites (I_{05} and I_{10}). It is expressed in a decrease of the reversed flow region in both radial and temporal extent.

7.5   Indices in the temporal domain

As a starting point for the calculation of the different indices, the mean velocity as a function of time along lines in the plane of symmetry has been determined for the different sites. Next the pulsatility index PI, the height width index HWI and the Pourcelot's resistance index RI, as defined in section 7.2, have been determined from this cross-sectional mean axial velocities. The results are presented in figure 7.4. From the left-hand side plot it can be seen that the pulsatility index significantly decreases at stenosed sites (I_{05} and I_{10}), whereas downstream the stenosis (I_{15} and I_{20}) the stenotic influence is less noticeable. It should be noted that PI is also strongly dependent on the axial position in the carotid sinus. At the entrance of the internal carotid artery (site I_{00}), PI is slightly higher in the stenosed case compared to the non-stenosed case. Similar characteristics can be found for the height width index (center plot) and the resistance index (right plot of figure 7.4). The influence of the 25% stenosis seems to find most expression in the pulsatility index PI and the height width index HWI.
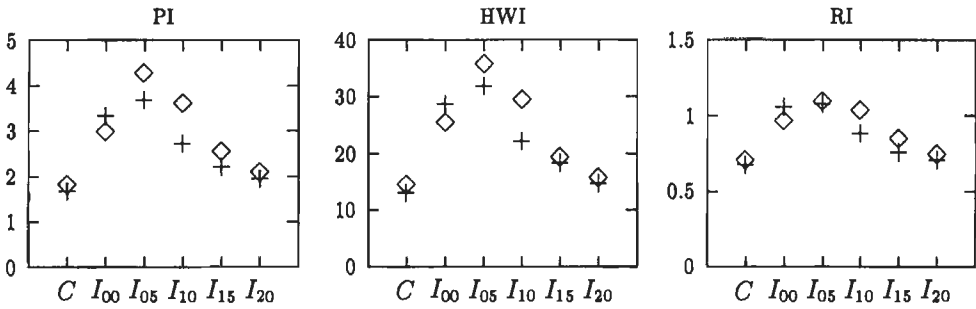
Figure 7.4: *Values of the pulsatility index (PI), height width index (HWI) and the Pourcelot's resistance index (RI) for the non-stenosed ($\diamond$) and the 25% stenosed ($+$) bifurcation at different sites, as determined from the mean cross-sectional velocities along the lines in the plane of symmetry from LDA experiments.*

7.6 Fourier analysis

The data of the ensemble averaged axial velocities in the plane of symmetry have been analyzed in the frequency domain. The frequency contents is calculated by applying a fast Fourier transform. This has been done for each measuring point along lines in the plane of symmetry at sites C, I_{00}, I_{05}, I_{10}, I_{15} and I_{20}. In figure 7.5 the results of the Fourier transforms are given as a function of the dimensionless position r/R and the dimensionless frequency f/f_0 (also referred to as harmonic). Here, f_0 represents the fundamental harmonic of the flow pulse, based on the period time T. The upper plots of figure 7.5 represent the Fourier spectra for the measuring points at site C in the communis. As expected, the stationary components ($f/f_0 = 0$) show that the mean velocity in time varies nearly parabolical with position r/R. The higher harmonics on the contrary appear to be nearly equally present for each radial position, except at near wall sites. As expected, for the sites in the carotid sinus the stationary components show higher values near the divider wall than near the non-divider wall. In the Fourier spectra at sites I_{00}, I_{05}, I_{10}, I_{15} and I_{20} roughly three regions can be discerned.

- A region corresponding with the low velocity region near the non-divider wall ($-1 < r/R < 0.5$). The stationary component is relatively low in this region. The shape of the Fourier spectra for the higher harmonics is similar to the spectra in the common carotid artery. As far as the influence of the 25% stenosis is concerned, no significant influence is found in the Fourier spectra in the low velocity region.

- The shear layer region ($r/R \approx 0.5$), coinciding with large radial gradients of the stationary components ($f/f_0 = 0$). In this region relative maxima in the Fourier spectra of the flow pulse appear. Considering the results of the non-stenosed case

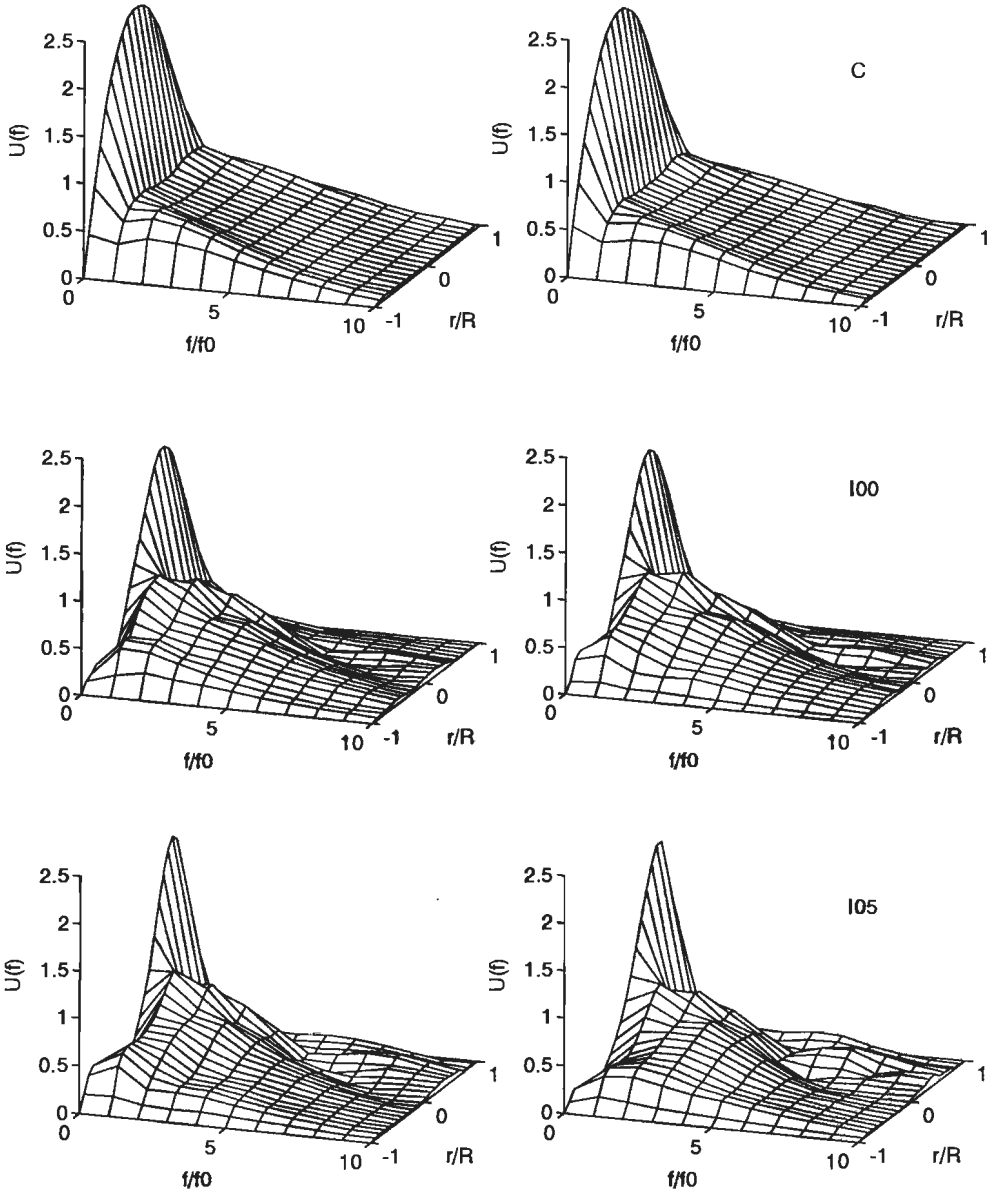**Figure 7.5:** *Fourier transforms of the ensemble averaged axial velocities in the non-stenosed (left) and the 25% stenosed (right) models of the carotid artery bifurcation at different sites.*
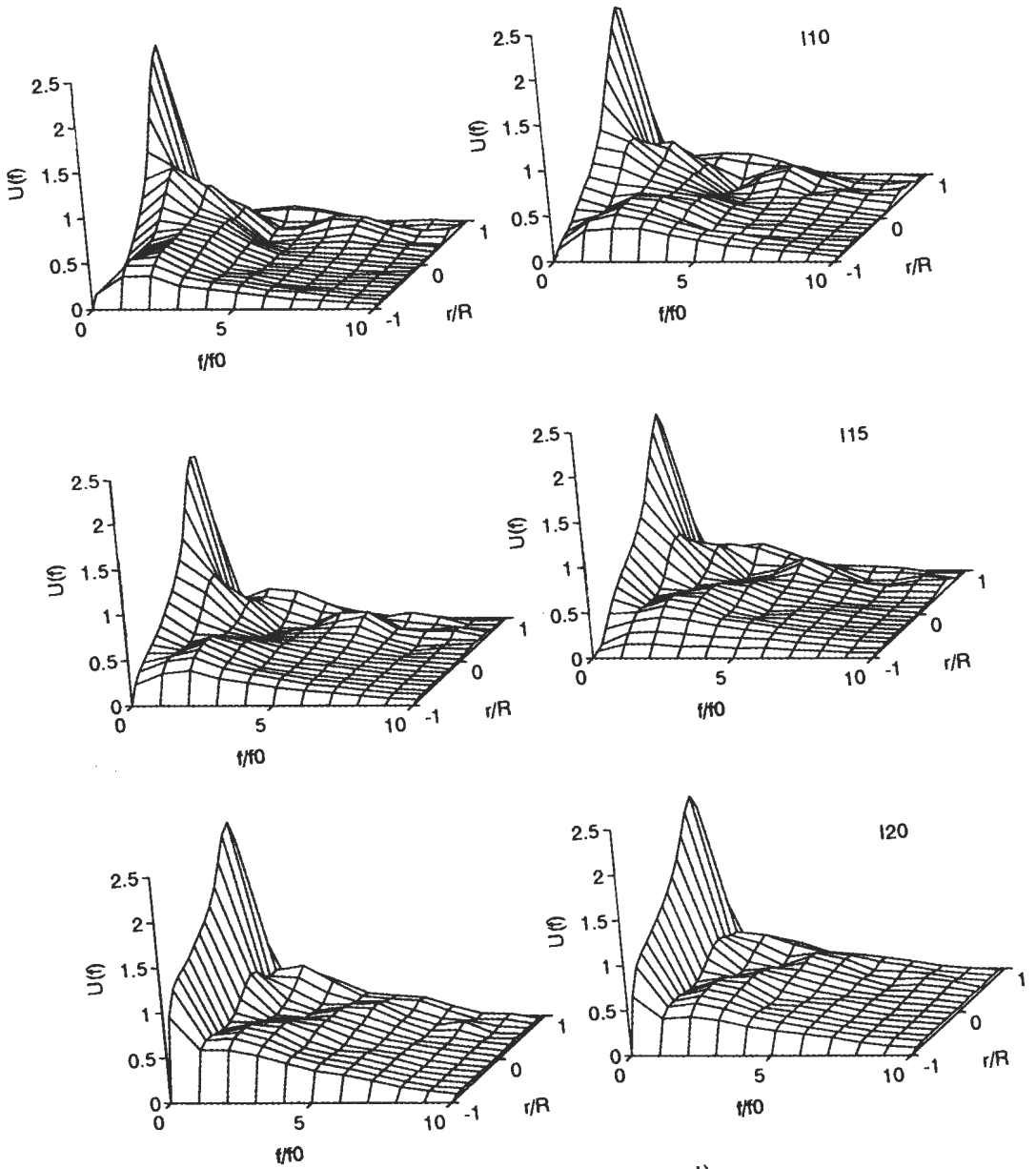
Figure 7.5: (Continued)

(left-hand-side plots of figure 7.5) this maximum can be discerned in the shear layer at site I_{00} at the 8th and 9th harmonic. Moving downstream the relative maximum seems to grow in amplitude and shifts to lower harmonics (7th and 8th harmonic at site I_{05}, 6th and 7th harmonic at site I_{10} and 5th and 6th harmonic at site I_{15}).
In the 25% stenosed case similar features occur in the shear layer. The relative maxima in the Fourier spectrum seem to have slightly shifted to lower harmonics, compared to the non-stenosed case.

- The region corresponding to the high velocity region ($r/R > 0.5$). The stationary components of the Fourier spectrum are maximal at these radial positions. In this region no significant relative maximum in higher harmonics or any other influence of the 25% stenosis can be seen anymore.

Although the influences of the 25% stenosis are small, it can be concluded that the main influence on the Fourier spectra can be found in the shear layer region. The relative maximum in the higher harmonics seems to shift slightly to lower values of f/f_0 for the 25% stenosed case.

7.7   Concluding discussion

In this chapter the ensemble averaged axial velocities along lines in the plane of symmetry have been analyzed. Several methods have been evaluated in order to trace and quantify the differences between the non-stenosed and the 25% stenosed case.

Velocity moments. The 25% stenosis mainly influences the first $\bar{r}(t)$ and second $\sigma(t)$ velocity moments at sites I_{05} and I_{10} in the initial phase of diastole. It should be noted, that this influence is in the same order of magnitude than the dependency of the velocity moments on the axial position. With respect to the detection of minor stenoses, this axial dependency must always be regarded (see also section 8.3).

Size of reversed flow region. The influence of the 25% stenosis on the size of the reversed flow region can mainly be found at sites (I_{05} and I_{10}), expressing a decreased reversed flow region in both radial and temporal extent. Since the radial and temporal gradients of the axial velocities are small at the boundary of the reversed flow region (i.e. the zero velocity contour), this method is very sensitive for (experimental) inaccuracies, which diminishes the diagnostic value of this parameter.

Indices. Calculation of the pulsatility index, the height width index and the Pourcelot's resistance index show a significant decrease of the indices at stenosed sites, whereas the stenotic influence is less noticeable at downstream sites. Since the influence of the stenosis on the indices is in the same order of magnitude as the influence of the axial position, the use of these parameters for detecting minor stenoses is strongly hampered.

Fourier analysis. Analysis in the frequency domain (calculation of Fourier spectra) shows a small influence of the 25% stenosis in the region of the shear layer, where a relative maximum in the spectrum of the higher harmonics occurs. Compared to the non-stenosed case, this maximum shifts to lower harmonics in the 25% stenosed case. However, the frequency at which this relative maximum occurs, appears to depend on the axial position in the carotid sinus, diminishing the diagnostic value of this parameter as stated before.

Considering the applicability of the methods, it should be noted that, though several influences of the 25% stenosis have been found, the influence of the stenosis is very small and has restrictions as mentioned above. In the next chapter both the influence of geometrical and initial conditions on the results, obtained with the methods described in this chapter, will be discussed. Moreover, remarks on the feasibility of clinical application will be made.

Chapter 8

Discussion, conclusions and recommendations

8.1 Introduction

In the present study the influence of a 25% stenosis on the flow field in the carotid artery bifurcation has been investigated. From the LDA experiments described in chapter 4, it appeared that the influence of the stenosis on the velocity field mainly involves two aspects: (i) a disturbance with enlarged axial velocities appears in the stenosed model in the region with flow reversal in the initial phase of diastole and (ii) a more pronounced oscillation of the axial flow field can be discerned near the shear layer in the stenosed bifurcation. In chapter 7 parameters have been evaluated that can trace and quantify this influence. It was found that the influence of the 25% stenosis is reflected in the following parameters.

Velocity moments: the 25% stenosis influences the first $\bar{r}(t)$ and second $\sigma(t)$ velocity moments at sites I_{05} and I_{10} in the initial phase of diastole.

Size of the reversed flow region: the size of the reversed flow region is significantly decreased in radial and temporal extent at stenosed sites (I_{05} and I_{10}). However, this parameter will not be considered anymore, since it is very sensitive for small inaccuracies as discussed in chapter 7.

Pulsatility Index and Height Width Index: a significant decrease of the pulsatility index and the height width index is found at stenosed sites (I_{05} and I_{10}).

Fourier spectrum: a small influence of the 25% stenosis is found in the region of the shear layer, expressed in slightly lower frequencies of the amplified higher harmonics.

These results were obtained from well-controlled experiments, in which only the geometrical influence of the stenosis was varied. The parameters, that have been evaluated to trace the influence of the stenosis, will have only a clinical relevance if they are not very sensitive for other geometrical variations than those of stenoses or variations of the

flow conditions, which show large inter-individual differences in clinical practice. Since the hydrogen-bubble visualizations from chapter 2 have shown that inflow conditions have a significant influence on the flow phenomena in the carotid artery bifurcation, in section 8.2 special attention is paid to the influence of the shape of the flow pulse and the flow division ratio on the detection parameters.

In order to give an indication of the influence of the degree of the stenosis on the flow phenomena, in section 8.3 the flow field in a 50% stenosed bifurcation is investigated by computing the axial and secondary velocities. It might be expected that the influence of such a larger stenosis is more pronounced or that even other physical phenomena become important. Finally, in section 8.4 general conclusions are drawn and recommendations for future investigations are given.

8.2   Discussion on the influence of inflow conditions

In order to investigate the influence of the inflow conditions, in addition to the LDA results for the non-stenosed and the 25% stenosed bifurcation (chapters 4 and 7), in this section LDA experiments are presented for minor variations of the inflow conditions. These variations have been performed in the non-stenosed model of the bifurcation. With respect to the reference case ($T_a/T = T_d/T = 0.1$, $T_p/T = 0$, $Re = 270-1000$, $\alpha = 6$ and $\gamma = 0.35$), the shape of the flow pulse and flow division ratio are varied. Four situations have been evaluated:

(i) the 0% stenosed bifurcation with reference inflow conditions (see chapters 4 and 7);

(ii) the 25% stenosed bifurcation with reference inflow conditions (see chapters 4 and 7);

(iii) the 0% stenosed bifurcation with slowly decelerating flow during systole ($T_d/T = 0.2$); this choice is motivated by the fact that recent in vivo pulsed Doppler ultrasound measurements (Brands, 1993) indicate that the flow decelerates more slowly compared to the flow pulse of Ku *et al.* (1985b).

(iv) the 0% stenosed bifurcation with an enlarged flow division ratio ($\gamma = 0.45$); this seems to be a physiological relevant flow division ratio, since according to measurements of Ku *et al.* (1985b) the flow pulse varies in time and reaches its maximum value $\gamma = 0.45$ at peak-systole.

The parameters from chapter 7, that are also summarized in section 8.1, have been evaluated for these four situations. The results are discussed below.

Velocity moments.   In figure 8.1 the first $\bar{r}(t)$ and second $\sigma(t)$ velocity moments at sites I_{05} and I_{10} as a function of time are presented for the four cases as mentioned above. It is evident that the first moment $\bar{r}(t)$ for the 25% stenosed bifurcation significantly deviates from the non-stenosed geometry with the three different inflow conditions. At site I_{05} $\bar{r}(t)$ is significantly higher between $t/T = 0.35$ and $t/T = 0.8$ for the 25% stenosed case,
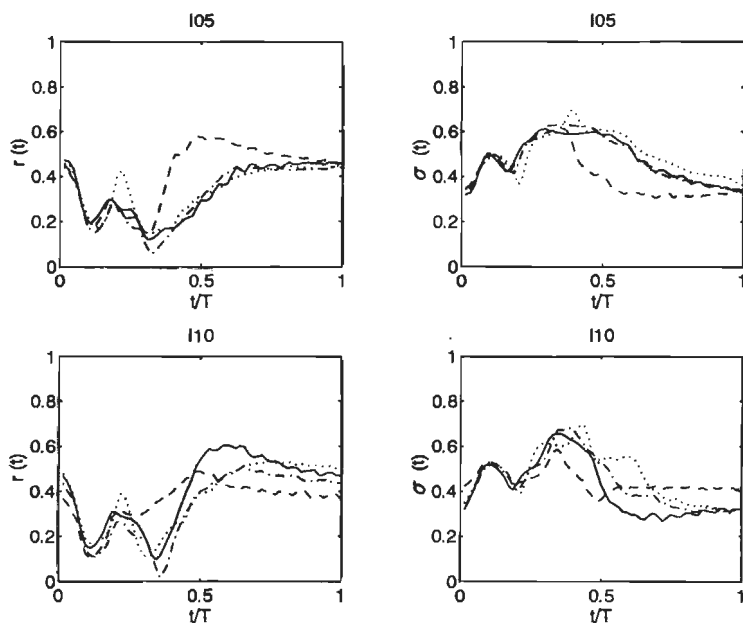
Figure 8.1: *Plots of the first $\bar{r}(t)$ (left) and second $\sigma(t)$ (right) velocity moments at sites I_{05} (upper) and I_{10} (lower) as a function of time for the different cases: 0% stenosed with reference inflow conditions (—), 25% stenosed with reference inflow conditions (− −), 0% stenosed with $T_d/T = 0.2$ (· · ·) and 0% stenosed with $\gamma = 0.45$ (− · −).*

whereas at site I_{10} this occurs in a smaller period ($0.35 < t/T < 0.45$).

The influence of the 25% stenosis on the second velocity moment $\sigma(t)$ is also significant at identical phases of the flow pulse, resulting in a large decrease of $\sigma(t)$ at site I_{05} and a small decrease at site I_{10}.

As discussed in chapter 7 the influence of the 25% stenosis on $\bar{r}(t)$ and $\sigma(t)$ originates from the less negative axial velocities in the reversed flow region of the 25% stenosed model. Though a significant deviation is found on $\bar{r}(t)$ and $\sigma(t)$ in the present study, the clinical applicability remains somewhat questionable for two reasons. Firstly, the shape of the carotid artery bifurcation, that was chosen according to results of Bharadvaj, shows a significant inter-individual variation (Bharadvaj *et al.*, 1982a). As a result velocity moments from a healthy bifurcation with a smaller divergence angle in the carotid sinus, will also show results that are similar to a stenosed bifurcation. Secondly, in the literature survey from section 1.2 it was shown that wall distensibility is expected to decrease the reversed flow region in size and velocity. This would result in a similar effect on the velocity moments as the influence of the 25% stenosis. Therefore additional research is needed to study the robustness of the velocity moments with respect to the factors, mentioned above.
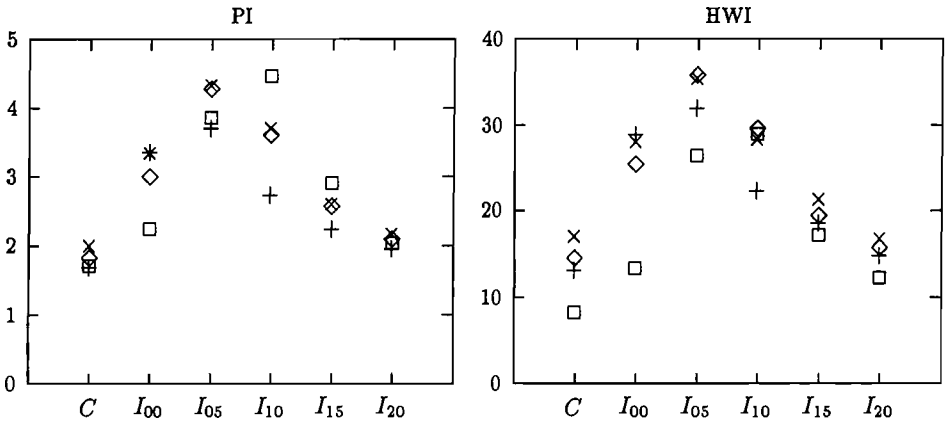
Figure 8.2: *Plots of PI (left) and HWI (right) at the different sites for the cases: 0% stenosed with reference inflow conditions ($\Diamond$), 25% stenosed with reference inflow conditions (+), 0% stenosed with $T_d/T = 0.2$ ($\Box$) and 0% stenosed with $\gamma = 0.45$ ($\times$).*

Pulsatility Index and Height Width index. The results of the Pulsatility Index (PI) and the Height Width Index (HWI) for the four different cases are presented in figure 8.2. For all four cases, PI and HWI vary with position in the internal carotid artery qualitatively in a similar way. Locally large differences are found. In particular at site I_{10} both PI and HWI differ significantly for the 25% stenosed bifurcation compared to the other cases, though PI still appears to be influenced by the inflow conditions at this site. This would suggest that at site I_{10} HWI might be a useful detection parameter, without being too sensitive for variation of the inflow conditions (reflected by the coinciding values of the indices for the 0% stenosed bifurcation). However, since the effect is very local and can only found at position I_{10}, it requires a very high spatial resolution of the detection technique, which will hamper the application of this detection parameter in practice. Moreover it can be expected that other factors, and especially the parameters that are related with wave propagation phenomena like the wall distensibility, will influence the observations too. Although the value of the Pulsatility Index and the Height Width Index for flows in distensible carotid artery bifurcations remains still an open question, from this study it must be concluded that these indices seem not to be suitable for the detection of minor stenoses.

Fourier spectrum. In figure 8.3 the results for the Fourier spectra at sites I_{05}, I_{10} and I_{15} are plotted in case of the non-stenosed bifurcation with two different inflow conditions: $T_d/T = 0.2$ (left) and $\gamma = 0.45$ (right). As expected, the Fourier spectra of the flow pulse with $T_d/T = 0.2$ has a larger stationary component, due to the enlarged mass flow during the flow cycle. Moreover, in this case the lower harmonics are more pronounced than the

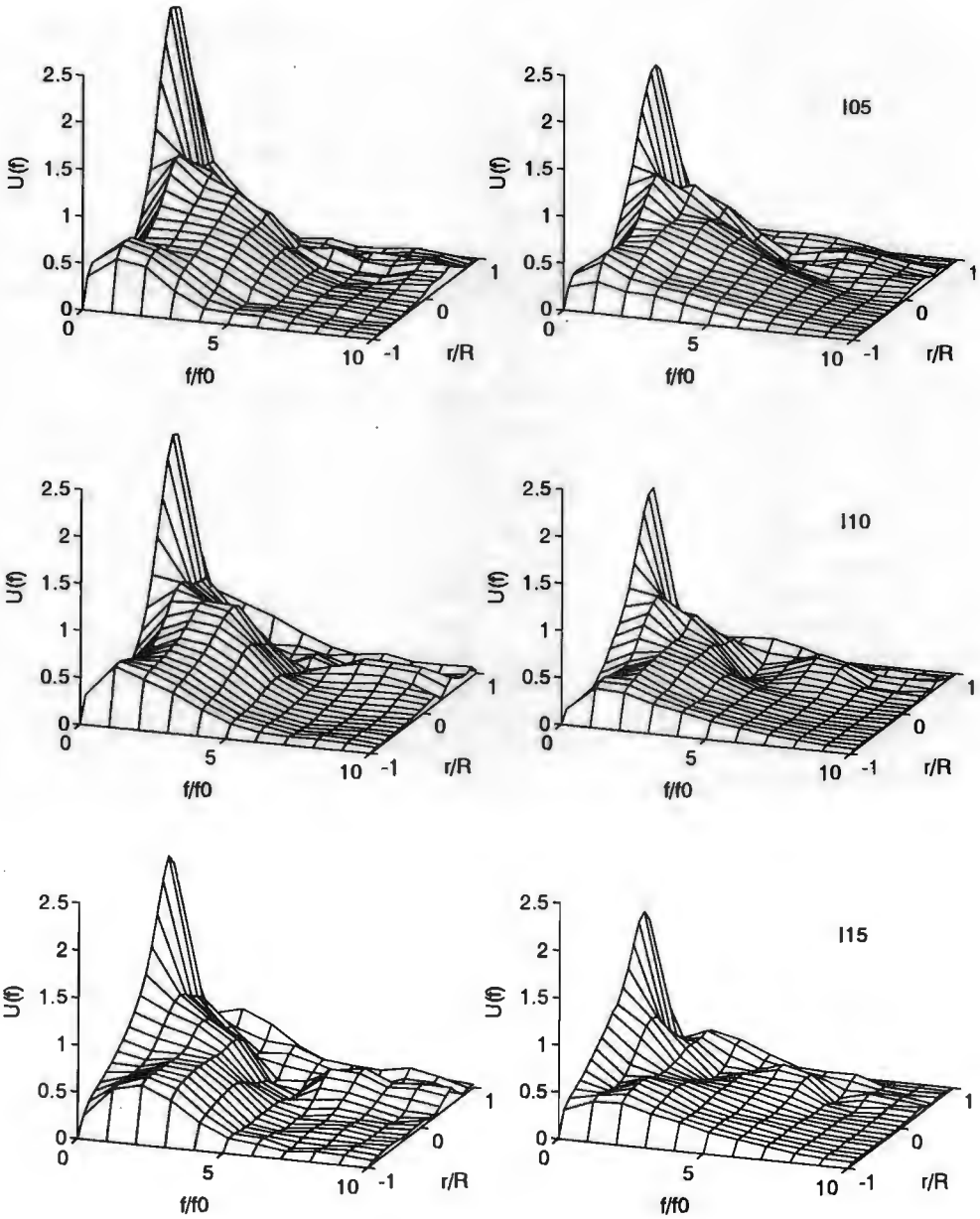**Figure 8.3:** *Plots of the Fourier spectra at sites I_{05} (upper), I_{10} (center) and I_{15} (lower) for the 0% stenosed bifurcation with $T_d/T = 0.2$ (left) and 0% stenosed with $\gamma = 0.45$ (right); compare this figure with figure 7.5.*

higher harmonics compared to the non-stenosed reference situation, due to the smaller temporal gradients during systolic deceleration for the flow pulse with $T_d/T = 0.2$. A comparison of figures 8.3 and 7.5 reveals that the position of the relative maximum in the spectrum in the shear layer region (near $r/R = 0.5$) as described in chapter 7, is strongly dependent on the inflow conditions, since the Fourier components in the shear layer are not only influenced by the presence of the stenosis but also by the inflow conditions. Thus, from this study it must be concluded that the Fourier analysis of the axial velocities does not lead to a useful detection parameter.

8.3   Discussion on the influence of the degree of the stenosis

In the previous section the influence of inflow conditions on detection parameters has been analyzed in a 0% stenosed bifurcation compared to the influence of a 25% stenosis. The first and second velocity moments at stenosed sites (I_{05} and I_{10}) appeared to be the only possible useful parameters, although the influence of model simplifications (see chapter 1) has not been considered yet. In general it can be concluded that detection of a 25% stenosis is not obvious, even for the well-controlled conditions and the accurate measuring method, as used in this study. To investigate whether this also holds for more severe stenoses, some attention will now be paid to a 50% stenosed carotid artery bifurcation. It is expected that the influence of such a larger stenosis is more pronounced, or that even other physical phenomena (such as vortex shedding from the rear end of the stenosis) might become important. In this section a tentative analysis is presented of pulsatile, three-dimensional flow in the carotid artery bifurcation with a 50% stenosis, by means of the computational method described in chapter 3.

The results for the 50% stenosed bifurcation are presented in figure 8.5 and can be compared with the results in chapter 3 (figures 3.5 and 3.6). Globally the effect of the 50% stenosis is similar to the effect of the 25% stenosis, but it is more pronounced. Some striking differences are found at stenosed sites (I_{10} and I_{15}):

- At site I_{10} the region with negative axial velocities is smaller in case of the 50% stenosis at end-systole ($t/T = 0.2$) and at $t/T = 0.25$. It also appears that much smaller secondary velocities are found in this case. Both effects are due to the stronger tapering of the wall of the internal carotid artery in case of the 50% stenosis. Furthermore, the ring-shaped region where the highest axial velocities occur is less pronounced in the 50% stenosed bifurcation.

- At site I_{15} a small reversed flow region is present in the 50% stenosed case at peak-systole ($t/T = 0.1$) and at end-systole ($t/T = 0.2$), which is not present in case of the 25% stenosis. Additionally, at end-systole ($t/T = 0.2$) a smaller reversed flow region is found in the 50% stenosed case with velocities that are less negative.
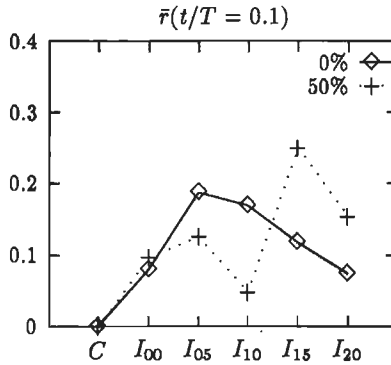
$$\bar{r}(t/T = 0.1)$$

Figure 8.4: *First velocity moment at peak-systole $\bar{r}(t/T = 0.1)$, determined from the computational results of the 0% and the 50% stenosed bifurcations.*

Next the first velocity moment $\bar{r}(t)$, being a possibly useful detection parameter, is considered. It is expected that the 50% stenosis shows a similar influence on $\bar{r}(t)$ during diastole as the 25% stenosis, but also that the effect is more pronounced. New effects on the first moment $\bar{r}(t)$ appear directly upstream and downstream the stenosis. Consider the first velocity moment at peak-systole $\bar{r}(t/T = 0.1)$ for the non-stenosed and the 50% stenosed bifurcation as a function of the axial position in the internal carotid artery (see figure 8.4). The computational results may be used for this purpose, since in chapter 5 it was shown that the computational results are in reasonably good agreement with the LDA results at peak-systole. Starting the axial scan in the common carotid artery, the $\bar{r}(t/T = 0.1)$ is nearly zero, due to the symmetry of the velocity profiles. Entering the internal carotid artery (site I_{00}), the first velocity moment at peak-systole increases, but still remains rather small. Moving downstream in the non-stenosed model $\bar{r}(t/T = 0.1)$ first increases up to site I_{05} and then it decreases again. On the contrary for the 50% stenosed case first a significant decrease occurs at site I_{10}, due to the flattened velocity profiles at occluded sites (see also figure 8.4). Next distal to the stenosis (site I_{15}) a sudden increase of the skewness $\bar{r}(t/T = 0.1)$ is present, since small negative velocities occur in a small separation area downstream the stenosis and high velocities are present near the divider wall (compare the situations for $t/T = 0.1$ and site I_{15} in figure 3.5 and 8.4). Moving further downstream the velocity profiles soon become rather flat again, due to the tapering of the interna and as a result the skewness $\bar{r}(t/T = 0.1)$ decreases. Increasing the degree of stenosis is expected to increase these effects furthermore.
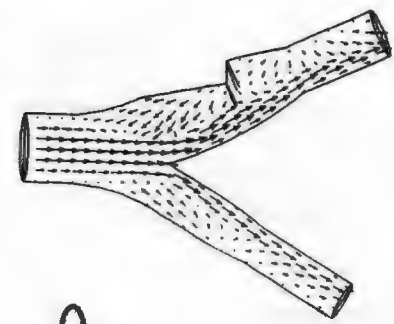
Figure 8.5: (Next pages) *Computational results of the 3D time-dependent flow field for the 50% stenosed bifurcation.*
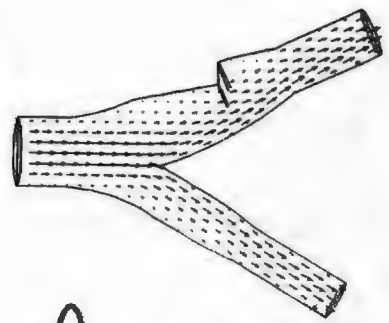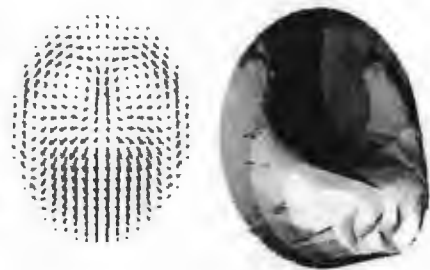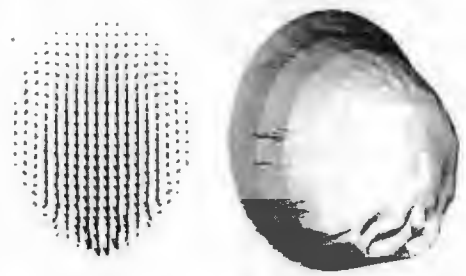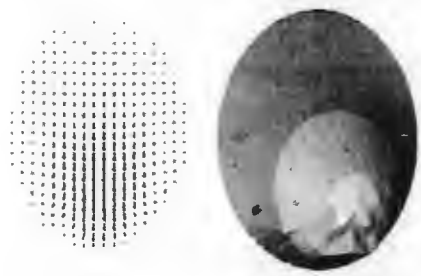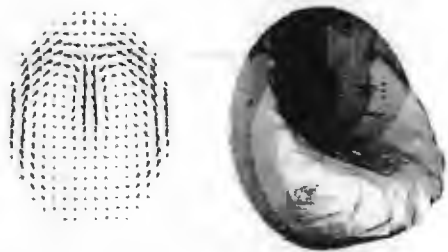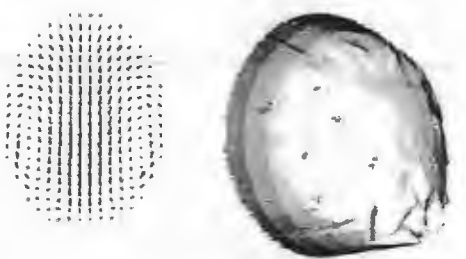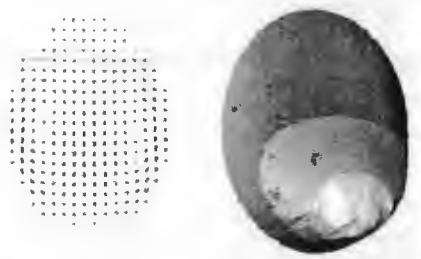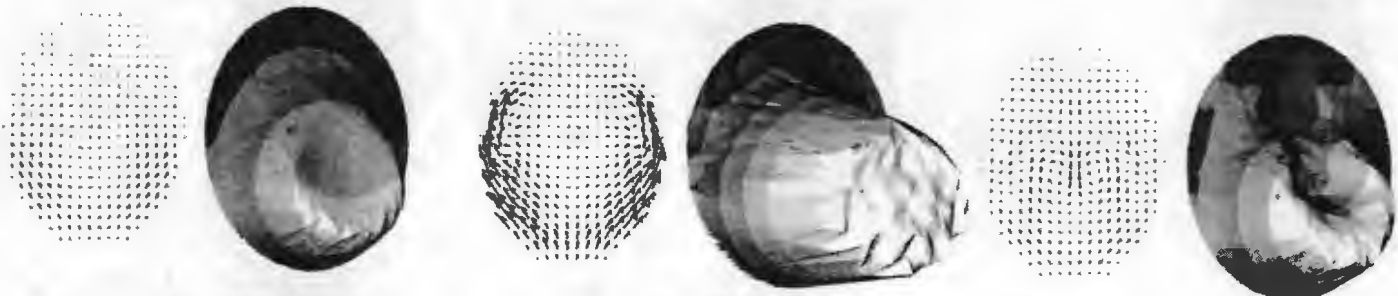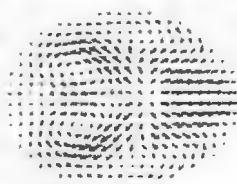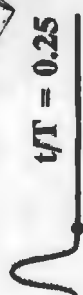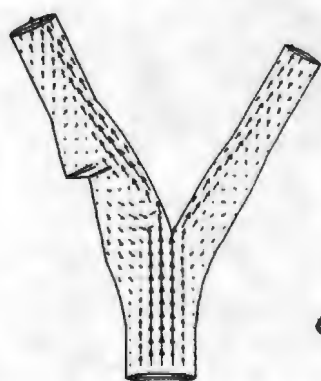
$t/T = 0.0$ $t/T = 0.1$ $t/T = 0.2$
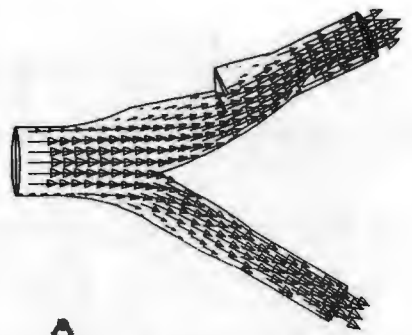
I_{00}

I_{05}

I_{10}

I_{15}

I_{20}
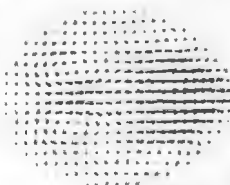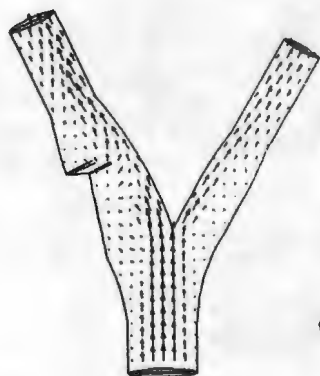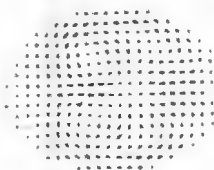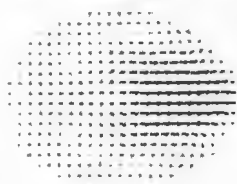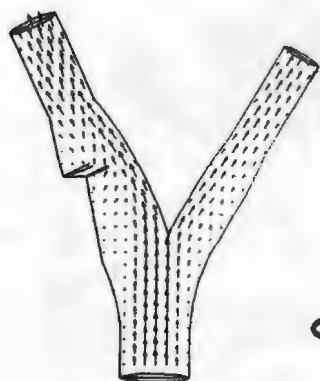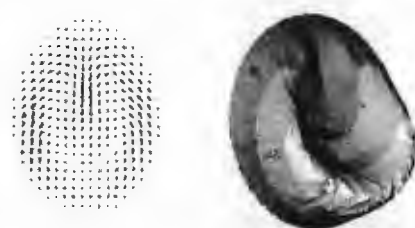
I_{10}
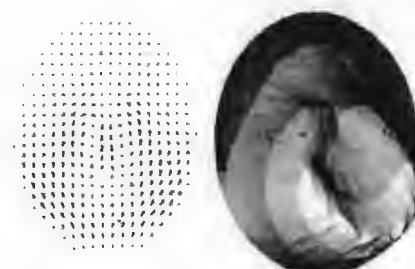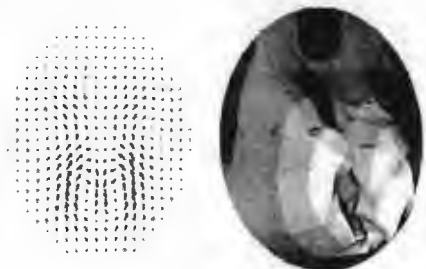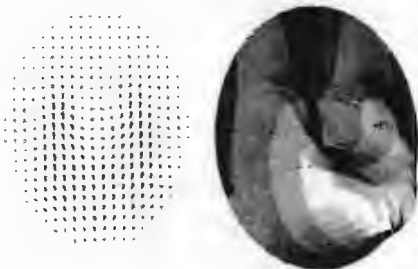
I_{15}
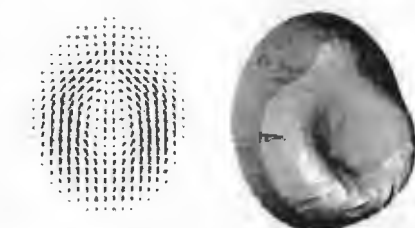
I_{20}

In conclusion: the first velocity moment at peak-systole $\bar{r}(peak\text{-}syst.)$ might be a useful parameter for the detection of moderate carotid stenoses (50% area reduction). A decrease followed by a sudden increase of $\bar{r}(peak\text{-}syst.)$ seems to mark the presence of a stenosis. Since this approach only considers relative changes in the first velocity moment, it is expected to be rather insensible for inter-individual differences, thus subordinating the problem of inter-individuality as much as possible. It also requires less exact knowledge of the position of the measuring volume. Nevertheless, future research on the robustness of this parameter for variation of the bifurcation angle, the shape of carotid sinus and stenosis, the wall distensibility and the non-Newtonian behavior, will still be needed.

8.4   Conclusions and recommendations

In this section first the accomplishments of the research presented in this thesis are discussed and next some ideas for future research are given. The main objective of this thesis is to investigate the influence of minor stenoses (with an area reduction of 25%) on the flow field in the carotid artery bifurcation and to search for parameters that can be used to detect these minor stenoses. Before the results are discussed with respect to this objective, first the most important facts of the previous chapters are summarized.

In chapter 1 it has been argued that at this stage of the study a simplified model of the carotid artery bifurcation was used with rigid walls and a Newtonian fluid. A typical geometry of the carotid artery bifurcation, based upon data from Bharadvaj *et al.* (1982a) was chosen.

In chapter 2 the hydrogen-bubble visualizations showed that shortly after the onset of diastole vortex formation occurs in a shear layer, i.e. the interface between a region with low shear rates at the non-divider wall and a region with high shear rates near the divider wall. These experiments demonstrated that, though the 25% stenosis only slightly influences the flow phenomena, the most striking influences are found in the stability of the shear layer. In this chapter it was also shown that relatively small changes in the inflow conditions influence the stability of the shear layer significantly. The hydrogen-bubble experiments also justified the use of a plane of symmetry in the finite elements computations from chapter 3, which reduced the number of unknowns considerably.

The computational results of the 0% and 25% stenosed models of the carotid artery bifurcation (chapter 3) showed that a very complex three-dimensional time-dependent flow field is present in the bifurcation, where both the axial and secondary flow fields play an important role. The following features occur: (*i*) during systolic acceleration the region with reversed axial flow is 'washed away' (i.e. no negative axial velocities are found near the non-divider wall); (*ii*) a region with reversed axial flow develops during systolic deceleration, reaching its largest dimensions at the onset of diastole and (*iii*) during the second half of systolic deceleration and in the initial phase of diastole a significant secondary flow field is present in the bifurcation, resulting in an extension in circumferential direction of the region with high axial velocities. The most significant and interesting flow phenomena

can be found in the period starting from systolic deceleration up until $t/T = 0.4$. After that, a smooth transition to the end-diastolic situation occurs, pointing at the quasi-static behavior at that time. The influence of the 25% stenosis mainly involves three aspects: (i) a decrease of the reversed axial velocity area at stenosed sites in the initial phase of diastole; (ii) an increase of the reversed axial velocity area downstream the stenosis, coinciding with the shift of the main flow towards the divider wall and (iii) in the stenosed case an increase of the near wall secondary velocities. Since the computational accuracy might not be sufficient to resolve all physical phenomena in detail, extension of this analysis with quantitative and accurate experiments is indispensable.

The laser Doppler method has been used to gain accurate time-dependent measurements of the axial and secondary velocity fields (chapter 4). The influence of the stenosis appears to involve two aspects: (i) the presence of a disturbance with elevated velocities in the region with flow reversal in the initial phase of diastole and (ii) more pronounced oscillations in the shear layer with different frequencies.

A comparison of the numerical results with LDA measurements has been discussed in chapter 5. Globally good agreement was found, but during systolic deceleration and the first part of diastole significant differences were found in the carotid sinus. The time scale of the computed unsteady shear layer behavior appeared to be smaller than the one from the experiments. Although the LDA experiments also suffer from experimental inaccuracies (see section 4.4), these differences are mainly ascribed to computational inaccuracies, due to the limitations of the finite element method as used in chapter 3.

In chapter 7 the LDA data were used to search for parameters, that are able to trace minor stenoses. Several detection parameters were evaluated. Together with the study on the influence of inflow conditions (chapter 8), the only promising detection parameters appear to be the first and second velocity moments at stenosed sites.

The unsteady shear layer behavior has been studied in a simplified geometry, represented by a 2D rectangular channel (chapter 6). It was shown that unsteady vortex shedding occurs in the 2D shear layer during systolic deceleration and in the initial phase of diastole and that the vortices move downstream with the instantaneous local fluid velocity, resembling the unsteady flow phenomena in the shear layer of the carotid artery bifurcation. Nevertheless, this 2D model situation may not simply be mapped on the complex 3D flow case of the carotid artery bifurcation. But still this model study has provided useful knowledge on unsteady shear layer behavior.

Finally, an evaluation of the study as presented in this thesis, is made next: a retrospective on the objectives, the course of the study, the conclusions and recommendations for future research. In the introduction an ambitious objective has been posed: investigating the possibility to detect minor stenoses from information on the velocity field in space and time. With the acceptable assumptions of rigid walls and Newtonian fluid behavior at this stage of the study, the following course has been pursued. (i) Hydrogen-bubble visualizations have provided a qualitative and overall view of the interesting locations and phenomena in the three-dimensional time-dependent carotid artery flow. (ii) The finite

element method has acted as a computational model of the flow problem and offered the possibility of parameter variation with respect to the geometry and inflow conditions. (*iii*) The LDA experiments have provided accurate and detailed information on the velocity field and offered the possibility to validate the computational results. These three methods, each having their own strong points and restrictions, have proven to be complementary. In conclusion it may be stated that the chosen course is excellent for studying this kind of flow problems.

The finite element computations have given a useful and clear insight into the complex three-dimensional axial and secondary flow fields in the carotid artery bifurcation. However, the computations are not suitable to describe the unsteady shear layer behavior accurately. Refining the spatial and temporal discretization of the method is expected to improve the results. However, with the present generation of computers this can not be achieved easily, due to the time and memory consuming character of the computations. A more structural way to improve the computational accuracy is to use the highly accurate and efficient high-order spectral element method, that has been recently developed for 2D incompressible flow problems (Timmermans, 1994). For future research on this topic the use of such a spectral element method, extended to 3D flow analysis, is strongly recommended.

Considering the fluid dynamics of the flow in models of the non-stenosed and the 25% stenosed carotid artery bifurcation, the experiments indicate that the unstable shear layer behavior in the initial phase of diastole and the frequency contents of the velocity signals at that location are influenced by the presence of a minor stenosis. The present study has shown that even for well-controlled conditions and accurate experimental techniques this influence is not determinative for the detection of minor stenoses, since the effects on the flow field are small, local in time and space and dependent on other factors like the inflow conditions, the geometry, wall distensibility and the non-Newtonian fluid behavior.

In the experiments and computations from this study no local vortex shedding from the rear edge of the stenosis is found. It is shown that for all phases of the flow pulse the stenosis is located in a region with low velocities. As a result the studies on pulsatile flow in narrowed tubes, where the stenoses are located in the main flow and high shear stresses are resulting, are of minor importance for the investigation of stenosed carotid artery flow.

The evaluation of the first velocity moment at peak-systole $\bar{r}$(*peak-syst.*) as a function of the axial position in the internal carotid artery is believed to be a possibly useful parameter in the detection of stenoses, especially when larger degrees of stenoses are considered (see also section 8.3). A decrease in $\bar{r}$(*peak-syst.*) followed by a (sudden) increase seems to mark the presence of a stenosis. Since this approach considers only relative changes in the first velocity moment, it is expected to be rather insensible for inter-individual differences like the shape of the carotid sinus, the bifurcation angle, the specific wall distensibility and the flow conditions. Though it is believed that this method, solely considering the

hemodynamics of carotid artery flow, is only promising for *moderate* stenoses (> 50% area reduction, which is equivalent to 30% diameter reduction for circular cross-sections), future research will be needed to investigate the value of this parameter for the detection of moderate stenoses in clinical practice.

To achieve the main objective of this thesis: the detection of *minor* stenoses (less than 25% area reduction), local changes of the wall distensibility at stenosed sites are believed to play an important role. Since the development of atherosclerosis at an early stage of the disease is attended by a stiffening of the arterial wall, it might be expected that the detection of minor stenoses will be enhanced when information on the hemodynamics is combined with measurements of local changes of the wall distensibility at stenosed sites.

Appendix A

Boundary condition for the computations

In this appendix the derivation of the axial velocity profiles, that are prescribed at the entrance of the common carotid artery as a inflow condition, will be given. The theory is based on the theory of Witzig (1914) and described in more detail by Womersley (1957). He considered the oscillatory flow of a viscous fluid in straight, rigid, circular tubes. The definitions of the problem are given in figure A.1 It is assumed that the tube is sufficiently
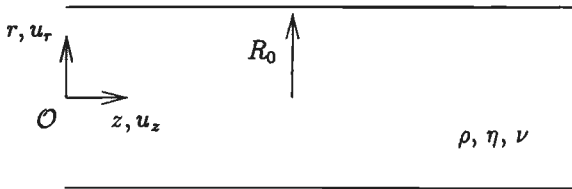
Figure A.1: *Definition of the parameters, that are used in this appendix.*

long in relation to its diameter, so that the radial velocity $u_r = 0$ and the axial velocity along the tube u_z is independent of the axial distance $\partial u_z/\partial z = 0$. Then the Navier-Stokes equations for this problem reduce to:

$$\frac{\partial u_z}{\partial t} = -\frac{1}{\rho}\frac{\partial p}{\partial z} + \nu\left(\frac{\partial^2 u_z}{\partial r^2} + \frac{1}{r}\frac{\partial u_z}{\partial r}\right), \tag{A.1}$$

in which $\partial p/\partial z$ is independent of r and z, since the flow is fully developed. Next we assume an applied pressure gradient that is composed of N Fourier components:

$$\frac{\partial p}{\partial z} = \sum_{n=0}^{N} A_n\, e^{in\omega t}. \tag{A.2}$$

Writing also

$$u_z = \sum_{n=0}^{N} u_n(r) e^{in\omega t}, \tag{A.3}$$

and introducing the dimensionless parameters $\alpha_n = R_0\sqrt{(n\omega)/\nu}$ and $y = r/R_0$, equation A.1 leads to

$$\frac{\partial^2 u_n}{\partial y^2} + \frac{1}{y}\frac{\partial u_n}{\partial y} - i\alpha_n^2 u_n(y) = \frac{A_n R_0^2}{\eta}. \tag{A.4}$$

By substituting $y = s/(\alpha_n i^{3/2})$ this differential equation leads to a standard differential equation. Together with the boundary condition $u_n(y = 1) = 0$ the solution for u_n then can be written as:

$$u_n(y) = -\frac{A_n}{in\omega\rho}\left(1 - \frac{J_0(\alpha_n i^{3/2} y)}{J_0(\alpha_n i^{3/2})}\right). \tag{A.5}$$

Here J_0 is a Bessel function of the first kind of zeroth order (see also Kreyszig, 1983). Together with A.3 the axial velocity profile can be written as

$$u_z(y) = \sum_{n=0}^{N} -\frac{A_n}{in\omega\rho}\left(1 - \frac{J_0(\alpha_n i^{3/2} y)}{J_0(\alpha_n i^{3/2})}\right) e^{in\omega t}. \tag{A.6}$$

A group of representative velocity profiles of this type of motion during one flow cycle and for one component ($n = 1$) is given in figure A.2
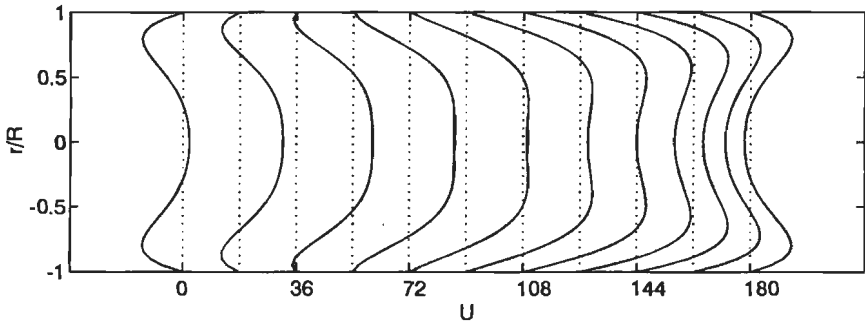
Figure A.2: *Typical profiles of the flow from a sinusoidal pressure gradient in a straight rigid tube. The results are given at intervals of 18° and for $\alpha = 6$.*

As the inflow conditions are determined by the Reynolds number and thus by the mean cross-sectional averaged velocity, the flow rate

$$Q(t) = \sum_{n=0}^{N} Q_n e^{in\omega t} \tag{A.7}$$

needs to be derived from equation A.6 by interpolation. This results in

$$Q(t) = 2\pi \int_0^{R_0} r\, u_z(r)\, dr = 2\pi R_0^2 \int_0^1 y\, u_z(y)\, dy \tag{A.8}$$

$$Q(t) = -\pi R_0^2 \sum_{n=0}^{N} \frac{A_n}{in\omega\rho}(1 - F_{10}(\alpha_n))\, e^{in\omega t}, \tag{A.9}$$

with $F_{10}(\alpha_n)$ defined as

$$F_{10}(\alpha_n) = \frac{2J_1(\alpha_n i^{3/2})}{\alpha_n i^{3/2} J_0(\alpha_n i^{3/2})}. \tag{A.10}$$

Here the formula for integration of Bessel functions of the first kind of zeroth order (Kreyszig, 1983) are used to derive equation A.9. The result is an expression, where Bessel functions of the first kind of first order also play a role (see equations A.9 and A.10).

With the theory, described above, it is easy to calculate the axial velocity profiles $u_z(r,t)$, that should be prescribed at the entrance of the common carotid artery. Starting with the inflow condition of a time varying Reynolds number $Re(t)$, the according flow $Q(t)$ can be calculated, using the density ρ, the dynamic viscosity η and the diameter of the common carotid artery D. Next the flow pulse $Q(t)$ has to be Fourier decomposed so that for each component n the angular frequency $n\omega$ and the amplitude Q_n are known. In the present study the flow pulse has been Fourier decomposed into 20 components, resulting in an error less than 1%. Next with the help of equations A.9 and A.10 the corresponding factors A_n are calculated for each component, using α_1 (i.e. the Womersley parameter of the fundamental harmonic, that equals to 6) as a known input parameter. Finally the axial velocity profile is calculated from equation A.6 for each component n and a summation of all components leads to the total axial velocity profile that is prescribed at the entrance of the common carotid artery to obtain the desired initial condition.

Appendix B

The differential Doppler technique

B.1 Doppler shift on scattering

The fundamental phenomenon in laser Doppler anemometry is the Doppler shift of light that is scattered by small particles. Consider the situation as given in figure B.1. A particle located at position $\vec{x}(t)$ scatters the light from an incident illuminating beam with complex electric vector $\vec{E}_i$, frequency ω_0 and intensity E_0^2. The illuminating beam is assumed to be linearly polarized and the wave number is denoted as $\vec{k} = k\vec{e}_k$, where $\vec{e}_k$ represents the direction of propagation. It can be represented by the complex wave

$$\vec{E}_i = E_i \vec{e}_k = E_0\, e^{i(\omega_0 t - k\vec{e}_k \cdot \vec{x})}\, \vec{e}_k. \tag{B.1}$$

The electric vector is given by the real part of $\vec{E}_i$ and will be considered in the sequel of this section. The scattered light wave can be regarded as a spherical wave, provided that the distance r to the observer is much larger than both the wavelength of the light (λ_0) and the mean diameter of the scattering particle. Then the scattered wave can be written
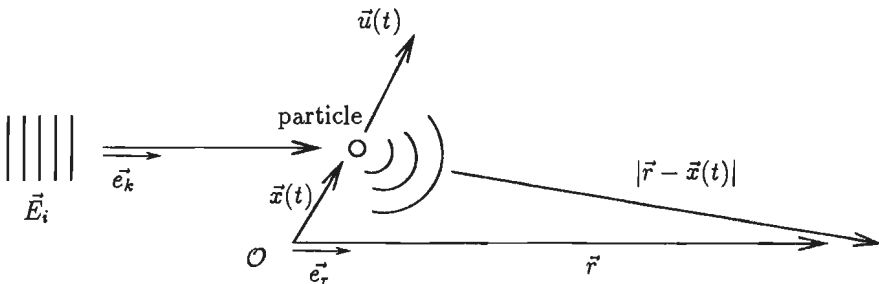
Figure B.1: *Diagram for the derivation of the Doppler shift on scattering by a moving particle.*

as follows (Kerker, 1969)

$$\vec{E}_s = \frac{\sigma E_i}{k|\vec{r} - \vec{x}|} e^{-ik|\vec{r} - \vec{x}|} \vec{e}_s, \tag{B.2}$$

where σ is a complex scattering coefficient, dependent on the scattering angle, the phase shift and polarization of the scattered wave relative to the illuminating wave $\vec{E}_i$.

The origin in figure B.1 is assumed to be positioned in the center of the illuminated region where scattering occurs (i.e. the measuring volume). As this measuring volume is very small, it is realistic to assume that $|\vec{x}| \ll |\vec{r}|$. Thus from a simple geometric consideration it follows that $|\vec{r} - \vec{x}| \cong |\vec{r}| - \vec{x} \cdot \vec{e}_r$ with $r = |\vec{r}|$, and equation B.2 can be rewritten as

$$\vec{E}_s = \frac{\sigma \vec{E}_0}{k|\vec{r} - \vec{x}|} e^{i(\omega_0 t - kr + k\vec{x} \cdot (\vec{e}_r - \vec{e}_k))}. \tag{B.3}$$

The instantaneous frequency of nearly harmonic signals is the time derivative of its phase. Let $\vec{u}(t)$ be the velocity of the particle, then from equation B.3 the frequency can be denoted as

$$\omega_s = \omega_0 + k\vec{u}(t) \cdot (\vec{e}_r - \vec{e}_k), \tag{B.4}$$

or in units of Hertz

$$\nu_s = \nu_0 + \frac{\vec{u}(t) \cdot (\vec{e}_r - \vec{e}_k)}{\lambda_0}. \tag{B.5}$$

It can be seen that the Doppler shift of the scattered light from the moving particle is the sum of a shift associated with the particle's velocity component $(-\vec{u} \cdot \vec{e}_k)$ away from the incident wave and the particle's velocity component $(\vec{u} \cdot \vec{e}_r)$ towards the observer at $\vec{r}$.

B.2   The differential Doppler method

Next two intersecting plane light waves $\vec{E}_{i1}$ and $\vec{E}_{i2}$ with frequencies ν_0 and $\nu_0 + \nu_s$, propagating in two different directions $\vec{e}_{k1}$ and $\vec{e}_{k2}$ are considered as presented in figure B.2. As will be shown the superposition of a shift frequency ν_s offers the possibility to distinguish between positive and negative velocities. The measuring volume is the intersection of the two focused beams of similar intensity with inclination angle θ. The scattered light is observed in the direction of detector $\vec{e}_r$. A particle moving through the measuring volume scatters two waves (E_{s1} from E_{i1} and E_{s2} from E_{i2}) with frequencies

$$\nu_{s1} = \nu_0 + \frac{\vec{u}(t) \cdot (\vec{e}_r - \vec{e}_{k1})}{\lambda}, \tag{B.6}$$

$$\nu_{s2} = \nu_0 + \nu_s + \frac{\vec{u}(t) \cdot (\vec{e}_r - \vec{e}_{k2})}{\lambda}. \tag{B.7}$$

The frequency difference can be written as

$$\nu_{s1} - \nu_{s2} = \nu_s + \frac{\vec{u}(t) \cdot (\vec{e}_{k2} - \vec{e}_{k1})}{\lambda}, \tag{B.8}$$
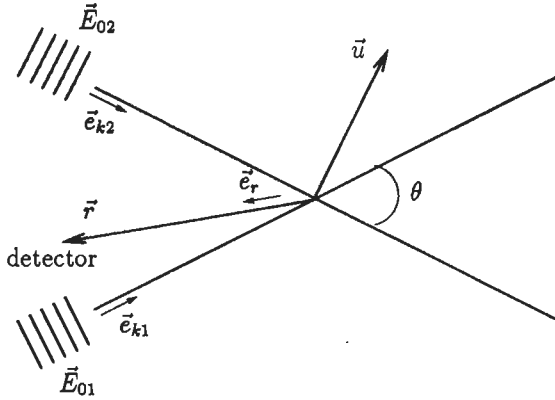
Figure B.2: *Definition of symbols for the differential Doppler technique.*

After a simple geometric consideration equation B.8 can be rewritten as

$$\nu_{s1} - \nu_{s2} = \nu_s + \frac{2u}{\lambda} \sin\frac{\theta}{2}, \tag{B.9}$$

where u represents the velocity component in the direction normal to the bisector of the two laser beams. The first term is a constant frequency difference between the two illuminating beams, used for the determination of the sign of the velocity. For negative velocities the frequency difference is smaller than ν_s, whereas for positive velocities this difference is larger than ν_s. The second term, representing the frequency difference between the Doppler shifts, is linear dependent on the velocity component u of the scattering particle in the direction normal to the bisector of the two illuminating laser beams. It appears to be independent of the scattering direction $\vec{e}_r$ and thus independent of the detector's location. Only the intensity of the scattered light will be dependent on the scattering direction.

The scattered light is detected by a photomultiplier, which can not follow the high frequency of the laser light (ν_0). As a result the detector generates an output signal which is linear dependent on u according to equation B.9.

In the case that more velocity components have to be measured simultaneously, the same principle can be applied, using two additional laser beams for each extra component to be measured. This can only be done on the condition that the frequency difference between the additional set of beams and the original set of beams is large compared to $\nu_{s1} - \nu_{s2}$ from equation B.9.

Appendix C

Literature review on unstable shear layer flow

Without giving a complete overview of the field of stability analysis, some basic fundamentals and phenomena that can be interesting for the flow in the carotid artery bifurcation are summarized here.

C.1 Kelvin-Helmholtz instability

Consider two uniform potential flows of an incompressible and inviscid medium, separated by an infinitesimally thin shear layer of uniform vortex strength $U_1 - U_2$ (see also figure C.1a). This vortex sheet is susceptible for the development of a Kelvin-Helmholtz instability, which can be analyzed using *linear stability analysis* (see also Drazin and Reid, 1981). The mean flow is assumed to be two-dimensional in the x-y plane. If the undisturbed flow $\vec{u} = u(y)\vec{e}_x$ is disturbed by $u' << u$ and $v' << u$ a perturbation stream function can be defined by $\vec{u}' = \nabla \times \Psi'$. For harmonic disturbances, propagating in the x-direction the stream function can be written as

$$\Psi'(x, y, t) = \hat{\Psi}(y)e^{i(kx-\omega t)}, \tag{C.1}$$

where $\hat{\Psi}(y)$ is the amplitude of the disturbance, $k = k_r + ik_i$ the complex wave number and $\omega = \omega_r + i\omega_i$ the complex frequency. For spatial instabilities, ω_i is set to zero and the disturbance is spatially amplified if $k_i < 0$. Drazin and Reid only considered temporal instabilities, where k_i is set to zero and the disturbance is amplified in time if $\omega_i > 0$. Using linear stability analysis Drazin and Reid (1981) showed that the complex frequency can be written as follows

$$\omega = -\frac{k}{2}(U_1 + U_2) \pm i\frac{k}{2}(U_1 - U_2), \tag{C.2}$$

where k is the real-valued wave number of the disturbance and $(U_1 - U_2)$ is the strength of the vortex sheet. From equations C.1 and C.2 it can be seen that an initially infinitesimally
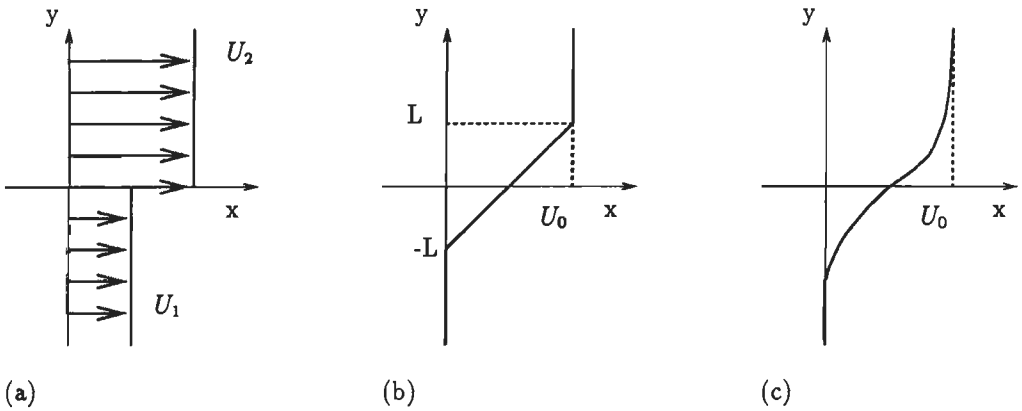
Figure C.1: *Vortex sheet with infinitesimally thin vortex layer (a), a layer with finite thickness, assuming a linear variation of the velocity between the two regions (b) and the hyperbolic tangent profile (c).*

small disturbance amplifies exponentially in time. The amplification factor is determined by the imaginary part of the complex frequency ω_i and amounts $\frac{k}{2}(U_1 - U_2)$. The vortex layer always appears to be unstable, except for $U_1 = U_2$. The highest amplification factor is found for the disturbance with the highest wave number, i.e. the largest frequency. The disturbances are moving with phase-velocity $c = \omega_r/k_r = (U_1 + U_2)/2$, the average velocity of the main flow.

C.2   Shear layer of finite thickness

In reality the action of viscosity spreads the vorticity in a layer of finite thickness. Drazin and Howard (1966) assumed a linear variation of the velocity between the two uniform flows, as presented in figure C.1b. They showed that the layer is not unconditionally unstable anymore. The layer becomes temporally unstable if $kL < 0.64$, where k is the real-valued wave number and $2L$ the distance between the two uniform flows. The amplification factor is dependent on kL and is found to be maximal for $kL \approx 0.4$, being 0.1.

Michalke (1964) used the inviscid linearized stability theory to study numerically the temporal instability of a shear layer with a more realistic velocity profile

$$u(y) = \frac{U_0}{2}(1 + \tanh(\frac{y}{L})),\tag{C.3}$$

as shown in figure C.1c. The results are qualitatively similar to the results of Drazin and Howard. Some quantitative differences are found in the criterion for instability ($kL < 1$) and the maximum amplification factor (0.095 for $kL \approx 0.44$). Michalke showed that the

propagation velocities $c = \omega_r/k_r$ of the perturbations for temporal instabilities are equal to the local velocity of the unperturbed flow.

Michalke (1965) also studied the spatial linear stability of a hyperbolic tangent velocity profile for inviscid fluids. He showed that the curves, describing the amplification of the disturbances as a function of the wave number, for spatial instabilities only slightly differ from those for temporal instabilities. However, considering the phase velocity of the disturbances, significant differences between the temporal and the spatial cases are found. In contradiction to the temporal case the phase velocity for spatial instabilities depends strongly on the frequency of the disturbance, especially for small frequencies. Only the most amplified wave, corresponding to the natural frequency of the shear layer, moves with a phase velocity that is equal to the average velocity of the main flow.

C.3 Non-linear effects

Knio and Gnoniem (1990) studied the influence of non-linear effects on the behavior of a 2D free shear layer in unbounded steady flows. They concluded that the development of disturbances in the shear layer can be subdivided into three stages.

first stage: In the first stage an exponential growth of the amplitude of the oscillation occurs. The shape of the perturbations remains unchanged. This can be described by means of linear stability analysis for example as in the previous paragraph on Kelvin-Helmholtz instabilities.

second stage: In the second stage a non-linear growth occurs, characterized by the roll-up of the shear layer and an extension of the shear layer in the cross-stream direction. For the example of the Kelvin-Helmholtz instability the non-linear effects can be described as follows. Beyond the stage of exponential growth, the Kelvin-Helmholtz instability waves evolve into a periodic array of compact spanwise vortices, moving at the average fluid velocity. In figure C.2 an illustration of this phenomenon is given. The recirculating regions, which contain most of the vorticity, are usually referred

Figure C.2: *Development of Kelvin-Helmholtz instability at the interface of two fluids (Copyright © Van Dijke 1982, The parabolic press - Reprinted with permission).*

to as Kelvin cat's eyes. The roll-up process appears to be predominantly two-dimensional (Ho and Huerre, 1984).

third stage: Next a completion of the growth of the instability in cross-stream direction takes place, accompanied by pairing of vortex structures. Finally transition to turbulence occurs and the instability becomes essentially three-dimensional. The phenomenon of vortex pairing has been visualized by Roshko (1976) and a typical result is given in figure C.3. In the vortex pairing process, the vorticity is constantly being redistributed into larger and larger vortices. The wavelength and strength is doubled after each interaction, or equivalently, subharmonics of the disturbance frequency are generated. As a result the spectrum exhibits a shift towards lower frequencies with increasing axial distance.

C.4   Influence of viscosity

The stability of viscous flows has been described first by Orr (1907) and Sommerfeld (1908), who derived the well-known Orr-Sommerfeld equation (Drazin and Reid, 1981). The solution of this fourth order differential equation with the help of heuristic methods of approximation and computational methods have led to an understanding of the role of viscosity. In summary, it can be stated that the influence of viscosity can be twofold. Firstly, viscosity can generate instabilities that do not exist in the inviscid theory. These instabilities are referred to as viscid modes. Secondly, for the inviscid modes corresponding to the predicted instabilities in the inviscid theory, the viscosity mainly acts as a damping mechanism (Drazin and Reid, 1981).

C.5   Influence of walls

To study the influence of boundaries on the stability of free shear layers, Drazin and Reid (1981) analyzed an unbounded and a bounded shear layer with piecewise-linear velocity profiles. The unbounded shear layer has already been described in paragraph C.2. For the bounded case the walls are positioned at $y = 1$ and $y = -1$ and the shear layer is positioned between $y = L$ and $y = -L$. It follows that the flow is unstable provided that $L < \frac{1}{2}$. This condition on the gradient of the shear layer causes the flow to be more stable in the bounded case, compared to the unbounded case, where instability always can be expected.

The influence of boundaries on the stability of free shear layers is studied numerically by Lie and Riahi (1988). Using linear spatial analysis for the viscous case they found that the presence of boundaries resulted in much higher values of the minimum Reynolds number for instability to occur. Here again the boundaries seem to have a damping effect on the development of disturbances in the shear layer.
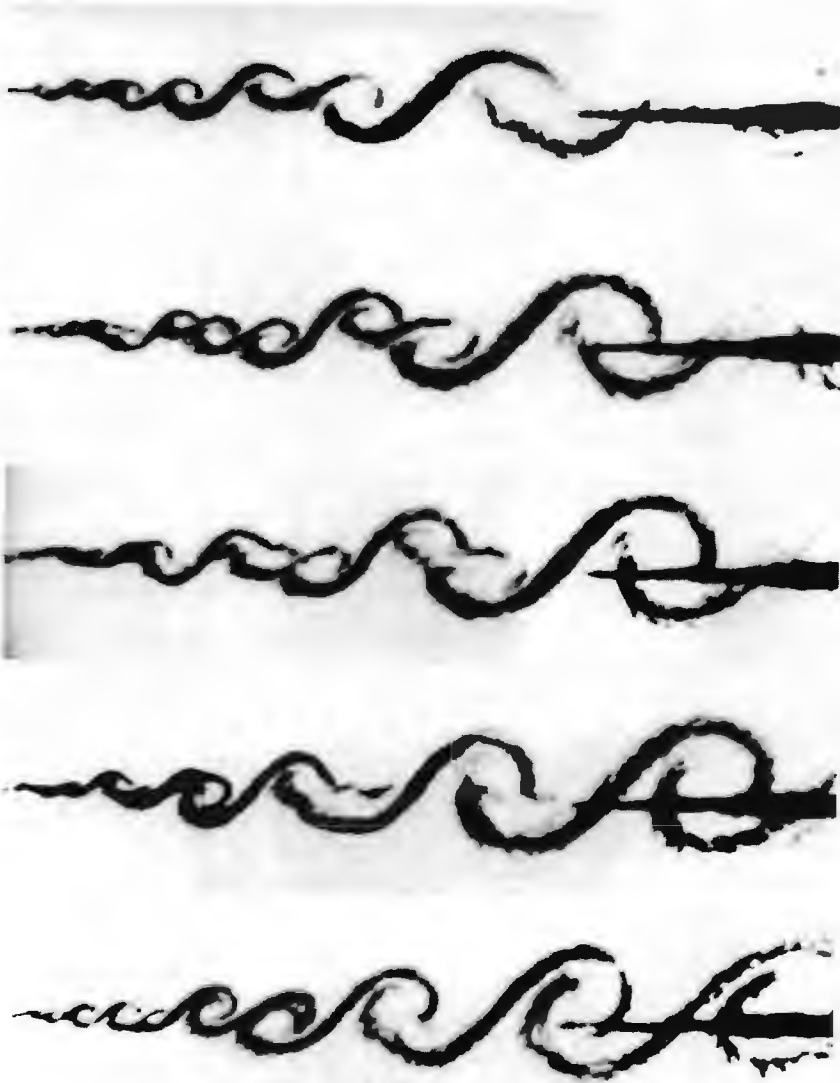
Figure C.3: *Vortex pairing occurring in a shear layer according to Roshko (1976). Two vortices, distinct in the top photograph, are pairing in the center and have become a single larger vortex at the bottom (Copyright ©1976 AIAA - Reprinted with permission).*

References

[1] Ahmed S.A. and Giddens D.P. (1983a) Flow disturbance measurements through a constricted tube at moderate Reynolds numbers, *J. Biomech.* **16**, 955-963.

[2] Ahmed S.A. and Giddens D.P. (1983b) Velocity measurements in steady flow through axisymmetric stenoses at moderate Reynolds numbers, *J. Biomech.* **16**, 505-516.

[3] Ahmed S.A. and Giddens D.P. (1984) Pulsatile poststenotic flow studies with Laser Doppler anemometry, *J. Biomech.* **17**, 695-705.

[4] Anayiotos A.S., Giddens D.P., Jones S.A., Glagov S. and Zarins C.K. (1991) Effects of arterial wall distensibility on the near wall flow field in a model of a human carotid bifurcation, *ASME Adv. Bioeng. 1991* **BED 20**, 17-19.

[5] Anayiotos A.S., Giddens D.P., Jones S.A., Glagov S. and Zarins C.K. (1992) General flow characteristics in a compliant model of a carotid bifurcation, *ASME Adv. Bioeng. 1992* **BED 22**, 281-284.

[6] Baaijens J.P.W., Van Steenhoven A.A. and Janssen J.D. (1993) Numerical analysis of steady generalized Newtonian blood flow in a 2D rigid model of the carotid artery bifurcation, *Biorheology* **30**, 63-74.

[7] Balasubramanian K, Giddens D.P. and Mabon R.F. (1979) Steady flow at the carotid bifurcation, in: *Biofluid mechanics 2 (Ed. D.J. Schneck)*, 475-496.

[8] Bharadvaj B.K., Mabon R.F., and Giddens D.P. (1982a) Steady flow in a model of the human carotid bifurcation - Part I: Flow visualization, *J. Biomech.* **15**, 349-362.

[9] Bharadvaj B.K., Mabon R.F., and Giddens D.P. (1982b) Steady flow in a model of the human carotid bifurcation - Part II: Laser-Doppler Anemometer measurements, *J. Biomech.* **15**, 363-378.

[10] Brands P.J. (1993), Personal communication, University Maastricht.

[11] Caro C.G., Dumoulin C.L., Graham J.M.R., Parker K.H. and Souza S.P. (1992) Secondary flow in the human common carotid artery imaged by MR angiography, *J. Biomech. Eng.* **114**, 147-149.

[12] Cassanova R.A. (1978) Disorder distal to modeled stenoses in steady and pulsatile flow, *J. Biomech.* **11**, 411-453.

[13] Clark M.E., Robertson J.M. and Cheng L.C. (1983) Stenosis severity effects for unbalanced simple-pulsatile bifurcation flow, *J. Biomech.* **16**, 895-906.

[14] Corver J.A.W.M., Van de Vosse F.N., Van Steenhoven A.A. and Reneman R.S. (1985) The influence of a small stenosis in the carotid artery bulb on adjacent axial velocity profiles, in: *Biomechanics: Current Interdisciplinary Research (Ed. S.M. Perren and E. Schneider)*, Martinus Nijhoff Publishers, Dordrecht.

[15] Cuvelier C., Segal A. and Van Steenhoven A.A. (1986) *Finite element methods and Navier-Stokes equations*, D. Reidel Publishing Company, Dordrecht.

[16] Davis S.H. (1976) The stability of time-periodic flows, *Ann. Rev. Fluid Mech.* **8**, 57-74.

[17] Van Dijke M. (1982) *An album of fluid motion*, The Parabolic Press, Stanford, California.

[18] Drazin P.G. and Howard L.N. (1966) Hydrodynamic stability of parallel flow of inviscid fluid, *Adv. Appl. Mech.* **9**, 1-89.

[19] Drazin P.G. and Reid W.H. (1981) *Hydrodynamic stability*, Cambridge University Press, Cambridge.

[20] Drain L.E. (1980) *The laser doppler technique*, John Wiley & Sons, Chicester.

[21] Evans D.H., Barrie W.W., Asher M.J., Bentley S. and Bell P.R.F. (1980) The relationship between ultrasonic pulsatility index and proximal arterial stenosis in a canine model, *Circ. Res.* **46**, 470-475.

[22] Evans D.H., McDicken W.N., Skidmore R. and Woodcock J.P. (1989) *Doppler Ultrasound; Physics, instrumentation and clinical applications*, Chapt. 10, 162-187, John Wiley & Sons, Chichester.

[23] Fei D.Y., Billian C. and Rittgers S.E. (1988) Flow dynamics in a stenosed carotid bifurcation model - Part I: Basic velocity measurements, *Ultrasound in Med. & Biol.* **14**, no. 1, 21-31.

[24] Fukushima T., Homma T., Harakawa K., Sakata N. and Azuma T. (1988) Vortex generation in pulsatile flow through arterial bifurcation models including the human carotid artery, *ASME J. Biomech. Eng.* **110**, 166-171.

[25] Goldstein R.J. (1983) *Fluid mechanics measurements*, Hemisphere Publishing Corporation, New York.

[26] Gosling R.G. and King D.H. (1974) Continuous wave ultrasound as an alternative and complement to X-rays in vascular examination, In: *Cardiovascular applications of ultrasound (Ed. R.S. Reneman)*, Chapt. 22, 266-282, North-Holland, Amsterdam.

[27] Guyton A.C. (1985) *Anatomy and physiology*, Saunders College Publishing, Philadelphia.

[28] Hinze J.O. (1975) *Turbulence, second edition*, Mc Graw-Hill, New York.

[29] Ho C.M. and Huerre P. (1984) Perturbed free shear layers, *Fluid Mech.* **16**, 365-424.

[30] Johnston K.W., Brown P.M. and Kassam M. (1982) Problems of carotid Doppler scanning which can be overcome by using frequency analysis, *Stroke* **13**, 660-666.

[31] Johnston K.W., Kassam K. Koers J., Cobbold R.S.C. and MacHattie D. (1984) Comparative study of four methods for quantifying Doppler ultrasound waveforms from the femoral artery, *Ultrasound in Med. & Biol.* **10**, 1-12.

[32] Junger M., Chapman B.L.W., Underwood C.J. and Charlesworth D. (1984) A comparison between two types of waveform analysis in patients with multisegmental arterial disease, *Br. J. Surg.* **71**, 345-348.

[33] Jungquist G., Arborelius M.Jr. and Lindell S. (1989) Features of carotid artery flow velocity in healthy subjects and consequences for evaluating stenosis in the internal carotid artery, *Ultrasound in Med. & Biol.* **15**, 305-310.

[34] Kerker M. (1969) *The scattering of light*, Chapt. 3, Academic, New York,

[35] Khalifa A.M.A. and Giddens D.P. (1981) Characterization and evolution of poststenotic flow disturbances, *J. Biomech.* **14**, 279-296.

[36] Kleinstreuer C., Nazemi M. and Archie J.P. (1991) Hemodynamics analysis of a stenosed carotid bifurcation and its plaque-mitigating design, *ASME J. Biomech. Eng.* **113**, 330-335.

[37] Knio O.M. and Gnoniem A.F. (1990) Three-dimensional vortex simulation of roll-up and entrainment in a shear layer, *J. Comp. Phys.*, 172-223.

[38] Kreyszig E. (1983) *Advanced engineering mathematics*, John Wiley & Sons, New York.

[39] Ku D.N. and Giddens D.P. (1983) Pulsatile flow in a model carotid bifurcation, *Arteriosclerosis* **3**, 31-39.

[40] Ku D.N., Giddens D.P., Phillips D.J. and Strandness D.E. (1985a) Hemodynamics of the normal human carotid bifurcation: in vitro and in vivo studies, *Ultrasound in Med. & Biol.* **11**, no. 1, 13-26.

[41] Ku D.N., Giddens D.P., Zarins C.K. and Glagov S. (1985b) Pulsatile flow and atherosclerosis in the human carotid bifurcation, *Arteriosclerosis* **5**, 293-302.

[42] Ku D.N. and Liepsch D. (1986) The effects of non-Newtonian viscoelastic and wall elasticity on flow at a 90° bifurcation, *Biorheology* **23**, 359-370.

[43] Ku D.N. and Giddens D.P. (1987) Laser Doppler measurements of pulsatile flow in a model carotid bifurcation, *J. Biomech.* **20**, 407-421.

[44] Lie K.H. and Riahi D.N. (1988) Numerical solution of the Orr-Sommerfeld equation for mixing layers, *Int. J. Eng. Sci.* **26**, no. 2, 163-174.

[45] Liepsch D. and Moravec S. (1984) Pulsatile flow of non-Newtonian fluid in distensible models of human arteries, *Biorheology* 21, 571-586.

[46] Liepsch D., Poll A. and Pflugbeil G. (1993) In vitro laser anemometry blood flow systems, *Laser Anemometry Adv. & Appl.* **SPIE 2052**, 163-178.

[47] LoGerfo F.W., Nowak M.D., Quist W.C., Crawshaw H.M. and Bharadvaj B.K. (1981) Flow studies in a model carotid bifurcation, *Arteriosclerosis* **1**, 235-241.

[48] Van Merode T., Hick P.J.J., Hoeks A.P.G. and Reneman R.S. (1988) The diagnosis of minor to moderate atherosclerotic lesions in the carotid artery bifurcation by means of spectral broadening combined with the direct detection of flow disturbances using a multi-gate pulsed Doppler system, *Ultrasound in Med. & Biol.* **14**, no.6, 459-464.

[49] Van Merode T., Lodder J., Smeets F.A.M., Hoeks A.P.G. and Reneman R.S. (1989) Accurate noninvasive method to diagnose minor atherosclerotic lesions in carotid artery bulb, *Stroke* **20**, 1336-1340.

[50] Michalke A. (1964) On the inviscid instability of the hyperbolic-tangent velocity profile, *J. Fluid Mech.* **19**, 543-556.

[51] Michalke A. (1965) On spatially growing disturbances in an inviscid shear layer, *J. Fluid Mech.* **23**, 521-544.

[52] Motomiya M. and Karino T. (1984) Flow patterns in the human carotid artery bifurcation, *Stroke* **15**, no. 1, 50-56.

[53] Nazemi M., Kleinstreuer C. and Archie J.P.Jr. (1990) Pulsatile two-dimensional flow and plaque formation in a carotid artery bifurcation, *J. Biomech.* **23**, no. 1, 1031-1037.

[54] Nerem R.M. (1992) Vascular fluid mechanics, the arterial wall, and atherosclerosis, *ASME J. Biomech. Eng.* 114, 274-282.

[55] Olson D.E. (1971), *Fluid mechanics relevant to respiration: flow within curved or elliptical tubes and bifurcating systems*, PhD Thesis, University of London.

[56] Orr W.M.F. (1907) The stability or instability of the steady motions of a perfect liquid and of a viscous liquid, *Proc. Roy. Irish Acad.* **A27**, 9-138.

[57] Palmen D.E.M., Van de Vosse F.N., Janssen J.D. and Van Dongen M.E.H. (1993) The influence of minor stenoses on the flow in the carotid artery bifurcation - Hydrogen-bubble visualization, accepted for publication in *J. Biomech.*

[58] Perktold K. and Hilbert D. (1986) Numerical simulation of pulsatile flow in a carotid bifurcation model, *J. Biomed. Eng.* **8**, 193-199.

[59] Perktold K., Peter R. and Resch M. (1989) Pulsatile non-Newtonian blood flow simulation through a bifurcation with an aneurism, *Biorheology* 26, 1011-1030.

[60] Perktold K., and Resch M. (1990) Numerical flow studies in human carotid artery bifurcations: basic discussion of the geometric factor in atherogenesis, *J. Biomed. Eng.* **12**, 111-123.

[61] Perktold K., Resch M. and Peter R.O. (1991a) Three-dimensional numerical analysis of pulsatile flow and wall shear stress in the carotid artery bifurcation, *J. Biomech.* **24**, no. 6, 409-420.

[62] Perktold K., Peter R.O., Resch M. and Langs G. (1991b) Pulsatile non-Newtonian blood flow in three-dimensional carotid bifurcation models: a numerical study of flow phenomena under different bifurcation angles, *J. Biomed. Eng.* **13**, 507-515.

[63] Perktold K. and Rappitsch G. (1993) Numerical analysis of arterial wall mechanics and local blood phenomena, *ASME Adv. Bioeng.* **BED 26**, 127-130.

[64] Pourcelot L. (1976) Diagnostic Ultrasound for cerebral vascular diseases, In: *Present and future of diagnostic ultrasound (Ed.: Donald, I. and Levi, DS.)*, 141-147, Kooyker, Rotterdam.

[65] Reneman R.S. and Spencer M.P. (1979) Local Doppler audio spectra in normal and stenosed carotid arteries in man, *Ultrasound in Med. & Biol.* **5**, 1-11.

[66] Reneman R.S., Van Merode T., Hick P. and Hoeks A.P.G. (1985) Flow velocity patterns in and distensibility of the carotid artery bulb in subjects of various ages, *Circulation* **71**, no. 3, 500-509.

[67] Reuderink P.J. (1991) *Analysis of the flow in a 3D distensible model of the carotid artery bifurcation*, PhD Thesis, Eindhoven University of Technology.

[68] Rindt C.C.M., Van de Vosse F.N., Van Steenhoven A.A. and Janssen J.D. (1987) A numerical and experimental analysis of the flow field in a two-dimensional model of the human carotid artery bifurcation, *J. Biomech.* **20**, no. 5, 499-509.

[69] Rindt C.C.M., Van Steenhoven A.A., and Reneman R.S. (1988) An experimental analysis of the flow field in a three-dimensional model of the human carotid artery bifurcation, *J. Biomech.* **21**, 985-991.

[70] Rindt C.C.M. (1989) *Analysis of the three dimensional flow field in the carotid artery bifurcation*, PhD Thesis, Eindhoven University of Technology.

[71] Rindt C.C.M., Van Steenhoven A.A., Janssen J.D., Reneman R.S. and Segal A. (1990) A numerical analysis of steady flow in a three-dimensional model of the carotid artery bifurcation, *J. Biomech.* **23**, no. 5, 461-473.

[72] Rindt C.C.M. and Van Steenhoven A.A. (1994) Unsteady flow in a rigid 3D-model of the carotid artery bifurcation; Experimental validation of a finite element model, Submitted to *J. Biomech. Eng.*

[73] Rittgers S.E. and Fei D.Y. (1988) Flow dynamics in a stenosed carotid bifurcation model - Part II: Derived indices, *Ultrasound in Med. & Biol.* **14**, no. 1, 33-42.

[74] Roshko A. (1976) *AIAA J.* **14**, 1349-1357.

[75] Schraub F.A., Kline S.J., Henry J., Runstadler P.W.jr, Littell A. (1965) Use of hydrogen bubbles for quantitative determination of time-dependent velocity fields in low-speed water flows, *ASME J. Basic Engineering* **87**, 429-444.

[76] Segal A. (1984) *SEPRAN user manual, standard problems and programming guide*, Ingenieursbureau SEPRA, Leidschendam.

[77] Sommerfeld A. (1908) Ein Beitrag zur hydrodynamischen Erklaerung der turbulenten Fluessigkeitsbewegungen, *Proc. 4th Int. Conf. Math., Rome* **III**, 116-124.

[78] Timmermans L.J.P. (1994) *Analysis of spectral element methods with application to incompressible flow*, PhD Thesis, Eindhoven University of Technology.

[79] Van de Vosse F.N., Van Steenhoven A.A. and Janssen J.D. (1986) A finite element approximation of the unsteady two dimensional Navier-Stokes equations, *Int. J. Num. Methods in Fluids* **6**, 427-443.

[80] Van de Vosse F.N. (1987) *Numerical analysis of carotid artery flow*, PhD Thesis, Eindhoven University of Technology.

[81] Van de Vosse F.N., Van Steenhoven A.A., Janssen J.D. and Reneman R.S. (1990) A two-dimensional numerical analysis of unsteady flow in the carotid artery bifurcation, *Biorheology* **27**, 163-189.

[82] Witzig S. (1914) *Inaugural dissertation*, Berne.

[83] Womersley J.R. (1957) *The mathematical analysis of the arterial circulation in an oscillatory motion*, Wright Air Development Center, Technical Report WADC-TR56-614.

[84] Zarins C.K., Giddens D.P., Bharadvaj B.K. Sottiurai V.S., Mabon R.F. and Glagov S. (1983) Carotid bifurcation atherosclerosis; Quantitative correlation of plaque localization with flow velocity profiles and wall shear stress, *Circ. Res.* **53**, 502-514.

Samenvatting

Het onderzoek naar de stroming in de halsslagadervertakking is van groot belang voor zo-
wel het inzicht in het ontstaan van atherosclerose (een ziekte, waarbij vernauwingen in de
slagaders optreden) als het vinden van detectie methoden voor deze ziekte. In dit proef-
schrift is de mogelijkheid onderzocht om geringe vernauwingen (25% oppervlakte-reductie)
op te kunnen sporen vanuit informatie over het snelheidsveld in plaats en tijd. Er zijn een
tweetal experimentele technieken gebruikt: waterstof-bellen visualisatie en laser Doppler
anemometrie (LDA). De experimenten zijn verricht onder fysiologische stromingscondities
in starre modellen van een niet-vernauwde en een 25% vernauwde halsslagadervertakking,
waarbij gebruik is gemaakt van Newtonse vloeistoffen. Daarnaast zijn numerieke bereke-
ningen uitgevoerd in 0%, 25% en 50% vernauwde modellen van de halsslagadervertakking
met behulp van een eindige elementen methode.

De waterstof-bellen visualisaties hebben een algemeen en kwalitatief beeld gegeven van
de vloeistofdynamische fenomenen en de interessante plaatsen in de drie-dimensionale (3D)
tijdsafhankelijke stroming in de halsslagadervertakking. Kort na het begin van de diastole
vindt er wervelvorming plaats in een schuiflaag, die de scheiding vormt tussen een gebied
met lage snelheden aan de 'non-divider' wand en een gebied met hoge snelheden aan de
'divider' wand. De invloed van de 25% vernauwing op de stromingsfenomenen is slechts
klein en de belangrijkste invloed wordt gevonden in de stabiliteit van de schuiflaag. Echter,
relatief kleine veranderingen in de stromingscondities blijken de stabiliteit van de schuiflaag
nog sterker te beïnvloeden.

De eindige elementen berekeningen bieden de mogelijkheid om parameter variaties van
de geometrie en de stromingscondities uit te voeren. Bovendien geven ze een goed inzicht
in de complexe 3D axiale en secundaire snelheidsvelden, die optreden in de halsslagader-
vertakking en hier kort worden samengevat. (*i*) Tijdens de vertragingsfase ontstaat een
gebied met negatieve axiale snelheden aan de 'non-divider' kant van de vertakking, dat
zijn maximale grootte bereikt in het begin van de diastole-fase. (*ii*) Tevens ontwikkelt zich
dan een sterk secundair snelheidsveld, dat een schroefvormige beweging van vloeistofdeeltjes
in de vertakking veroorzaakt en het gebied met hoge axiale snelheden in circumferentiële
richting doet uitbreiden. (*iii*) Tijdens de versnellingsfase van de systole verdwijnen alle
negatieve snelheden bij de 'non-divider' wand. De 25% vernauwing beïnvloedt het stro-
mingsveld als volgt: (*i*) het gebied met negatieve snelheden na de vertragingsfase wordt
kleiner, (*ii*) het gebied met negatieve snelheden achter de vernauwing neemt toe, hetgeen
gepaard gaat met een verschuiving van de stroming in de richting van de 'divider' wand en

(*iii*) de secundaire snelheden langs de zijwanden nemen toe.

Met behulp van de LDA techniek zijn nauwkeurige metingen gedaan aan het 3D tijds-afhankelijke snelheidsveld. Dit levert tevens de mogelijkheid om de berekeningen te valideren. Tijdens de vertragingsfase en in de eerste helft van de diastole-fase blijken interessante stromingsfenomenen op te treden. Gedurende de vertragingsfase ontstaat een gebied met negatieve axiale snelheden aan de 'non-divider' kant en in de schuiflaag treden grote radiële gradiënten op in de axiale snelheid. In het begin van de diastole-fase treden oscillaties op in de schuiflaag, zowel in de 0% als 25% vernauwde vertakking. Daarna vindt er een geleidelijke overgang plaats naar de eind-diastolische toestand en er ontstaat een quasi-statische stroming op dat tijdstip. De invloed van de 25% vernauwing kan als volgt worden samengevat: (*i*) in de beginfase van de diastole zijn de axiale snelheden in het lage-snelheden gebied vergroot en (*ii*) de oscillaties in de schuiflaag hebben een iets grotere amplitude en een lagere frequentie.

De vergelijking van de numerieke resultaten en de LDA metingen heeft globaal een redelijke overeenstemming tussen beide methoden opgeleverd. Echter, de tijdschaal van de instationaire fenomenen in de berekeningen blijkt kleiner te zijn dan die in de experimenten. Deze discrepantie wordt toegeschreven aan numerieke onnauwkeurigheden, die veroorzaakt worden door de beperkingen van de gebruikte numerieke methode.

Om wervelvorming in instationaire schuiflagen beter te kunnen begrijpen, is er een studie verricht naar het instationair gedrag van een schuiflaag in een vereenvoudigd 2D rechthoekig kanaal. Ook hier blijkt wervelvorming op te treden gedurende de vertragings-fase en in het begin van de diastole. Hoewel deze studie een bruikbaar inzicht heeft gegeven in het gedrag van instationaire schuiflagen, mag deze stromingssituatie niet zonder meer worden vergeleken met de situatie in de halsslagadervertakking.

De LDA metingen zijn gebruikt om parameters te vinden, die de verschillen tussen stromingen in de 0% en de 25% vernauwde modellen kunnen opsporen. Voor diverse parameters is de toepasbaarheid voor detectie doeleinden geëvalueerd. Voor geen van de parameters is een eenduidige methode gevonden om geringe vernauwingen te kunnen detecteren.

Terugblikkend naar de doelstelling van dit proefschrift, de detectie van geringe vernauwingen, kan de volgende algemene conclusie worden geformuleerd. Hoewel de stromings-fenomenen in de 0% en de 25% vernauwde modellen te kennen geven dat het gedrag van de schuiflaag en de frequenties van de oscillaties worden beïnvloed door de aanwezigheid van een geringe vernauwing, blijkt zelfs voor goed-gecontroleerde condities en nauwkeurige meettechnieken deze invloed niet eenduidig te zijn voor de detectie van *geringe* vernauwingen, omdat het effect op het stromingsveld klein is, lokaal in plaats en tijd en afhankelijk van andere faktoren, zoals de stromingscondities en de geometrie. Voor *middelmatig grote* vernauwingen (50% oppervlakte-reductie) is het eerste moment (een maat voor de scheef-heid van de snelheidsprofielen) op piek-systole, gemeten als funktie van de axiale afstand in de interna, een mogelijk bruikbare detectie parameter. Nader onderzoek is hiervoor nodig. Voor de detectie van geringe vernauwingen (kleiner dan 25% oppervlakte-reductie) is de combinatie van informatie over het snelheidsveld en de lokale veranderingen van de wand-distensibiliteit wellicht meer geschikt.

Nawoord

Het onderzoek, beschreven in dit proefschrift, is verricht in het kader van een projekt van de Stichting Technische Wetenschappen (STW). De praktische uitvoering heeft plaatsgevonden binnen de vakgroep Fundamentele Werktuigkunde (WFW) van de Technische Universiteit Eindhoven. Een groot aantal mensen uit deze vakgroep, maar ook daarbuiten, heeft bijgedragen aan het onderzoek en het tot stand komen van dit proefschrift.

Mijn promotieonderzoek is in 1989 gestart binnen het reeds lopende 'Atherosclerose-projekt', dat toen onder leiding stond van Anton van Steenhoven. Na zijn vertrek bij WFW bleef hij betrokken bij het projekt via de STW-vergaderingen. Bij het schrijven van dit proefschrift is hij als tweede promotor heel direkt betrokken geweest. Zijn kritische en ook positieve houding zijn voor mij zeer waardevol en stimulerend geweest.

De begeleiding is reeds in een vroeg stadium overgenomen door Frans van de Vosse, die met veel enthousiasme en volle energie het Atherosclerose-projekt voortzette. Frans was altijd belangstellend, stond altijd klaar en de vele discussies, die we gehad hebben, waren zeer vruchtbaar. Zijn kennis en ervaring op het gebied van de numerieke stromingsleer waren een belangrijke steun bij de stromingsberekeningen.

Het experimentele werk heb ik verricht in het 'Laboratorium voor Biomechanika' (beter bekend als 'Bio-lab'). Behalve dat ik daar in een hele prettige sfeer heb kunnen werken, stonden daar Theo van Duppen, Leo Wouters en Roel van de Brink altijd klaar voor de technische ondersteuning. Theo van Duppen heeft de experimentele opstellingen gemaakt en vele tussentijdse klussen geklaard. Samen met Hans Hijink, Sjaak Couwenberg en Sjors van de Molengraft maakte hij de experimentele modellen van de geometrisch complexe halsslagadervertakking. Zonder de bijdrage van al deze mensen was het experimentele werk ondenkbaar geweest. Ron Snijders heeft gezorgd voor de ondersteuning bij het schrijven van software voor diverse doeleinden. Met name bij de verwerking van de laser Doppler metingen heeft hij samen met Frank Gijsen een belangrijke bijdrage geleverd aan dit onderzoek.

Tijdens de promotie heb ik diverse stagiaires en afstudeerders begeleid, hetgeen altijd een stimulerend effekt op mij en het onderzoek had. Ik ben daarom de stagiaires Jos Westenberg, Jacco Steenhuijsen, Mark Sabel, Patrick Kleuskens en Maurice van der Beek en de afstudeerder Robert Kuypers erg dankbaar. In het bijzonder wil ik de afstudeerders Frank Gijsen en Carla Reijnierse noemen, vanwege hun grote bijdrage aan respectievelijk de laser Doppler experimenten in de halsslagadervertakking en de modelstudie aan 2D schuiflagen.

133

Bij de figuren van de stromingsberekeningen uit de hoofdstukken 3 en 8 heb ik veel hulp gehad van Ion Barosan, die zich op het Rekencentrum van de TUE bezighoudt met numerieke visualisatie methoden. Met veel inzet en geduld heeft hij de vele plaatjes geproduceerd, waarvoor ik hem veel dank verschuldigd ben. De visualisatie beelden van de 2D schuiflaag uit hoofdstuk 6 zijn bijgewerkt door Gert van der Plas.

Tenslotte wil ik mijn eerste promotor Jan Janssen bedanken voor het in goede banen leiden van het onderzoek en het bewaken van de grote lijn, met name ook bij het schrijven van dit proefschrift. Tevens ben ik de overige leden van mijn promotiecommissie Anton van Steenhoven, Frans van de Vosse, Rini van Dongen en Rob Reneman erkentelijk voor hun suggesties ter verbetering van dit proefschrift. De belangstelling en goede suggesties, die ik gedurende mijn promotieperiode kreeg van Rini van Dongen en Gerrit Vossers heb ik zeer gewaardeerd.

Er zijn vele mensen, die niet genoemd zijn in dit nawoord, die op hun eigen manier een steentje hebben bijgedragen aan het bereiken van dit punt. Mijn ouders wil ik bedanken voor hun aanmoediging en steun. In het bijzonder wil ik mijn -aanvankelijke collega en kamergenoot, maar inmiddels- vriend Hans bedanken voor alle geduld, begrip en de zo waardevolle steun achter de schermen.

Daniëlle Palmen, 8 April 1994

Curriculum Vitae

13-11-1965	geboren te Susteren
1978 - 1984	Atheneum β opleiding,
	Bisschoppelijk College te Echt
1984 - 1989	Technische Natuurkunde studie,
	Technische Universiteit Eindhoven (TUE)
1989 - 1994	promotie-onderzoek,
	vakgroep Fundamentele Werktuigkunde (WFW),
	Technische Universiteit Eindhoven,
	in dienst van STW en de TUE

Stellingen

behorende bij het proefschrift

The influence of minor stenoses
on carotid artery flow

1. Het stromingsonderzoek aan verstoringen in vernauwende buizen is niet relevant voor de studie van de stroming in een halsslagadervertakking met een geringe vernauwing.

   - Hoofdstuk 2 van dit proefschift

2. De snelheids-oscillaties in de interna zijn in tegenstelling tot de bevindingen van Ku *et al.* (1987) niet het gevolg van oscillaties in de fysiologische flowpuls, maar van schuiflaaginstabiliteiten, die ontstaan aan het begin van de diastolische fase.

   - Ku D.N. and Giddens D.P. (1987), 'Laser Doppler anemometer measurements of pulsatile flow in a model carotid bifurcation', *J. Biomech.* **20**, 407-421.
   - Hoofdstuk 4 van dit proefschrift

3. De eindige elementen methode, zoals die gebruikt is in dit proefschrift, is niet in staat het instabiele gedrag van de schuiflaag nauwkeurig te beschrijven.

   - Hoofdstuk 5 van dit proefschrift

4. De detectie van geringe vernauwingen (25% oppervlakte reduktie) uit informatie van alleen het snelheidsveld is klinisch niet haalbaar.

   - Hoofdstukken 7 en 8 van dit proefschrift

5. Numerieke visualisatiepakketten zijn onmisbaar om de onderzoeker een goed inzicht te geven in de grote hoeveelheden data van bijvoorbeeld complexe stromingsproblemen, die berekend zijn met behulp van supercomputers.

   - Belie R.G. (1985), 'Flow visualization in the Space Shuttle Main Engine', *J. Mech. Eng.* **107**, 27-33.

6. De tijd, besteed aan de vorm en het uiterlijk van een wetenschappelijk verslag, is vaak te groot ten opzichte van de tijd, besteed aan het inhoudelijke.

7. Het samenplaatsen op een kamer van meerdere AIO's, die ongeveer in een gelijke fase van de promotie verkeren, heeft behalve een belangrijke sociale funktie ook een aanzienlijke stimulerende werking op de promotie-werkzaamheden.

8. Het feit dat er door de Technische Universiteiten aparte aktiviteiten voor meisjes worden georganiseerd (bijvoorbeeld de pré-intro en Thea-dagen) is in strijd met het streven dat meisjes zoveel mogelijk moeten integreren in de door mannen gedomineerde technische wereld.

9. Het gebrek aan part-time banen voor hoger-opgeleiden in het bedrijfsleven ontneemt paren van twee hoger-opgeleiden de mogelijkheid om het ouderschap te combineren met een loopbaan.

10. De invloed van psychische en sociale factoren op het herstel en fysieke welzijn van patiënten wordt in de Westerse techniek-georiënteerde gezondheidszorg onderschat.

11. Musiceren is een perfecte tegenhanger van het bedrijven van wetenschap: beiden vereisen weliswaar techniek, vaardigheden en gevoel, maar het uiteindelijke resultaat wordt bij musiceren vooral bepaald door het *(subjectieve) gevoel* dat de musicus erin legt, terwijl wetenschappelijke resultaten worden gedomineerd door *(objectieve) rationele* argumenten.

12. Mensen raken verder van elkaar door zwijgen dan door afstanden.

    • Coco Chanel

13. Wie het hardst schreeuwt, krijgt het woord.

14. Als het niet kan zoals het moet, moet het zoals het kan.

Eindhoven, april 1994   Daniëlle Palmen